

**IRON OXIDATION STATE IN (Mg,Fe)O: CALIBRATION OF THE FLANK  
METHOD ON SYNTHETIC SAMPLES AND APPLICATIONS ON NATURAL  
INCLUSIONS FROM LOWER MANTLE DIAMONDS**

Von der Fakultät für Chemie und Geowissenschaften  
der Universität Bayreuth

zur Erlangung der Würde eines Doktors der Naturwissenschaften

- Dr. rer. nat. -

Dissertation

vorgelegt von

Micaela Longo

aus Rom (Italien)

Bayreuth, July 2009

This doctoral thesis was prepared at the Bayerisches Geoinstitut, University of Bayreuth between April 2006 and July 2009. It was supervised by Dr. Catherine McCammon.

This is a full reprint of the dissertation submitted to attain the academic degree of Doctor of Natural Sciences (Dr. rer. nat.) and approved by the Faculty of Biology, Chemistry and Geosciences of the University of Bayreuth.

Date of submission: July 29, 2009

Date of defence (disputation): December 4, 2009

Doctoral Committee:

Prof. Falko Langerhornst

Chairman

Prof. Leonid Dubrovinsky

1<sup>st</sup> reviewer

Prof. Gerhard Brey

2<sup>nd</sup> reviewer

Prof. Hans Keppler

Prof. Friederich Seifert

Prof. Jürgen Senker

## Acknowledgments

I would like to thank the European Commission to provide the funding for the present Ph.D project under the Marie Curie Action Stage Training of Researchers (6<sup>th</sup> Framework Programme, contract number MEST-CT-2005-019700).

I would like to thank my dissertation supervisor Dr. Catherine McCammon for her assistance during my Ph.D work, with her patience in teaching me and a huge number of stimulating discussions and feedbacks.

My two advisors, Tiziana Boffa Ballaran and Dan Frost, for providing stimulating discussions, exchange of ideas and support in the labs.

Detlef Krauß, for his help during the long time spent at the electron microprobe. I would like to thank him for his patience teaching me how to use the instrument and for his constant constructive help during the calibration developments.

Steven Jacobsen for showing interest in the project and providing samples; Galina Bulanova, Felix Kaminsky and Ralf Tappert for providing precious natural inclusions from lower mantle diamonds. Kazuhiko Otsuka and Vincenzo Stagno for providing synthetic samples from their Ph.D work.

Thanks to Niko Walte for his help in the laboratory and his help with translating documents in German for me. Thanks to Gudmundur Gudfinnsson for his precious assistance in the multi anvil laboratory.

Thanks to Hubert Schultze, Uwe Dittman, Heinz Fisher and Stefan Übelhack for sharing their skills in technology and in the sample preparation. Gerti Gollner, Anke Potzel, Sven Linhardt, Kurt Klasinsky are also warmly thanked for their assistance and support in the labs and help for technical problems.

Thanks to Lydia Kison-Herzing, Petra Buchert and Stefan Keyssner to make Bayerisches Geoinstitut different from every other place in the world! Thanks for making our life easier many many times. Special thanks to all my colleagues for stimulating discussions at any time, and for their support, at any time. Special thanks to all my friends - almost a family - Olga Narygina, Coralie Weigel, Polina Gavrilenko, Shantanu Keshav, Martha Pamato and Davide Novella for their friendship and support. Thanks to Fabrizio Nestola for his patience in answering to all my numerous questions, to always share with me his own experience and enthusiasm for science.

And finally I would like to thank my family in Rome for their comprehension and support even from far: Francesca, Fiorentino, Eleonora and Dario, always in my thoughts.

# Table of Contents

<b>Summary</b>	<b>I</b>
<b>Zusammenfassung</b>	<b>i</b>
<b>1. Introduction</b>	<b>1</b>
1.1 MgO-FeO solid solution	1
- <i>MgO Periclase</i>	2
- <i>FeO Wüstite</i>	3
- <i>(Mg,Fe)O Ferropericlase</i>	4
- <i>Fe<sup>3+</sup> incorporation and point defects in (Mg<sub>x</sub>Fe<sub>1-x</sub>)O</i>	7
1.2 Earth's interior structure and mineral composition	8
1.3 Diamonds from the lower mantle	14
1.4 Ferropericlase as a diamond inclusion	18
1.5 Oxygen fugacity in lower mantle diamonds and the determination of the Fe <sup>3+</sup> /ΣFe ratio	19
1.6 The "flank method": state of the art	22
1.7 Aim of the project	25
<b>2. Experimental Methods</b>	<b>26</b>
2.1 Synthesis of (Mg,Fe)O crystals	26
2.2 Gas-Mixing furnace	26
2.3 Multi Anvil Apparatus	28
2.4 Mössbauer Spectroscopy	29
2.4.1 The basic principles	30
2.4.2 Conventional source and point source	33
2.5 Powder X-Ray Diffraction	35
2.6 Electron MicroProbe Analysis (EMPA)	36
- <i>Basic principle</i>	36
- <i>X-ray emission spectra and electronic transitions</i>	37
- <i>X-rays: intensity and absorption effects</i>	39
- <i>Heat production</i>	40
- <i>Wave Length Dispersive Spectrometers</i>	40

2.6.1 Major elements analysis plus qualitative analysis	42
- Flank Method procedure: spectrometer calibration	42
- Flank Method measurements	44
- Major element analysis combined with flank method measurements	44
<b>3. Results (1): Flank Method Calibration</b>	<b>46</b>
3.1 Flank Method Results: Determination of the $L\alpha$ and $L\beta$ flank method measuring positions	46
3.2 Flank Method calibration for natural garnets on the Jeol JXA-8200 @ BGI	49
3.3 Flank Method calibration for synthetic (Mg,Fe)O ferropericlae: present study	56
- Attempt no 1	61
- Attempt no 2	62
- Attempt no 3	62
3.3.1 A new calibration for (Mg,Fe)O after spectrometer adjustments	69
<b>4. Results (2): Flank Method Applications</b>	<b>72</b>
4.1 Synthetic (Mg,Fe)O from a different study	72
4.1.1 (Mg,Fe)O containing secondary mineral phase	72
4.1.2 (Mg,Fe)O from High Pressure High Temperature diffusion experiments	77
4.1.3 Flank Method applied to synthetic (Mg,Fe)O at 24 GPa	90
4.2 Natural (Mg,Fe)O diamond inclusions	89
- Juina Area, Mato Grosso (Brazil)	90
- Machado River (Brazil)	91
- Eurelia and Springfield Basin, Orooro (Australia)	93
4.2.1 Sample preparation	93
4.2.2 Flank Method and Major element analysis results for natural (Mg,Fe)O	94
<b>5. Discussion and Future Perspectives</b>	<b>100</b>
5.1 Overview of the present study and research goals achieved	100
5.2 Compositional variation determined by flank method	102
5.2.1 Detection of extra phase(s) other than primary (Mg,Fe)O	102

5.2.2 Fe <sup>3+</sup> variation along diffusion profiles	103
5.3 Oxygen fugacity in lower mantle (Mg,Fe)O ferropericlas	105
5.3.1 Implication for diamond formation	107
5.4 Future perspectives for flank method applications and lower mantle studies	112
<b>6. Concluding statements and further work</b>	<b>113</b>
<b>7. References</b>	<b>116</b>

## Summary

(Mg,Fe)O ferropericlasite is the most common mineral found in diamonds originating in the lower mantle (more than 50% of occurrences). It is well known that the  $\text{Fe}^{3+}$  concentration in (Mg,Fe)O is sensitive to oxygen fugacity, even at high pressures. Therefore, the determination of  $\text{Fe}^{3+}/\Sigma\text{Fe}$  in such inclusions provides a direct method for investigating lower mantle redox conditions during diamond formation. The goal of the present research is to calibrate the “flank method” by electron microprobe using synthetic (Mg,Fe)O, and then apply the method to determine *in situ*  $\text{Fe}^{3+}/\Sigma\text{Fe}$  in ferropericlasite inclusions from lower mantle diamonds. Up to now a calibration of the flank method is available only for garnets.

Initially, the flank method was calibrated for garnets to test the reproducibility of the method on the Jeol XA-8200 electron microprobe in use at Bayerisches Geoinstitut. Results showed that for garnets a new calibration curve needs to be established at each working session.

Then the flank method was calibrated for the Jeol XA-8200 electron microprobe in use at Bayerisches Geoinstitut for a homogeneous set of (Mg,Fe)O ferropericlasite crystals over a wide range of composition ( $x_{\text{Fe}} = 2$  to 60 at.%) and  $\text{Fe}^{3+}/\Sigma\text{Fe}$  (1 to 15%). Samples were obtained by performing high pressure high temperature experiments in a multi anvil apparatus. In order to avoid compositional effects on flank method measurements, the high sample homogeneity was essential. Moreover, the determination of the  $\text{Fe}^{3+}/\Sigma\text{Fe}$  ratio needed to be extremely accurate. For this purpose, a more accurate procedure for fitting the Mössbauer spectra of the final set of synthetic (Mg,Fe)O was adopted.

The calibration curve determined is  $\text{Fe}^{2+} = 46.238 + 8.161 * \ln(\Sigma\text{Fe}) - 137.01 * (\text{L}\beta/\text{L}\alpha) + 85.57 * (\text{L}\beta/\text{L}\alpha)^2$ , for a Fe compositional range between 3 and 47 wt. %. A comparison of  $\text{Fe}^{3+}/\Sigma\text{Fe}$  determined by flank method and values determined earlier by Mössbauer spectroscopy shows that results are generally consistent between the two different methods within the experimental errors. In contrast with garnet, the calibration curve established for ferropericlasite does not need to be recalibrated at each microprobe session. Therefore, the calibration curve can be considered universal for the electron microprobe in use if the spectrometer adjustments remain identical with time.

To explore applications of the flank method, a set of (Mg,Fe)O samples from diffusion studies was also investigated. Three (Mg,Fe)O crystals were measured by electron microprobe in

order to test the sensitivity and accuracy of the flank method for small variations of bulk  $\Sigma\text{Fe}$  (wt%) as well as to measure  $\text{Fe}^{3+}/\Sigma\text{Fe}$  along diffusion profiles. In the present work it is demonstrated how the flank method can be a powerful tool to measure small variations in  $\text{Fe}^{3+}$  content, with a spatial resolution of only few microns (2-3  $\mu\text{m}$ ) and a lower detection limit of  $\Sigma\text{Fe}$  of 3 wt%. Moreover, the measurement of  $\text{Fe}^{3+}$  content on the micron scale enables the study of the variation of oxygen fugacity conditions along diffusion gradients.

A set of (Mg,Fe)O ferropericlasite inclusions from ultra deep diamonds selected worldwide were analyzed by the flank method. The data set consists of eighteen (Mg,Fe)O ferropericlasite samples from Juina, Brazil, Machado River, Brazil, and Ororoo, Australia. Inclusions are between 10 and 50  $\mu\text{m}$  in size, therefore they are suitable to perform flank method measurements to determine  $\text{Fe}^{3+}/\Sigma\text{Fe}$ .

For the first time  $\text{Fe}^{3+}/\Sigma\text{Fe}$  ratios were measured directly at the electron microprobe on inclusions of less than 50  $\mu\text{m}$  in size. Results for the (Mg,Fe)O inclusions show good agreement with the theoretical trend described by the synthetic samples, which confirms high phase homogeneity for most of the samples. Flank method measurements show a large range of  $\text{Fe}^{3+}/\Sigma\text{Fe}$  values for (Mg,Fe)O inclusions, which implies a large range of oxygen fugacities based on charge balance calculations. This large range of oxygen fugacities is similar to results for a suite of much larger inclusions from Kankan, Guinea, and São Luiz, Brazil, that were studied using Mössbauer spectroscopy. The variation of oxygen fugacity seems to be correlated to the geographical distribution of the inclusions studied, showing a redox gradient with more reducing conditions at Kankan, Guinea, and São Luiz, Brazil, and more oxidized in the case of Juina and Machado River, Brazil, and Eurelia, Australia. Such a correlation may be linked to the proto-pacific subduction mechanism, and the different ages combined with the geographic variation may indicate a difference in depth correlating with the large redox variation. Inclusions recovered from the same host diamond from Eurelia shows a strong redox gradient, which suggests a drastic change in the oxygen fugacity conditions during diamond growth. In order to provide information on the mechanisms able to control the redox conditions at lower mantle depths, a multi disciplinary study is suggested for further work.

## Zusammenfassung

(Mg,Fe)O Ferroperiklas ist das häufigste Mineral aus dem unteren Mantel, welches in Form von Diamanteinschlüssen gefunden wird (über 50% der Vorkommen). Es ist bekannt, dass die Fe Konzentration in (Mg,Fe)O sogar bei hohem Druck abhängig von der Sauerstoff fugazität ist. Somit stellt die Analyse des  $Fe^{3+}/\Sigma Fe$  in diesen Einschlüssen eine direkte Methode dar, um den Redoxzustand des unteren Mantels während der Diamantbildung zu untersuchen. Das Ziel dieser Untersuchung ist die Kalibrierung der „Flankierungsmethode“ mit Hilfe der Elektronenmikrosonde an synthetischem (Mg,Fe)O und die Benutzung der Methode, um eine *in situ*  $Fe^{3+}/\Sigma Fe$  Bestimmung in Ferroperiklaseinschlüssen aus dem unteren Mantel vorzunehmen. Bisher ist eine solche Kalibrierung nur für Granat verfügbar.

Zunächst wurde die Flankierungsmethode an Granat kalibriert, um die Reproduzierbarkeit der Methode an der Jeol XA-8200 Elektronenmikrosonde des Bayerischen Geoinstituts zu testen. Die Resultate ergaben, dass für den Granat für jede Messeinheit eine neue Kalibrierung notwendig ist.

Danach wurde die Flankierungsmethode für die Jeol XA-8200 Mikrosonde vom BGI für eine homogene Gruppe von (Mg,Fe)O Ferroperiklaskristallen über eine weite Variation von Zusammensetzungen kalibriert. Die Proben wurden mit Hilfe von Hochdruckexperimenten in der Vielstempelzelle hergestellt. Die gute Probenhomogenität war notwendig, um Zusammensetzungseffekte auszuschließen. Außerdem musste die Messung des  $Fe^{3+}/\Sigma Fe$  Verhältnisses extrem präzise sein. Um das zu erreichen wurde eine genauere Methode zur Anpassung der Mößbauer Spektren der letzten Gruppe synthetischer (Mg,Fe)O Proben gewählt.

Die gefundene Kalibrierungskurve lautet  $Fe^{2+} = 46.238 + 8.161 * \ln(\Sigma Fe) - 137.01 * (L\beta/L\alpha) + 85.57 * (L\beta/L\alpha)^2$  für ein Fe Anteil von 3 bis 47 Gew.%. Ein Vergleich zwischen der  $Fe^{3+}/\Sigma Fe$  Analyse mit der Flankierungsmethode und mit Mößbauerspektroskopie zeigt eine generelle Konsistenz im Rahmen des experimentellen Fehlers. Im Gegensatz zum Granat muss die Kalibrierungskurve für Ferroperiklas nicht vor jeder Mikrosondensitzung neu kalibriert werden. Somit kann die Kalibrierungskurve als universal gesehen werden, sofern die Spektrometereinstellungen gleichbleiben.

Um die Anwendungen der Flankenmethode zu untersuchen, wurde eine Gruppe von (Mg,Fe)O Proben aus anderen Diffusionsstudien ebenfalls untersucht. Drei (Mg,Fe)O

Kristalle wurden mit der Mikrosonde gemessen, um die Empfindlichkeit und Genauigkeit der Flankenmethode für geringe Variationen des gesamten  $\Sigma\text{Fe}$  (Gew.%) zu testen und um  $\text{Fe}^{3+}/\Sigma\text{Fe}$  entlang von Diffusionsprofilen zu messen. In der vorliegenden Arbeit wird demonstriert, dass die Flankenmethode ein leistungsfähiges Werkzeug zum Messen von kleinen Variationen im  $\text{Fe}^{3+}$  Gehalt ist, mit einer räumlichen Auflösung von wenigen  $\mu\text{m}$  (2-3  $\mu\text{m}$ ) und einer unteren  $\Sigma\text{Fe}$  Nachweisgrenze von 3 Gew.%. Darüber hinaus ermöglicht die  $\text{Fe}^{3+}$  Messung im Mikromaßstab die Untersuchung von Änderungen der Sauerstoff fugazität entlang von Diffusionsprofilen.

Eine Gruppe von (Mg,Fe)O Ferroperiklaseeinschlüssen aus ultratiefen Diamanten aus der ganzen Welt wurde mit der Flankenmethode analysiert. Der Datensatz besteht aus 18 (Mg,Fe)O Ferroperiklasproben aus Juina, Brasilien, Machado Fluss, Brasilien, und Ororoo, Australien. Die Einschlüsse sind 10-50  $\mu\text{m}$  groß, somit sind sie geeignet für Flankiermethodenmessungen zur Bestimmung von  $\text{Fe}^{3+}/\Sigma\text{Fe}$ .

Zum ersten Mal wurden  $\text{Fe}^{3+}/\Sigma\text{Fe}$  Verhältnisse direkt mit der Mikrosonde an Einschlüssen vorgenommen, die kleiner als 50  $\mu\text{m}$  waren. Die Ergebnisse für die (Mg,Fe)O Einschlüsse zeigen eine gute Übereinstimmung mit der theoretischen Trendlinie der synthetischen Probe, was eine große Phasenhomogenität für die meisten Proben bestätigt. Messungen mit der Flankenmethode zeigen eine große Variation der  $\text{Fe}^{3+}/\Sigma\text{Fe}$  Werte für die (Mg,Fe)O Einschlüsse aus Kankan, Guinea und São Luiz, Brasilien, die mit Hilfe der Mößbauerspektroskopie untersucht wurden. Die Variation der Sauerstoff fugazität scheint mit der geographischen Herkunft der Einschlüsse korreliert zu sein. Sie zeigen einen Redoxgradienten mit reduzierenderen Bedingungen in Kankan, Guinea und São Luiz, Brasilien und oxidierenderen Bedingungen für die Proben aus Juina und Machado River, Brasilien und Eurelia, Australien. Eine solche Korrelation könnte mit dem protopazifischen Subduktionsmechanismus zusammenhängen, und die unterschiedlichen Alter kombiniert mit den geographischen Variationen könnte einen Tiefeunterschied korreliert mit großen Redoxvariationen anzeigen. Einschlüsse aus einem einzelnen Diamanten aus Eurelia zeigen einen großen Redoxgradienten, was eine drastische Veränderung der Sauerstoff fugazität während des Diamantwachstums bedeuten könnte. Um weitere Informationen über den Mechanismus zu gewinnen, der die Redoxbedingungen in Tiefen des unteren Mantels kontrolliert, wird eine multidisziplinäre Studie für weitergehende Untersuchungen vorgeschlagen.

## 1. Introduction

### 1.1 The MgO-FeO solid solution

Minerals of the MgO-FeO solid solution belong to the simplest binary compounds known. At ambient pressure and temperature conditions, both MgO (periclase) and FeO (wüstite) adopt the closest packed structure of rock-salt (halite structure, space group  $Fm3m$ , Fig. 1.1), have similar crystal structures, formal valence states and very close lattice parameters (about 4.212 Å for MgO and about 4.25 Å for FeO, depending on its stoichiometry). Therefore, due to their similar crystallographic configuration a complete (Mg,Fe)O solid solution can be formed. According to the nomenclature for the solid solution  $(Mg_x,Fe_{1-x})O$ , the term ferropericlase indicates a compositional range with <50 mol% FeO and magnesiowüstite a compositional range with >50 mol% FeO (Prewitt and Downs, 1998). The phase equilibria for the system MgO-FeO-Fe<sub>2</sub>O<sub>3</sub> at 1300°C is shown in Fig. 1.2. So far, many studies at high pressure and high temperature have been conducted on MgO-FeO solid solution and they will be discussed in the following sections of this chapter.

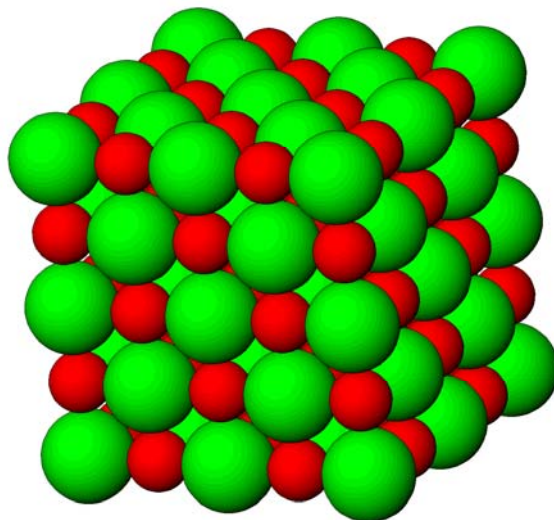


**Fig. 1.1** –Halite structure model for (Mg,Fe)O ferropericlase: Mg and Fe are represented by the red spheres, whereas the green spheres are the oxygen atoms.

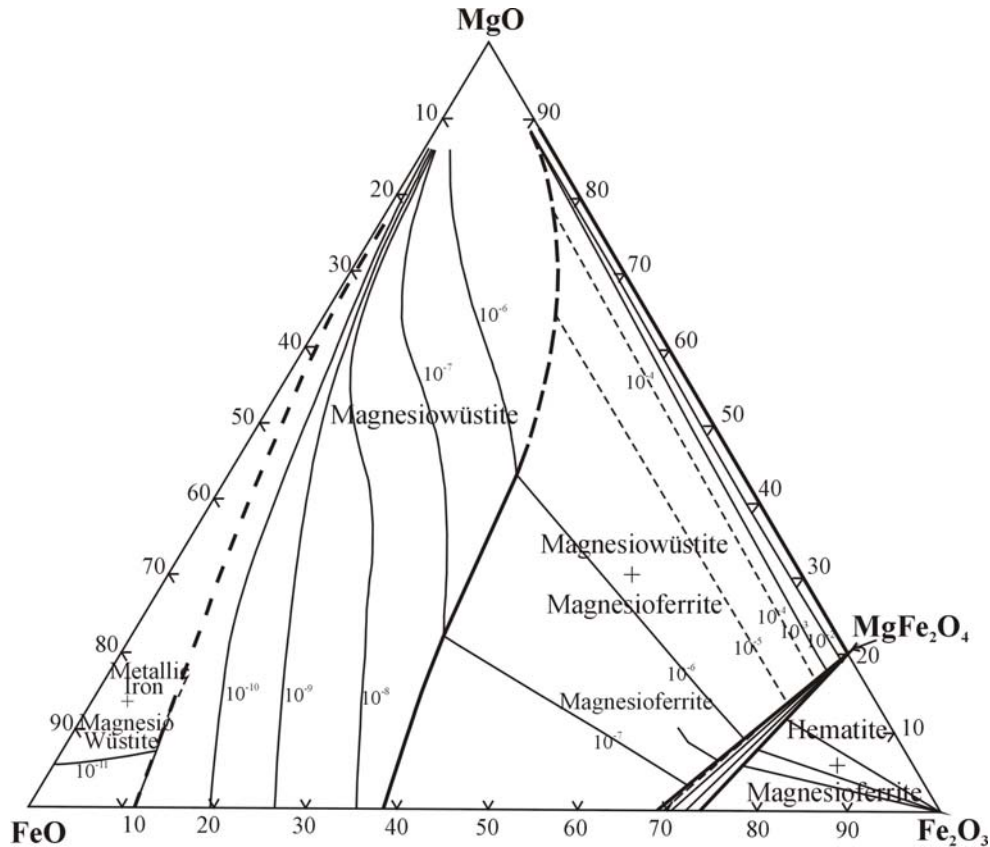


**Fig. 1.2** –MgO-FeO-Fe<sub>2</sub>O<sub>3</sub> system at 1300°C. Heavy solid lines mark the phase boundaries, light solid lines represent the oxygen isobars, both dashed when approximated. (Mg,Fe)O compositions in equilibrium with metallic iron refer to Hahn and Muan (1962) (*Modified after Spiedel 1967*).

### *MgO Periclase*

MgO periclase is one of the most widely studied phases in mineral physics and one of the few phases to maintain the B1 structure up to very high pressures. In fact, MgO does not undergo any phase transitions at least before 227 GPa (Duffy et al., 1995), and most likely to pressures > 400 GPa at ambient temperature based on lattice dynamical considerations (Karki et al., 1997). The bulk properties and elastic properties have been intensively investigated during the past decades (Spetzler, 1970; Jackson and Niesler, 1982; Chen et al., 1998; Reichmann et al., 1998, Fei, 1999; Sinogeikin and Bass, 2000; Zha et al., 2000) and are well known at high pressures (Zha et al., 2000). Therefore, periclase is a perfect candidate to be used as an internal standard material in high pressure and high temperature studies. A comparison between MgO, FeO and (Mg<sub>x</sub>,Fe<sub>1-x</sub>)O is reported in Table 1.1.

### *FeO Wüstite*

The iron monoxide FeO presents a more complex behavior than MgO at high pressure and high temperature and is an important member of the highly correlated transition metal oxide group including NiO, CoO, and MnO.  $\text{Fe}_{1-x}\text{O}$  is the classic non-stoichiometric oxide, where  $x$  typically ranges from 0.90 to 0.95 at room pressure. Stoichiometries as high as 0.98 or 0.99 have been achieved at pressures above 10 GPa (Zhang, 2000). The elastic properties for  $\text{Fe}_{1-x}\text{O}$  have been investigated as a function of pressure and temperature for different  $(1-x)$  values (Hazen, 1981) (Table 1.1).

Shock waves and diamond anvil cell experiments were performed in order to investigate FeO phase transitions. Jeanloz and Ahrens (1980) and Knittle and Jeanloz (1986) reported a phase transition occurring at about 70 GPa and temperatures over 1000 K, which would be due to a change in ferrous iron character at high pressures, resulting in a metallic phase, but no evidence supporting this theory were found in resistivity measurements in the diamond cell. Wüstite undergoes a phase transition to the distorted rhombohedral face-centered lattice at conditions around 17 GPa and 300 K (Zou et al. 1980, Yagi et al., 1985). The rhombohedral distortion (rhombohedral angle  $<60^\circ$ ) would subsequently increase with pressure and might be due to shortened Fe-Fe distance.

At high pressures and temperatures (above 90 GPa and 600 K) a phase transition into a hexagonal structure was observed (Fei and Mao, 1994) which was interpreted to be a NiAs-type (B8) structure. This transition consists of a change in symmetry due to a different stacking sequence of the close-packed planes, with the nearest-neighbor Fe-O bond distances being essentially the same in both structures.

*(Mg,Fe)O Ferropericlase*

(Mg,Fe)O is the dense magnesium–iron monoxide coexisting with (Mg,Fe,Al)SiO<sub>3</sub> at the P–T conditions of Earth’s lower mantle (e.g. Shim et al., 2001). (Mg,Fe)O is therefore believed to be the most abundant non-silicate oxide in the Earth. However, (Mg,Fe)O is rarely found in nature, but is the most abundant inclusion in diamonds from the deep Earth (Harte and Harris, 1994). Despite its cubic structure, (Mg,Fe)O ferropericlase exhibits a strong elastic anisotropy at ambient conditions (Reichmann et al., 2000; Jacobsen et al., 2002). The effect of pressure and temperature on the elastic anisotropy of the end member MgO has been studied both theoretically (e.g. Karki et al., 1999) and experimentally (e.g. Chen et al., 1998). A first-principles calculation (Chen et al., 1998) indicates that temperature effects counteract those of pressure; however, temperature effects decrease monotonically as pressure increases. The elastic anisotropy of MgO first decreases with pressure (and depth), vanishing at about 20 GPa (~ 600 km depth), and then increases throughout the pressure range of the lower mantle (24–130 GPa, representing 660–2900 km depth). At pressures corresponding to the bottom of the lower mantle, MgO is strongly anisotropic, suggesting that Mg-rich ferropericlase could be responsible for the seismic anisotropy of the D’’ layer (e.g. Mainprice, 2007). Moreover, the discovery of a pressure-induced electronic spin-pairing transition in (Mg,Fe)O occurring around 50 GPa may additionally contribute to affect the anisotropy of the D’’ layer (e.g. Badro et al., 2003; Speziale et al., 2005; Lin et al., 2005; Kantor et al., 2006, 2007; Speziale et al., 2007).

Experimental studies (Lin et al., 2003) have also shown that the addition of a certain amount of MgO in FeO should further depress the stability field of wüstite in the rhombohedral phase (Fig. 1.3), and that the B1–rhombohedral phase transformation in ferropericlase is unlikely to occur under lower mantle conditions.

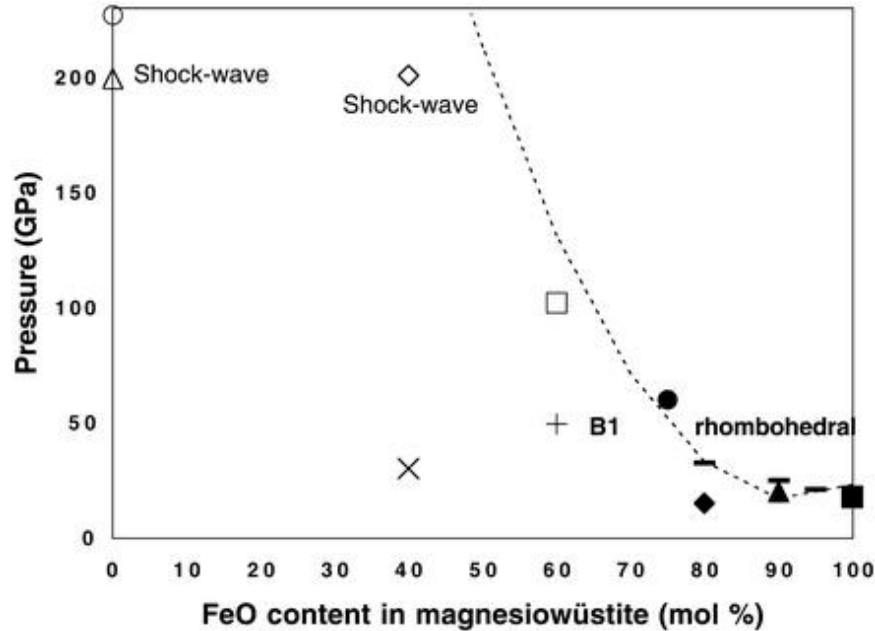


**Fig. 1.3** – Pressure–composition phase diagram of magnesiowüstite. Open symbols, +, and × represent magnesiowüstite in the B1 structure; solid symbols and ticks indicate the phase-transition pressure from B1 to the rhombohedral structure. The dashed curve represents a simple polynomial fit to all of the phase-transition pressures observed in magnesiowüstite. Two shock-wave studies on MgO and  $(\text{Mg}_{0.6}\text{Fe}_{0.4})\text{O}$  are at high P–T conditions (Vissiliou and Ahrens, 1981, 1982), and other studies are at high pressure and 300 K. ■, Shu et al. (1998a); solid lines, Shu et al. (1998b); ▲, Mao et al. (2002); ♦, Richet et al. (1989); ● and □, Lin et al. (2003); +, Richet et al. (1989); ◊, Vissiliou and Ahrens (1982); ×, Fei et al. (1992); ○, Duffy et al. (1995); and △, Vissiliou and Ahrens (1981) (*Diagram modified from Lin et al. 2003*).

The addition of MgO to FeO also decreases the stability of the NiAs structure, and therefore the B1–NiAs phase transformation in  $(\text{Mg,Fe})\text{O}$  suggested by Fei and Mao (1994) would also not be expected to occur in the lower mantle. High pressure high temperature experiments on Mg-Fe partitioning between magnesiowüstite and Si-perovskite indicate that the FeO content in magnesiowüstite decreases with increasing P–T and with the addition of  $\text{Al}_2\text{O}_3$  to the system (Mao et al. 1997, Kesson et al., 2002). This behavior therefore suggests that ferropericlase (Mg content > 50%) is favored in the deep lower mantle. No phase transformation was observed in  $(\text{Mg,Fe})\text{O}$  ferropericlase up to 120 GPa and 2300 K (Andrault, 2001; Kesson et al., 2002).

Elastic properties for  $(\text{Mg}_x\text{Fe}_{1-x})\text{O}$  with different  $x$  values have been investigated by Jacobsen et al. (1999) (Table 1.1). Experimental studies have shown that the addition of iron into MgO has a strong influence on the elastic constants at ambient conditions, and that the effect of

iron on the elasticity of (Mg,Fe)O is most pronounced up to about the composition 30 mol% FeO (Jacobsen et al., 2002).

**Tab.1.1** – Elastic properties for the MgO-FeO solid solution

Composition	$K_T$	$K'$	$\alpha$ to 1000°C
<b>MgO</b> <sup>1</sup>	160(2) GPa <sup>1</sup>	4.15 <sup>1</sup>	32 x 10 <sup>-6</sup> K <sup>-1</sup> <sup>2</sup>
<b>Fe<sub>0.91</sub>O</b> <sup>3</sup>	152(2) GPa <sup>3</sup>	2.1(4) <sup>3</sup>	34 x 10 <sup>-6</sup> K <sup>-1</sup> <sup>5</sup>
<b>Fe<sub>0.94</sub>O</b> <sup>3</sup>	153(2) GPa <sup>3</sup>	2.1(4) <sup>3</sup>	34 x 10 <sup>-6</sup> K <sup>-1</sup> <sup>5</sup>
<b>Fe<sub>0.96</sub>O</b> <sup>3</sup>	154(2) GPa <sup>3</sup>	2.1(4) <sup>3</sup>	34 x 10 <sup>-6</sup> K <sup>-1</sup> <sup>5</sup>
<b>(Mg<sub>0.73</sub>Fe<sub>0.26</sub>□<sub>0.01</sub>)O</b> <sup>4</sup>	158(1) GPa <sup>4</sup>	5.5(2) <sup>4</sup>	-
<b>(Mg<sub>0.42</sub>Fe<sub>0.54</sub>□<sub>0.04</sub>)O</b> <sup>4</sup>	156(2) GPa <sup>4</sup>	5.5(2) <sup>4</sup>	-
<b>(Mg<sub>0.24</sub>Fe<sub>0.72</sub>□<sub>0.04</sub>)O</b> <sup>4</sup>	151(1) GPa <sup>4</sup>	5.6(3) <sup>4</sup>	-

<sup>1</sup>Fei 1999, <sup>2</sup>Suzuki 1975, <sup>3</sup>Hazen 1981, <sup>4</sup>Jacobsen et al. 1999, <sup>5</sup>Fei 1995.

Studies on the elastic properties of magnesiowüstite show that the properties of Fe<sup>2+</sup> and Mg<sup>2+</sup> (such as ionic radii) may differ more at high pressures and temperatures, and the divergence would be more pronounced in the case of a high spin to low spin transition for Fe<sup>2+</sup> (Jacobsen et al. 2002). If Fe<sup>2+</sup> and Mg<sup>2+</sup> no longer substituted for each other in the octahedral site, it might be possible that a Fe-rich phase such as B8-structured FeO would exsolve from Mg-rich ferroperricline. As a consequence, an observable seismic discontinuity might occur in the Earth's lower mantle.

Experimental *in situ* studies (Lin et al. 2003) performed at lower mantle pressures and temperatures show that (Mg,Fe)O ferroperricline is stable in the B1 structure in the lower mantle. Ferroperricline in the lower mantle will exchange elements with (Mg,Si) perovskite as a function of P and T. Additionally, it was observed that (Mg,Si) perovskite and liquid iron can react and has FeO as a product. It is possible that (Mg,Fe)O ferroperricline chemically reacts with FeO at the core–mantle boundary. Such a reaction would destabilize FeO in the core–mantle boundary region and therefore remove FeO from the outer core. As a consequence, silicate material would be accumulated at the core–mantle boundary (Buffett et al. 2000).

## 1. Introduction

### *Fe<sup>3+</sup> incorporation and point defects in (Mg<sub>x</sub>Fe<sub>1-x</sub>)O*

The point defect microstructure of (Mg,Fe)O is generally dominated by the presence of Fe<sup>3+</sup>, which can occupy the tetrahedrally-coordinated B1 interstitial site at fractional coordinates (¼, ¼, ¼) or substitute for Fe<sup>2+</sup> on the octahedral site. In an oxidizing environment, the Fe<sup>3+</sup> incorporation mechanism is controlled by the substitution of two cations of Fe<sup>3+</sup> for three divalent metal cations, resulting in one octahedral cation vacancy (<sup>V</sup>□) to maintain the charge balance (Hazen and Jeanloz, 1984), according to the following reaction:



In natural ferropericlase, which is able to incorporate a wide range of heterovalent cations such as Cr, Al, Na, the charge balance condition is then given by:

$$x_{\square} = \frac{1}{2} (x_{\text{Fe}^{3+}} + x_{\text{Al}} + x_{\text{Cr}} - x_{\text{Na}}). \quad (2)$$

The amount of cation vacancies (and hence of Fe<sup>3+</sup>) is a function of the oxygen fugacity. It is also well known that at constant oxygen fugacity, the amount of cation vacancies increases with increasing total Fe bulk composition (Spiedel, 1967). The correlation between cation vacancies and total iron concentration can therefore give a measure of the oxygen fugacity conditions.

## **1.2 Earth's interior structure and mineral composition**

Our current information on the Earth's interior comes from studies of the paths of P and S waves travelling through the Earth, the characteristics of earthquakes, as well as from laboratory experiments on minerals and rocks at high pressure and temperature. Other important data on the Earth's interior come from geological observation of surface rocks and studies of the Earth's motions in the Solar System, the Earth's gravity and magnetic fields, and the flow of heat from inside the Earth.

In the interpretation of geophysical observations it is fundamental to relate seismic data to the structure, composition, mineralogy, physical state and dynamics of the Earth's interior. The multiplicity of wave paths highlights the presence of discontinuities in the Earth's interior and plays a key role in determining details of its structure. P- and S-wave velocities increase gradually inwards throughout the Earth, but at certain depths breaks occur in the travel time curves. Each discontinuity in wave velocity - combined with the density variation (Fig 1.4) - is associated with a drastic change in chemical and physical properties which can be interpreted as phase transitions (Agee, 1998). Earth models can be derived by combining free oscillation and body wave data to describe the Earth's interior structure as a function of depth. One example of a widely used Earth model is the Preliminary Reference Earth Model (PREM, Dziewonski and Anderson, 1981).

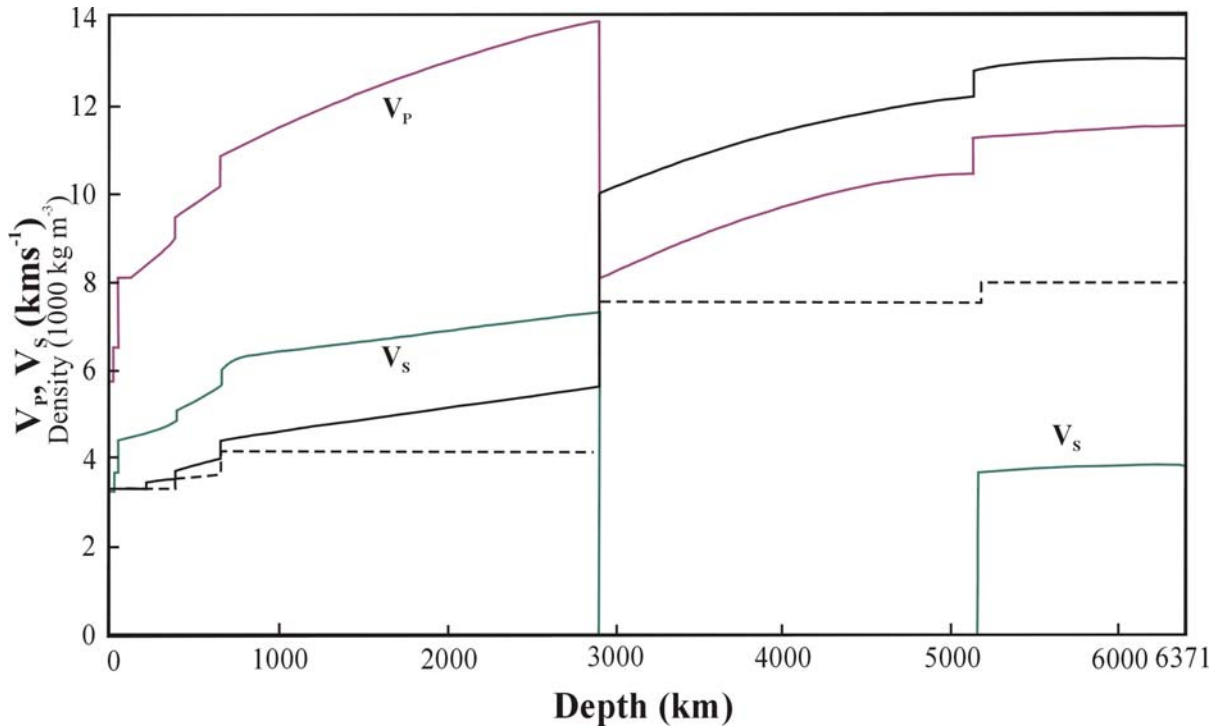


**Fig. 1.4** – P- and S-wave velocities,  $V_P$  and  $V_S$ , in the ak135 model of the Earth developed from body wave travel times (Kennett et al., 1995). The solid black line indicates the density ( $\rho$ ) profile for the Earth model PREM, whereas the black dashed line corresponds to the low temperature density estimated by finite strain theory.

The first order subdivision of the Earth concerns three main shells: the crust, the mantle and the core. Each of them is subsequently divided into additional subdivisions.

The mineral composition of the mantle is mainly represented by silicates, among which olivine is the most abundant upper mantle phase. Two high pressure polymorphs of olivine are involved in the two main seismic discontinuities observed in the transition zone. Two phase transitions take place: olivine transforms into wadsleyite ( $\beta$ -phase) at approximately 410 km in depth and 14 GPa in pressure, defining the upper limit of the so-called Transition Zone (TZ), and subsequently at about 529 km and 17.5 GPa wadsleyite transforms into ringwoodite ( $\gamma$ - phase) (Fig. 1.5).

The lower mantle begins at about 660 km in depth and 24 GPa and 1400-1800°C (Ito and Takahashi, 1989), where ringwoodite ( $(\text{Mg,Fe})_2\text{SiO}_4$ ) breaks down into  $(\text{Mg,Fe})\text{SiO}_3$  perovskite and  $(\text{Mg,Fe})\text{O}$  ferropericlasite. However,  $\text{CaSiO}_3$  perovskite starts to exsolve from garnet at about 18 GPa in the transition zone, while at depths greater than 660 km garnet transforms into

(Mg,Fe)(Al,Si)O<sub>3</sub> perovskite. The most abundant phase of the lower mantle is (Mg,Fe)(Si,Al)O<sub>3</sub> perovskite. Since the lower mantle is half of the Earth by volume, (Mg,Fe)(Si,Al)O<sub>3</sub> perovskite is considered to be the most abundant mineral phase in the Earth (Fig. 1.5).

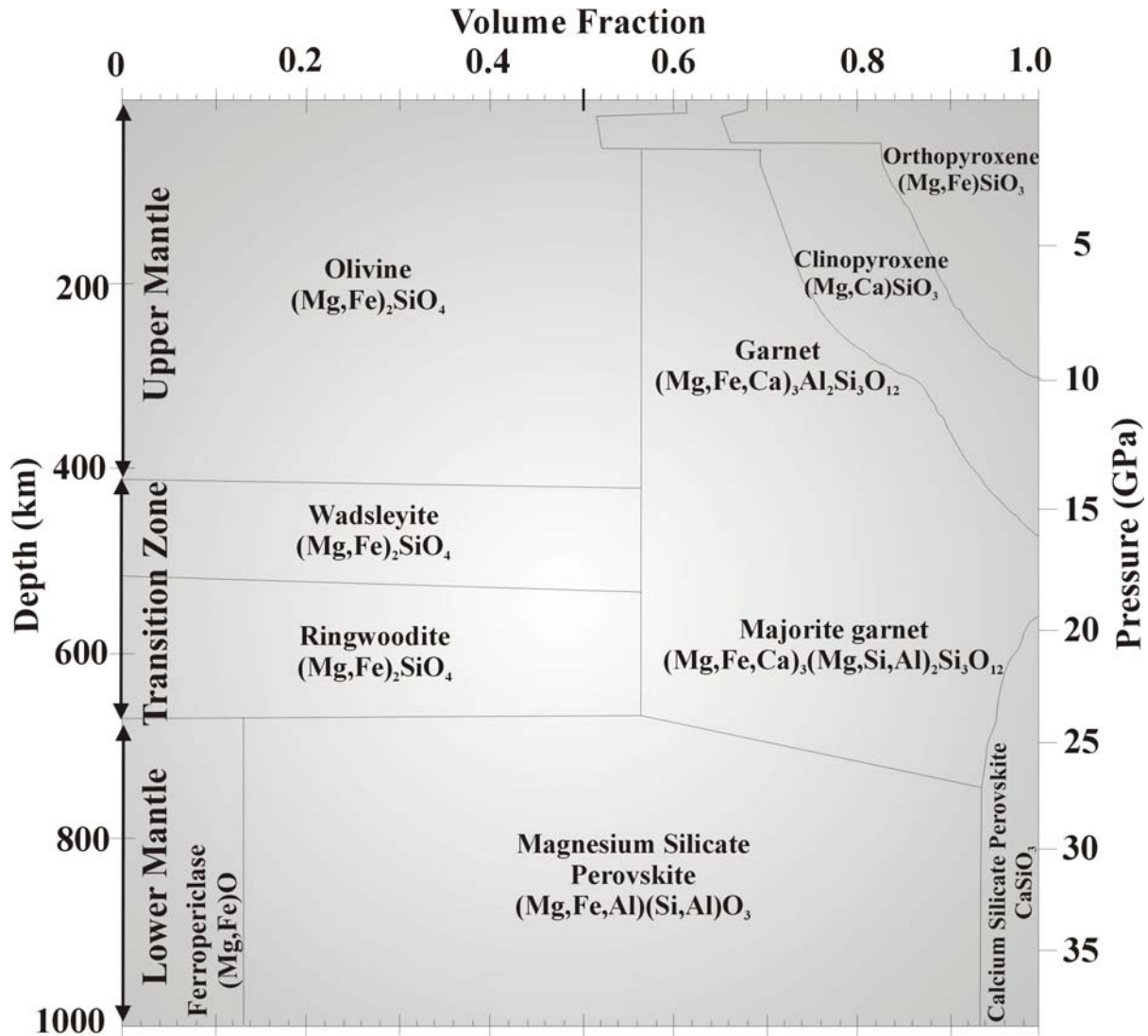
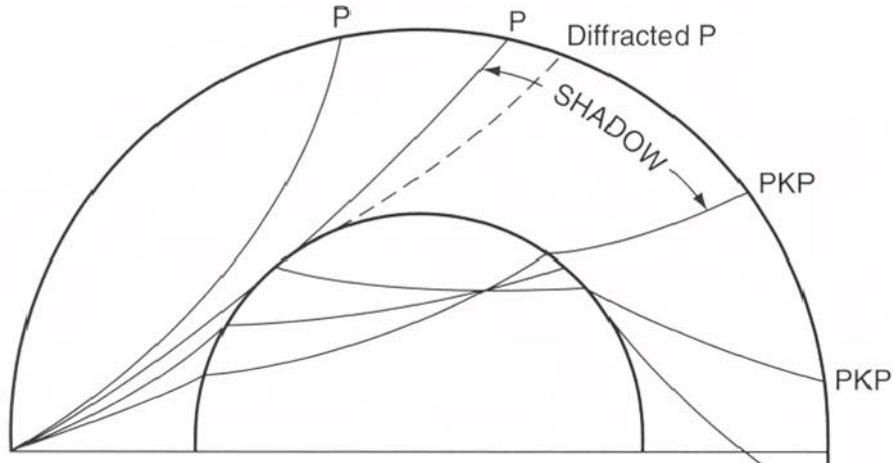


Fig. 1.5 – Mineral composition of the Earth's interior (upper 1000 km) as a function of depth and volume fraction based on a pyrolite composition (modified from Frost 2008).

At a depth of 2900 km and 136 GPa, the Core-Mantle Boundary (CMB) is defined by a P-wave velocity drop to less than 60% of its value at the base of the mantle, causing sharp downward refraction of the P-waves and leading to a shadow zone of distances over which direct P-waves are not observed (Fig. 1.6).



**Fig. 1.6** – Seismic rays refracted by the core, causing a shadow zone for direct P waves (From Stacey and Davis, 2008).

The CMB region is the seat of energetic exchanges and couplings between core and mantle that is of importance to mantle dynamics. Global seismological Earth models exhibit a zone of reduced or even negative velocity gradients (Lay, 1989, 1995) extending for 200 to 300 km above the CMB, called the D'' layer. Numerical simulations lead to the picture of the D'' layer as an unstable thermal boundary layer over the depth of which the temperature-dependent viscosity can decrease by several orders of magnitude and give rise to convective instabilities, or plumes (Loper, 1984; Zharkov et al., 1985; Olson et al., 1987). Chemically denser material of presumably lithospheric origin (or materials risen from the core) may lie at the bottom of the mantle, interacting with convection and modulating the heat flow from the core (Davies and Gurnis, 1986). The base of the D'' layer seems to be characterized by extremely low velocities. This region contains ultra low velocity zones (ULVZs) whose origin is still controversial. Possible explanations could be due to temperature effects (possibly accompanied by partial melt) or a variation in composition as silicate perovskite and ferropericlase interact with the molten iron alloy of the core (Williams et al. 1987; Urakawa et al., 1987; Knittle and et al., 1986; Knittle and Jeanloz, 1989; Goarant et al., 1992; Song and Ahrens, 1994). Recent studies suggest that the D'' discontinuity may be caused by the transition of perovskite into the post-perovskite phase (ppv) occurring at the base of the mantle (Murakami et al., 2004). The low seismic velocities of the iron-rich ppv absorbing iron from the core are in fact consistent with the ULVZs (Mao et al., 2006).

## 1. Introduction

The core is divided into an outer shell (from 2900 to 5200 km depth) and an inner shell (5200 to 6370 km), with pressures up to 360 GPa. Seismic data revealed that the outer core is in the liquid state (S waves do not pass through), whereas the inner core is solid. Despite previous theories which suggested that the core, like the mantle, would also be composed of silicate phases (Ramsey, 1949), it is now well accepted that the core is mainly formed by iron. In addition, by analogy with iron meteorites and from cosmic abundance considerations, it is reasonable to assume the presence of 4-5 wt.% of nickel in the Earth's core. According to density and seismic velocities, however, iron cannot be the only constituent of the outer core, since it would correspond to a density of about 10% higher than what is observed. Thus, iron-nickel would require to be alloyed with small quantities of light elements. In order to be eligible to be incorporated at the time of core formation, the hypothetical light elements must have been relatively abundant (on the order of a few percent by weight), and have low volatility and show siderophile behavior (iron-like). On the basis of these considerations, oxygen and silicon are currently considered to be the major light elements present in the core. In fact, experimental studies (Knittle and Jeanloz, 1986) demonstrated that FeO becomes metallic at pressures above 70 GPa and therefore could be incorporated into the iron core. Sulfur is also considered a good candidate as it can easily partition into iron and forms a low melting-point eutectic (Rama Murthy and Hall, 1970). Carbon and possibly hydrogen might also be present in small amounts (Wood, 1993), although there would have been a strong loss of such elements during core formation due to their high volatility. The light elements would partition into the liquid phase during crystallization of the iron alloy at the outer core-inner core boundary. The lighter liquids could then rise and initiate "compositional convection", which is believed to play an important role in the generation of the magnetic field (Braginsky, 1964; Loper, 1978).

Seismic data indicate that the inner core is solid, consisting essentially of iron. It is still impossible to access whether the inner core iron phase is hexagonal close packed ( $\epsilon$ ), double hcp or orthorhombic ( $\beta$ ), or something else ( $\alpha'$ ). However, it seems probable that it is not face-centered cubic ( $\gamma$ ), as there is good evidence that its stability field does not extend to such high pressures.

Crystallization of liquid alloy leads to a more pure solid phase and a liquid enriched in light elements. Pure liquid iron is around 3-6% denser than the inner core (Anderson and Ahrens,

1994). Therefore a certain amount of light elements is needed in the inner core to achieve a density in agreement with seismic velocity data (Jephcoat and Olson, 1987).

The inner core is characterized by a strong seismic anisotropy in which the P-wave velocity is higher (about 3-4 % faster) along the Earth's rotational axis than in the equatorial direction (Jeanloz, 1990; Tromp, 2001). Body waves travelling parallel to the Earth's rotation axis arrive faster than waves travelling in the equatorial plane. The possible explanation for this phenomenon is a percentage of cylindrical anisotropy with the fast axis parallel to the Earth's rotation axis and the slow axis in the equatorial plane. Solid state convection, solidification texturing, anisotropic growth of the inner core and the Earth's magnetic field are four mechanisms that have been suggested as a possible interpretation of inner core anisotropy. However, lattice-preferred orientation of the hcp iron crystals currently seems to be the most likely explanation for the inner core anisotropy (Dubrovinsky and Lin, 2009). A seismic anisotropy of 3-4% in the core would lead to the conclusion that a high amount of hcp crystals must be preferentially oriented, resulting in the presence of a gigantic iron crystal in the inner core.

### 1.3 Diamonds from the lower mantle

Diamonds require a minimum depth of 150 km to form in the upper mantle. The vast majority of diamonds mined from primary deposits in kimberlite and lamproite pipes and from secondary deposits derived through erosion and redeposition originated from a narrow depth window between about 140 and 200 km (where the P,T conditions are favorable for the transition graphite-diamond), as indicated by calculations of temperature and pressure of formation of their silicate inclusions. The bottom end of this depth range coincides with the “normal” maximum thickness of lithosphere. Such substantial thicknesses of lithosphere are only achieved beneath the oldest parts of continents, the cratons (Fig. 1.7).

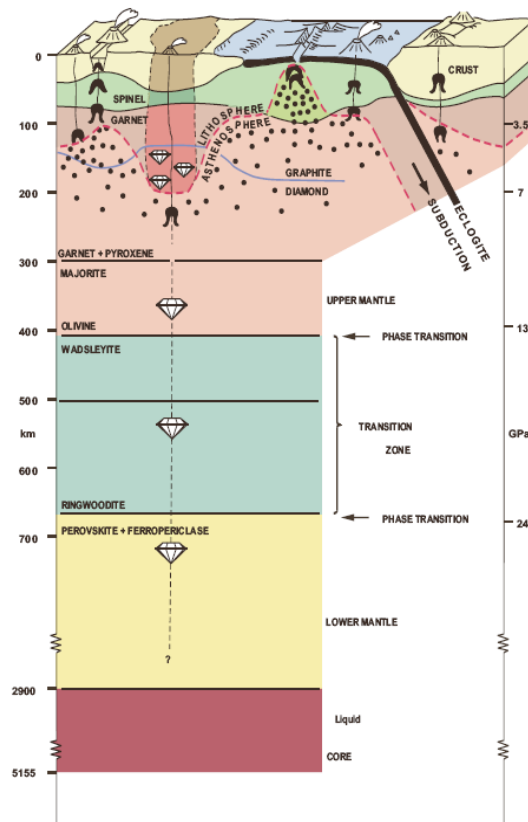


**Fig. 1.7** - Vertical section through Earth’s crust, mantle and core. Beneath ancient cratons the lithosphere may extend to about 200 km depth. In cooler regions of Earth’s mantle the graphite/diamond transition occurs at shallower depth. Beneath cratons, therefore, there is a region where lithosphere and diamond stability overlap and this is the main source region of diamonds worldwide. Rare ultradeep diamonds may come from (i) the deep upper mantle, where majorite garnet becomes stable, (ii) the transition zone, characterized by the stepwise isochemical conversion of olivine first to wadsleyite and then to ringwoodite, and (iii) the lower mantle (from Stachel et al., 2005).

## 1. Introduction

Diamond inclusions reflect the chemical composition and mineral assemblages of the two principal rock types occurring in the deep lithosphere, peridotite and eclogite (e.g., Meyer 1987). However, in the past decades diamonds have been found forming also at transition zone and lower mantle depths. The idea that diamonds could contain tiny inclusions from the lower mantle came in 1984 when ferropericlase was found for the first time in diamonds recovered from kimberlite dikes near Orroroo in South Australia (Scott-Smith et al. 1984). More than ten years later a lower mantle origin for diamonds carrying ferropericlase inclusions was generally accepted (Harte et al., 1999; Davies et al., 1999; Stachel et al., 2000). Since then, twelve localities worldwide have been identified which indicate the presence of lower mantle inclusions inside diamonds (Fig. 1.8), in particular the Juina area in Brazil (Harte et al., 1999), the DO-27 pipe at Lac de Gras in Canada (Davies et al., 1999) and Kankan area in Guinea (Stachel et al., 2000).

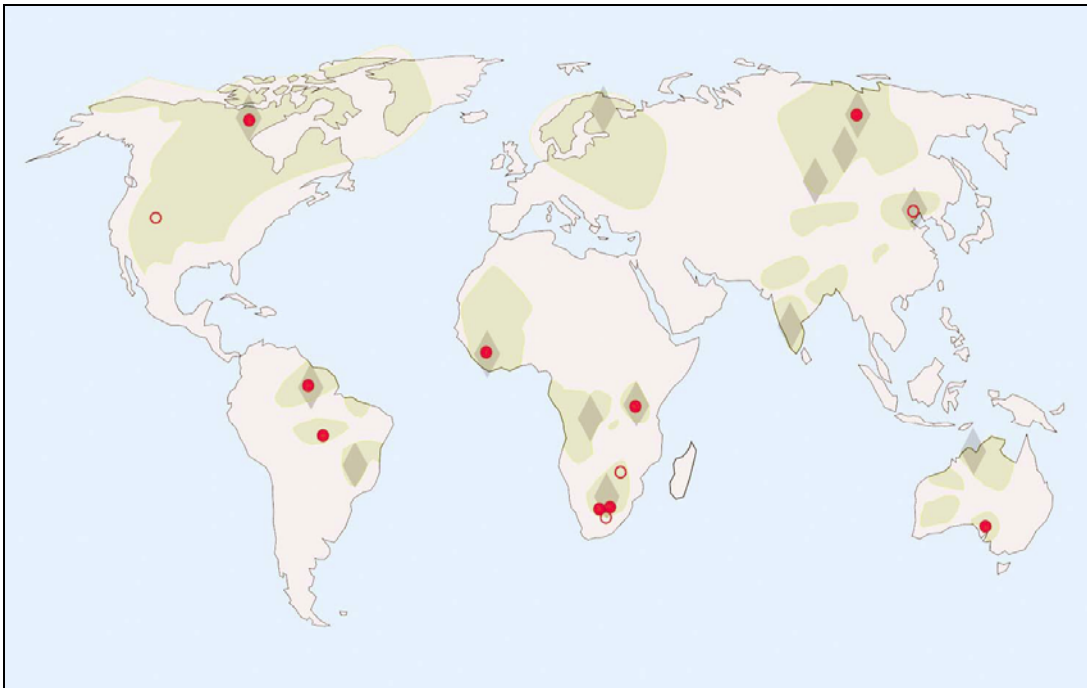


**Fig. 1.8** – Worldwide distribution of deposits with occurrence of superdeep diamonds (solid red circles) and potential lower mantle diamond sources (open red circles). The light grey areas indicate the global distribution of cratons, while dark grey diamonds indicate major diamond deposits (*from McCammon, 2001*).

## 1. Introduction

Trace element studies conducted on Ca,Si-perovskite inclusions from the lower mantle showed a high level of LREE concentrations and Eu anomalies. This would imply a highly enriched lower mantle source, suggesting that those diamonds were not formed from primitive mantle, but from former oceanic slabs accumulated at the topmost region of the lower mantle (the first 10-20 km) (Stachel et al., 2005), according to the “megalith model” proposed by Ringwood (1991) (Fig. 1.9). This is also supported by considerations of the low Al contents of the Mg,Si-perovskites, as the Al solubility in perovskite is predicted to be low at the topmost region of the lower mantle. Walter et al. (2008) suggested that silicate mineral inclusions in lower mantle diamonds recovered from Juina (Brazil) crystallized from primary and evolved carbonatite melts in the transition zone and deep upper mantle. Diamond growth is generally favored in regions of redox gradients (Deines, 1980), which may provide a clue to its origin in the lower mantle. The introduction of oxidized subducted material into reduced lower mantle could generate redox fronts that provide conditions favorable for diamond growth (Stachel, 2001).

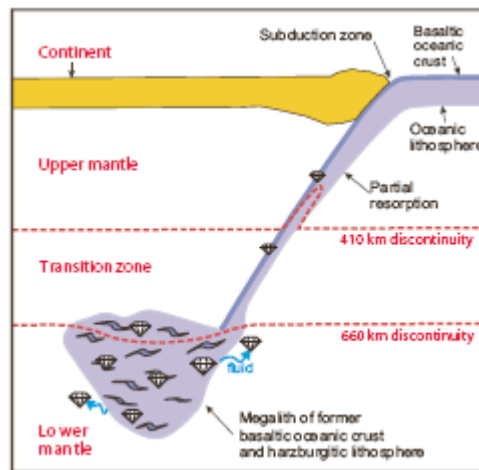


**Fig. 1.9** – The so called “megalith model” of Ringwood (1991) (from Stachel et al., 2005).

In most diamonds, nitrogen is a major impurity at concentrations between a few atomic ppm and 5000 atomic ppm (Bibby, 1982). Based on this, diamonds are classified as a function of nitrogen content as Type I (high N concentration) and Type II (low N concentration). Mostly all of the diamonds from the lower mantle belong to the second type, indicating very low N concentration. Therefore, N content can be considered one good indicator in distinguishing

## *1. Introduction*

diamonds from upper and lower mantle. Geochemical evidence supports the theory of the lower mantle as a nitrogen reservoir, and this implies that nitrogen is therefore not incorporated into diamonds during diamond formation, or alternatively was lost during core accretion.

The discovery of lower mantle inclusions in diamonds represents the only chance to directly investigate lower mantle chemistry, oxygen fugacity, and physical and chemical properties of the lower mantle mineral phases, even though these parameters reflect only conditions during diamond formation, and not the bulk lower mantle itself.

It is believed that the chemistry of mineral phases tends to be preserved by diamonds at the time of their formation. Diamonds from the lower mantle carry inclusions that largely conform to a composition and mineralogy of the deep mantle based on a “pyrolite” (primitive peridotitic) model. At the present, ferropericlase, stishovite (high pressure SiO<sub>2</sub>-phase), TAPP (Tetragonal Almandine-Pyrope Phase, Harris et al. 1997), Mg and Ca silicate perovskite and enstatite are the most common mineral phases discovered so far as diamond inclusions. Magnetite, native Fe and magnesioferrite are also sometimes found. Ferropericlase inclusions are often found to be associated with secondary magnetite-magnesioferrite (Hutchison 1997, Hayman et al., 2005).

Magnetite associated with native iron rimmed by wüstite was found to coexist in a diamond from Mwadui, Tanzania (Stachel et al. 1997). Magnetite inclusions are believed to be rare and of unknown paragenesis (Meyer 1987), and potentially associated with fluid precipitation along cracks into diamonds. Wüstite inclusions of unknown paragenesis are described as central inclusions (seeds) in Yakutian diamonds (Bulanova 1995). Native iron has previously been described as an inclusion in diamond from Yakutia (Sobolev et al. 1981) and the Sloan kimberlites (Meyer and McCallum 1986). The coexistence of native iron, wüstite and magnetite in the same diamond indicates a variation in oxygen fugacity from below WI (FeO-Fe) to above MW (Fe<sub>3</sub>O<sub>4</sub>-FeO) and might be indicative of ultra-deep origin. Sulfides are also commonly recognized in the ultra deep paragenesis (Bulanova et al., 2008). However, the role of sulfides in diamond genesis is not yet completely clear.

## 1.4 Ferropericlase as a diamond inclusion

Ferropericlase is the most prominent lower-mantle inclusion in superdeep diamonds. Under the microscope, it shows a petrol-brownish color, which makes it easy to recognize. Ferropericlase was found as a diamond inclusion in the early 1980s and considered to be an indicator of lower mantle origin of the host diamond (Scott-Smith et al., 1984). (Mg,Fe)O is preserved during exhumation because it is stable over the entire mantle pressure range, but in the presence of low-Ca pyroxene at depths above the lower mantle, it may react to form olivine (either in  $\beta$  or  $\gamma$  phase). Ferropericlase is absent in common upper mantle rocks, which might indicate that all ferropericlase inclusions in diamonds were formed at lower mantle conditions. However, it is only the coexistence of ferropericlase with pure perovskite inclusions that can be uniquely attributed to a lower mantle origin. Such a paragenesis in fact cannot have formed outside the lower mantle, since at lower pressures (Mg,Fe)O would react with silicate phases to form olivine and pyroxene compositions. In addition, experimental studies conducted on the solubility of sodium in ferropericlase at upper mantle pressure conditions show that Na can be incorporated in amounts normally measured in natural diamond inclusions. Those results suggest that the typically lower mantle phase ferropericlase might be present in the upper mantle in regions with low silica activity (Brey et al., 2004).

Experimental studies on pyrolite compositions showed that the Mg-number [ $\text{Mg}/(\text{Mg}+\text{Fe})$ ] characterizing lower mantle ferropericlase should be about 84-85. Studies on natural ferropericlase inclusions show Mg-numbers predominantly of 85-88, in accordance with experimental results. However ferropericlase inclusions from Juina (São Luiz, Brazil) differ significantly in Mg number, showing a very large range from 36 to 87. Theories about the iron-rich nature of the inclusions from Juina suggest a possible origin from Fe-enriched mantle regions located near the core-mantle boundary (Harte et al. 1999), or possibly derived from non-pyrolitic lower mantle sources (e.g. ancient subducted oceanic crust).

Ferropericlase is a stable phase in a wide range of temperatures and pressures throughout the mantle; therefore it has a strong tendency to incorporate several heterovalent cations in its structure. The chemistry of ferropericlase inclusions recovered from lower mantle diamonds includes reasonable concentrations of Na, Ni and Cr.

Ni concentrations differ significantly between lower mantle mineral assemblages and the ones formed at shallower depths (Stachel et al., 2000). In fact, the Ni contents of Ca and Mg silicate perovskite in diamond inclusions are on the order of <0.06 wt% NiO, while corresponding upper mantle enstatites can contain between 0.1 to 0.2 wt% NiO (Kesson and Fitz Gerald, 1991). Moreover, experimental results show that at high pressure Ni has more affinity for the ferropiclasite structure than for Mg silicate perovskite, ranging from 0.08 to 1.46 wt.% NiO for the Kankan (Guinea) inclusions (McCammon et al., 2004b), which is very similar to values reported for São Luiz and Juina area inclusions. However, Ni concentrations in ferropiclasite are not necessarily diagnostic of lower mantle origin.

Cr is also relatively abundant in natural inclusions, ranging from 0.11 to 1.75 wt%Cr<sub>2</sub>O<sub>3</sub>. Cr is assumed to be in its trivalent state, but recent XANES studies have shown evidence that divalent chromium is present with different Cr<sup>2+</sup>/Cr<sup>3+</sup> ratios in lower mantle ferropiclasite (Otake et al., 2008). Variation in the Na content is also notable, ranging from 0.01 to 1.35 wt% Na<sub>2</sub>O. The highest values are reported for inclusions recovered from the Juina area (Brazil), São Luiz (Brazil), Rio Soriso (Brazil), and Guinea.

### **1.5 Oxygen fugacity in lower mantle diamonds and the determination of the Fe<sup>3+</sup>/ΣFe ratio**

Many questions are still open regarding the oxygen fugacity in the lower mantle. Lower mantle diamonds represent our direct window to study the lower mantle. Previous studies have been conducted on *in situ* Fe<sup>3+</sup>/ΣFe measurements on inclusions from lower mantle diamonds, in particular Mg,Si perovskite and ferropiclasite (Mg,Fe)O, with the aim to provide information regarding lower mantle oxygen fugacities in the region where diamonds formed (McCammon et al., 1997; McCammon et al., 2004b). Silicate perovskite, which is the main phase of the lower mantle, shows very high Fe<sup>3+</sup>/ΣFe ratios even in reducing environmental conditions in equilibrium with iron metal (Frost et al., 2004a). Therefore, perovskite is a poor redox sensor for lower mantle diamonds and our attention must turn to (Mg,Fe)O, the second most abundant phase of the lower mantle and the most abundant phase in lower mantle diamond inclusions (more than 50% of occurrences).

## 1. Introduction

The main difficulty related to the study of lower mantle diamonds is due to the very small size of such inclusions ( $< 50 \mu\text{m}$ , commonly on the order of  $20\text{-}30 \mu\text{m}$ ). Therefore, it is necessary to improve and develop new techniques to measure  $\text{Fe}^{3+}/\Sigma\text{Fe}$  in order to study the oxygen fugacity during lower mantle diamond formation. So far, the potential experimental techniques which can be used to determine  $\text{Fe}^{3+}/\Sigma\text{Fe}$  in diamond inclusions are Mössbauer spectroscopy, Electron Energy Loss Spectroscopy (EELS), X-ray Absorption Near Edge Structure spectroscopy (XANES), X-ray photoelectron spectroscopy (XPS) and soft  $L\beta$  and soft  $L\alpha$  emission spectra:

- Mössbauer spectroscopy (MS): This technique is the most commonly used method for measuring  $\text{Fe}^{3+}/\Sigma\text{Fe}$ . However in its conventional form it requires large homogeneous samples, and it provides optimal results for mantle compositions with sample amounts greater than 100 mg. Recent advances have enabled *in situ* Mössbauer measurements to be performed to determine  $\text{Fe}^{3+}/\Sigma\text{Fe}$  on single mineral grains of  $\sim 100\text{-}200 \mu\text{m}$  in size (McCammon, 1994; McCammon, et al. 1997; Sobolev et al. 1999). Mössbauer spectroscopy has the advantage to provide information about site occupancies, including sites in which electrons may become delocalized. However, both macro- and micro-Mössbauer measurements are affected by recoil-free fraction effects (Grant, 1995) and thickness effects (Rancourt et al., 1993), and they require long data collection times (minimum 1-2 days).

- Electron Energy Loss Spectroscopy (EELS): Transmission Electron Microscopy (TEM) offers the best spatial resolution for determining *in situ*  $\text{Fe}^{3+}/\Sigma\text{Fe}$  using EELS, since it allows measurements to be made at the nano-scale (Garvie and Craven 1994; Golla and Putnis 2001; van Aken and Liebscher 2002; van Aken et al. 1998, 1999). The absolute error for  $\text{Fe}^{3+}/\Sigma\text{Fe}$  is considered to range between  $\pm 0.02$  and  $\pm 0.04$ , depending on the evaluation method chosen for interpreting the spectra.

- XANES (X-ray Absorption Near Edge Structure spectroscopy): Advantages include the possibility of *in situ* measurement of the  $\text{Fe}^{3+}/\Sigma\text{Fe}$  ratio on a micrometer scale (currently better than  $10 \times 15 \mu\text{m}^2$  for intense synchrotron sources, with  $< 30 \mu\text{m}$  sampling depth), and the possibility to obtain information regarding the coordination state (Calas et al., 1984; Chen et al., 1984; Brown and Parks, 1989, Delaney et al., 1998). Further

## 1. Introduction

advantages of this method are the significantly reduced counting times (minimum 20-30 min) compared to Mössbauer spectroscopy, and the possibility to study transition elements other than iron. However, quantitative calibrations have been complicated by the fact that variations in the Fe coordination environment affect both the energy and intensity of spectral features, requiring the use of compositionally similar standards. Recently, Berry et al. (2003) found that the coordination substantially affects the accuracy of results, so that regression equations based on pre-edge ratios are reasonable and consistent with Mössbauer data only as long as both the  $\text{Fe}^{3+}$  and  $\text{Fe}^{2+}$  cations are in octahedral coordination (Delaney et al., 1998); however they may deviate significantly and even become physically meaningless if Fe changes coordination. Nevertheless, the potential impact of XANES in numerous research fields has motivated a continued effort to develop quantitative calibration curves, and to extend the calibration to further systems relevant to geosciences. Despite the advantages of XANES, however, a limitation is the need for access to a synchrotron facility.

- X-ray photoelectron spectroscopy (XPS, Raeburn et al. 1997a, 1997b): Results from this technique are in excellent agreement with wet-chemistry, MS, and XANES, but the method is surface-sensitive and requires a particular sample preparation procedure to preserve the original oxidation state.

- Measurement of the soft  $\text{FeL}\alpha$  and  $\text{FeL}\beta$  X-ray emission spectra by Electron MicroProbe (EMPA) using the so-called Flank Method: Many studies have been conducted during the past decades to develop this technique and make it available to measure *in situ*  $\text{Fe}^{3+}/\Sigma\text{Fe}$  plus major element analysis. The basic principle is that in the X-ray emission spectra of transition metals, the  $\text{L}\alpha$  and the  $\text{L}\beta$  peaks and also the  $\text{L}\beta/\text{L}\alpha$  intensity ratios shift with changes in oxidation state (Fisher, 1965). Results obtained with the flank method show a correlation with Mössbauer results with respect to quadrupole splitting (QS) and crystallographic data (Höfer, 2002). This technique shows a slightly lower resolution with respect to hyperfine parameters compared to other methods such as Mössbauer spectroscopy or XANES. Nevertheless, it has several advantages: high spatial resolution due to the small sampling volume ( $\leq 1\mu\text{m}^3$ , spot beam size) and therefore only a small sample is needed (in the range of the beam size of 1 to 10  $\mu\text{m}$ , which is

significantly smaller compared to Mössbauer spectroscopy), and the routine and nondestructive sample preparation. The flank method offers also the advantage of a relatively short measuring time: depending on the iron content of the samples, each point requires 5 minutes for iron oxides (~70 wt-% Fe) and 10-20 min for other oxides containing less iron ( $\geq 10$  wt-%) (Höfer et al. 1994). Further advantages are the possibility to perform *in situ*  $\text{Fe}^{3+}/\Sigma\text{Fe}$  measurements simultaneously with major element analysis, and the wide availability of electron microprobe instruments.

### 1.6 The “flank method”: state of the art

Conventional measurements using electron microprobe analysis do not allow the determination of valence states for transition elements such as Fe. In previous studies  $\text{Fe}^{2+}$  and  $\text{Fe}^{3+}$  have been often estimated indirectly through the use of stoichiometry considerations. However, phases are not always stoichiometric, so calculating the  $\text{Fe}^{3+}$  content using electron microprobe chemical composition data can result in a large imprecision on the final  $\text{Fe}^{3+}/\Sigma\text{Fe}$  value. For this reason, the development of the flank method is an important contribution to mineralogy and geosciences. The interest in using the X-ray emission spectra to determine the  $\text{Fe}^{3+}/\Sigma\text{Fe}$  ratio in minerals started in the early 1970s (Albee and Chodos, 1970; O’Nions and Smith, 1971; Pavicević et al., 1972, 1989, 1992; Grassergauer, 1975a, b; Dodd and Rippe, 1978; Legkova et al., 1982).

Over the past two decades the flank method has been strongly improved and the  $L\beta/L\alpha$  ratio as a function of Fe bulk composition (wt.%) has been intensively studied for wüstite, magnetite and hematite (Höfer et al., 1994, 2000), garnet (Höfer et al., 1995; Höfer, 2002), sodic amphiboles (Enders et al., 2000), basaltic glasses (Fialin et al, 2001) and Ti-rich amphiboles (Wagner et al., 2008). The calibration curve for spinels has also been tentatively established (Berlin et al., 2004); preliminary *in situ* results pointed out that the huge range of compositional, structural and bonding effects may change the shape of the FeL lines. So far, a complete calibration of the flank method is available only for garnets (Höfer and Brey, 2007).

The “flank method” is based on the measurement of the soft FeL $\alpha$  and FeL $\beta$  X-ray emission spectra by electron microprobe. The shift of the L $\alpha$  peak between  $\text{Fe}^{2+}$  and  $\text{Fe}^{3+}$  can be measured with the electron microprobe and hence exploited to determine the  $\text{Fe}^{3+}/\Sigma\text{Fe}$  ratios (Fig.1.10).

Three different approaches have been explored to determine  $\text{Fe}^{2+}/\text{Fe}^{3+}$  by electron microprobe (Höfer et al. 1994):

- *Peak shift method*: the shift in wavelength with changing  $\text{Fe}^{2+}/\text{Fe}^{3+}$ ;
- *Peak area method*: the change in intensity ratios of fitted peak areas  $\text{FeL}\beta/\text{FeL}\alpha$ ;
- *Flank method*: combines the peak shift method and the peak area method by measuring intensity ratios of certain portions of the peak flanks ( $\text{cpsL}\beta/\text{cpsL}\alpha$ ), i.e., the ratio of intensities on the low energy flank of the  $\text{L}\beta$  band and on the high-energy flank of the  $\text{L}\alpha$  band, which is where the differences between  $\text{Fe}^{2+}$  and  $\text{Fe}^{3+}$  are the largest.

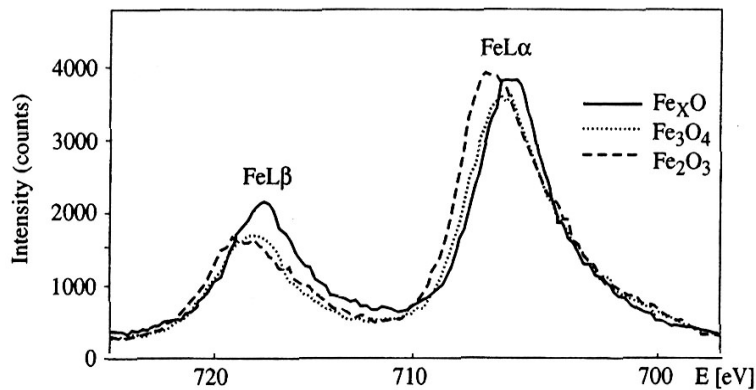


**Fig. 1.10** – FeL emission spectra of iron oxides  $\text{Fe}_x\text{O}$ ,  $\text{Fe}_3\text{O}_4$  and  $\text{Fe}_2\text{O}_3$  measured at 10kV and 50 nA (from Höfer et al., 1994).

Of the three methods, the flank method offers the highest accuracy. The error in the determination of  $\text{Fe}^{3+}/\Sigma\text{Fe}$  in iron oxides using the peak area method is 0.07, versus 0.02 ( $1\sigma$ ) for the flank method (Höfer et al., 1994). The measurements are performed at fixed spectrometer positions on the  $\text{FeL}\beta$  and  $\text{FeL}\alpha$  flanks (Fig 1.11). When possible, data can be collected simultaneously on two different spectrometers to improve the counting statistics.

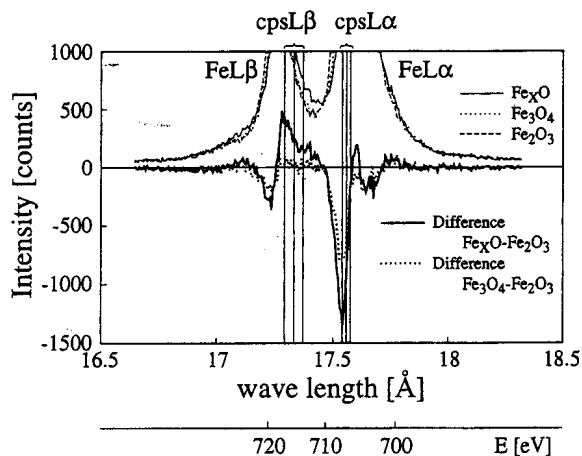


**Fig. 1.11** – Difference spectra (lower curves) of the FeL emission spectra for  $\text{Fe}_x\text{O}$ ,  $\text{Fe}_3\text{O}_4$  and  $\text{Fe}_2\text{O}_3$ . The vertical lines indicate the measuring positions  $L\beta$  and  $L\alpha$  of the flank method (from Höfer *et al.*, 1994).

A new method was developed for self-absorption correction and matrix effects (Höfer and Brey, 2001). Results obtained on the flank method for garnet show a correlation with Mössbauer results with respect to quadrupole splitting (QS) and crystallographic data, and a strong correlation between the  $\text{Fe}L\beta/\text{Fe}L\alpha$  ratio and the  $\text{Fe}^{3+}$  content (Höfer, 2002).

Despite the advantages offered by this method, there are complexities related to the calibration procedure; therefore, the flank method is not yet a routine method. The FeL emission spectra, which are the basis for the flank method, are not only sensitive to  $\text{Fe}^{2+}/\text{Fe}^{3+}$ , but are also affected by the electronic environment of the iron atoms (i.e., the coordination polyhedra and the crystal structure). Moreover, parameters such as spectrometer reproducibility and stability of the beam current during the measurements need to be monitored carefully (Berlin *et al.*, 2004). Since the low energy Fe  $L\alpha$  and the Fe  $L\beta$  X-ray emission lines are also affected by bulk chemistry and crystal structure, it is necessary to establish separate calibration curves for each mineral group. However, in cases for which high spatial resolution is needed, this tool is able to provide useful data on  $\text{Fe}^{2+}/\text{Fe}^{3+}$  ratios down to a minimum FeO bulk content of 3-4 wt%.

## 1.7 Aim of the project

Although physical and chemical properties of the upper mantle can be constrained by direct and indirect observations, many parameters are not yet known about the lower mantle. The only direct information regarding the lower mantle is provided by diamonds originating in the deep Earth that are carried to the surface by mantle convection and kimberlite eruption. The mineral inclusions in such diamonds can therefore provide information regarding the conditions under which the diamonds crystallized (e.g. P, T,  $f_{O_2}$  and  $f_{S_2}$ ).

I therefore undertook a study to develop an in-house experimental technique able to measure these inclusions, namely the flank method involving the electron microprobe. As discussed above in comparing different techniques, the flank method offers a good compromise between advantages and disadvantages.

The research strategy of this thesis comprises two different steps: first the calibration of the flank method on synthetic (Mg,Fe)O of known bulk composition and  $Fe^{3+}/\Sigma Fe$  ratios and then application of the calibration to natural samples. Samples of Fe bulk composition ranging from 2 to 40 wt.% and  $Fe^{3+}/\Sigma Fe$  ratios from 1 to 15% were synthesized in order to explore the behavior of  $L\beta/L\alpha$  ratios measured by flank method as a function of  $\Sigma Fe$  and  $Fe^{2+}$  (and hence  $Fe^{3+}$ ) along the solid solution MgO-FeO to establish the calibration for a simplified compositional system. Once the calibration of the flank method was established for synthetic (Mg,Fe)O, a set of natural samples worldwide was used to measure the  $Fe^{3+}/\Sigma Fe$  ratios and evaluate the influence of chemical composition on the flank method.

The study of natural samples provides insight into the mechanism by which (Mg,Fe)O is able to record oxygen fugacity conditions, the oxygen fugacity conditions during lower mantle diamond genesis, and the variation of oxygen fugacity recorded by different lower mantle diamond sources worldwide.

## 2. Experimental methods

### 2.1 Synthesis of (Mg,Fe)O crystals

(Mg,Fe)O ferropericlasite crystals were synthesized in order to cover a wide range of Fe bulk composition ( $x_{\text{Fe}} = 2$  to 78 at.%) and  $\text{Fe}^{3+}/\Sigma\text{Fe}$  (1 to 15%). Reichmann et al. (2000) and Jacobsen et al. (2002) described the synthesis of high quality single crystals of (Mg,Fe)O using the interdiffusion of Fe and Mg between (Mg,Fe)O pre-reacted powders and single crystal MgO, using a method similar to that described by Schaefer and Brindley (1963). However, at the temperature range (1300-1450°C) and the oxygen fugacity range ( $10^{-2}$ - $10^{-5}$  Pa) used, if the oxygen fugacity is not accurately controlled during the experiments, a detectable amount of magnesioferrite may exsolve from the (Mg,Fe)O single crystal, giving rise to chemical impurities in the crystals. Therefore, in order to produce pure (Mg,Fe)O crystals we chose a different approach.

Mg and Fe metals were mixed in stoichiometric proportions in order to obtain (Mg,Fe)O powders over a Fe compositional range of 2-78 at%. The mixtures were enriched in  $^{57}\text{Fe}$  of approximately 10% of the Fe total. Metals were first dissolved in  $\text{HNO}_3$ . The mixture with addition of water (10 ml) was then heated to 50°C to allow  $\text{HNO}_3$  to slowly evaporate. This procedure of adding 10 ml of water and heating up to 50°C was repeated several times. Subsequently liquid  $\text{NH}_3$  was added to obtain oxide precipitates. Excess  $\text{HNO}_3$  and  $\text{NO}_3$  were then removed by drying the obtained gel in a Pt crucible (to avoid contamination with other elements), first using a Bunsen burner (1200-1500°C) and then drying in a conventional oven up to 800°C. The sample was subsequently cooled down to 500°C. The obtained powder was then analyzed by means of X-ray diffraction for phase identification and then re-equilibrated at different oxygen fugacities to obtain various  $\text{Fe}^{3+}/\Sigma\text{Fe}$  ratios.

### 2.2 Gas-mixing furnace

All synthetic powders were equilibrated in a gas-mixing furnace at Bayerisches Geoinstitut (Fig.2.1), under different ratios of  $\text{CO}/\text{CO}_2$  well mixed at 1300°C in order to obtain a wide range of  $\text{Fe}^{3+}/\Sigma\text{Fe}$ . The intended  $\log f_{\text{O}_2}$  for each run was estimated based on the activity-composition relations and oxygen activity at temperature of 1300°C (Srećec et al., 1987;

## 2. Experimental Methods

Giddings and Gordon, 1973). As a result, the oxygen fugacity during the experiments was varied over the  $\log f_{\text{O}_2}$  range from -7 to -11 relative to the Fe-FeO buffer, and in addition to the determination of oxygen fugacity based on the CO/CO<sub>2</sub> gas ratio, it was also monitored during the experiments using an oxygen fugacity sensor.

Polycrystalline (Mg<sub>x</sub>Fe<sub>1-x</sub>)O powders were loaded into a press to form pellets of 1.2 cm diameter. The pellets were attached to a ceramic tube using Pt wire, and then placed into a vertical furnace with the pellet centered at its hot spot (which varied depending on temperature used). The experiments were carried out for 12 hours (sufficient for equilibrating ferropericlase at 1300°C) and the samples were quenched into water in a glass beaker placed at the bottom of the furnace, which ensures a rapid quench and avoids the formation of ferrite crystals. To homogenize the sample, the entire re-equilibration procedure was repeated three times.

Samples were ground into powder for X-ray powder diffraction and Mössbauer spectroscopy measurements to investigate the homogeneity of the newly obtained polycrystalline powders and to measure the  $\text{Fe}^{3+}/\Sigma\text{Fe}$ .

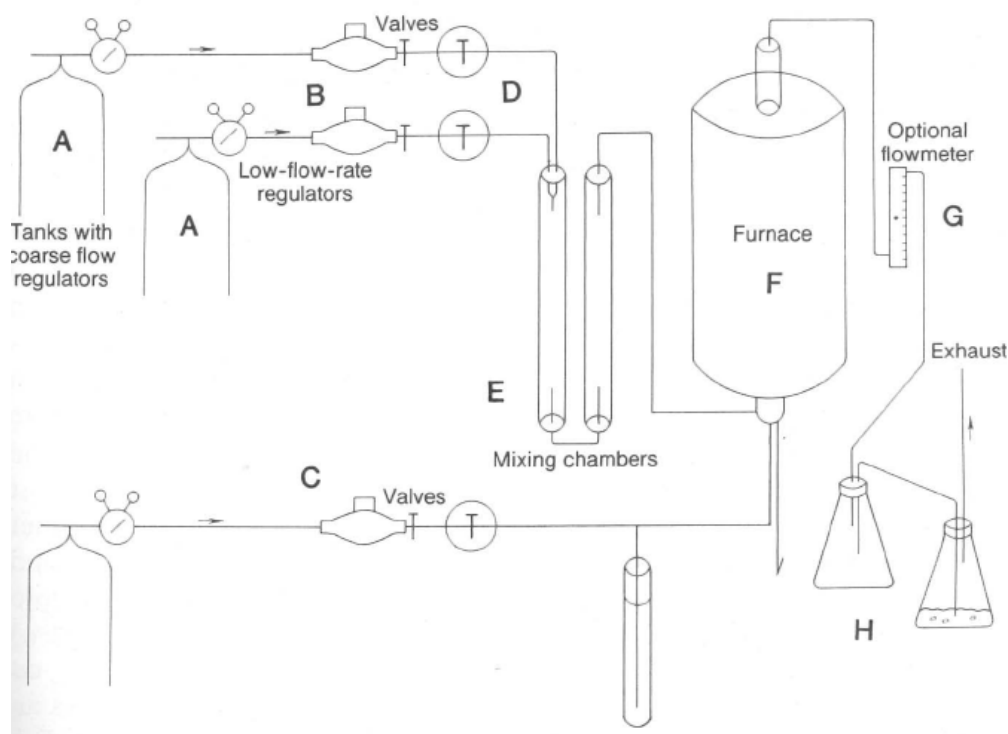


**Fig. 2.1** – Gas-mixing furnace scheme. CO and CO<sub>2</sub> gases flow into a mixing chamber before entering the furnace. The oxygen fugacity inside the furnace is measured using an oxygen fugacity sensor (from Ulmer and Barnes, 1987).

### 2.3 Multi-Anvil Apparatus

In order to obtain crystals with the high quality surface needed for electron microprobe measurements, the polycrystalline powders were transformed to quasi single crystals at high pressure and temperature using a multi anvil apparatus. All experiments were performed by using a Sumitomo press, one of the 6-8 Kawai-types of multi-anvil press (Kawai and Endo, 1970) at Bayerisches Geoinstitut. Details of multi-anvil technique and experimental procedure are given by Rubie (1999).

The (Mg,Fe)O polycrystalline powders were initially loaded into Re capsules (made out of Re foil, 1 mm thick) of 1.6 mm diameter and 2 mm long. Each capsule was then loaded into a 10/5 (octahedral edge length/tungsten-carbide anvil truncation in mm) assembly. The pressure cell consists of several parts: an octahedron made of MgO doped with 5% Cr<sub>2</sub>O<sub>3</sub> and cored to host a heater (Fig.2.2a). A cylindrical ZrO<sub>2</sub> sleeve thermally isolates the MgO octahedron from the LaCrO<sub>3</sub> heater. Two MgO hollow cylinders (each half of the heater's length) are placed inside the heater, and the rhenium capsule is positioned inside them. The bottom of the heater is filled with a MgO solid cylinder, whereas the top hosts a W<sub>3</sub>Re<sub>97</sub>-W<sub>25</sub>Re<sub>75</sub> thermocouple (wire  $\varnothing = 0.25$  mm) within a 4-hole Al<sub>2</sub>O<sub>3</sub> sleeve. The octahedral assembly containing the sample is then placed at the centre of eight corner-truncated tungsten carbide cubes, which represent the first stage anvils (Fig.2.2b). The corner truncations of the eight cubes are covered by pyrophyllite gaskets in order to accommodate the octahedral assembly. The cubes are finally packed together using epoxy impregnated fiberglass laminate sheets in order to ensure electrical insulation from the guided six anvils. At this stage, the cubes containing the octahedral assembly are placed into the press, where they are compressed by six outer tool-steel anvils (second stage anvils), which are driven by a hydraulic press in a uniaxial direction (Fig.2.2c). During the experiment the cubes are compressed to 15 GPa and heated to 1800-2000°C for a maximum time of one hour.

In order to know the variables pressure and temperature during the experiments, we made use of the calibration already established for the press in use (Frost et al. 2004b).

## 2. Experimental Methods

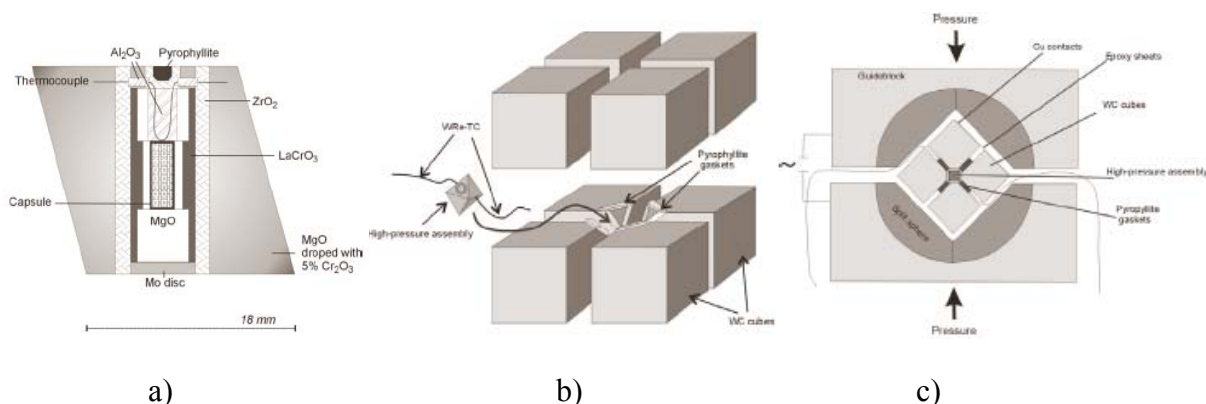


**Fig. 2.2** – Multi anvil apparatus details and sequence of experiment: a) a cross section of a octahedron containing the capsule described with each of its components; b) the 8 corner-truncated tungsten carbide cubes hosting the octahedron in the centre, surrounded by gaskets; c) two guide blocks with six anvils forming a cubic cavity where the 8 cubes will be finally be placed for the experiment (from Gavrilenko, 2008, modified after Rubie, 1999).

### 2.4 Mössbauer Spectroscopy

Mössbauer measurements were performed with the aim to determine the  $\text{Fe}^{3+}/\sum\text{Fe}$  ratios with high accuracy. The value of  $\text{Fe}^{3+}/\sum\text{Fe}$  determined is then used as a standard reference for the electron microprobe analysis in order to correlate the  $L\beta/L\alpha$  ratios and  $\text{Fe}^{3+}/\text{Fe}^{2+}$  concentration in  $(\text{Mg,Fe})\text{O}$ .

A conventional  $^{57}\text{Co}$  source (1.85 GBq over 10 mm diameter) was used to determine  $\text{Fe}^{3+}/\sum\text{Fe}$  for all  $(\text{Mg,Fe})\text{O}$  powders, before and after re-equilibrating in the gas mixing furnace, in order to verify the homogeneity of samples and to rule out the presence of additional phases such as magnetic compounds (magnesioferrite, magnetite) which may affect the flank method measurements. The powders were loaded into a sample holder of 1.2 cm in diameter.

A  $^{57}\text{Co}$  point source (370 MBq over 500  $\mu\text{m}$  diameter) was used to determine *in situ*  $\text{Fe}^{3+}/\sum\text{Fe}$  for all Multi-Anvil run products. A horizontal section of the MA capsule (1.6 mm in diameter) was selected for the measurements. When possible, samples were polished to achieve an optimum thickness according to the Fe content (mol.%) and relative  $^{57}\text{Fe}$  content (mol%) in each  $(\text{Mg,Fe})\text{O}$  sample (Long, 1983), but in any case sample thicknesses were kept below  $\sim 5$  mg unenriched  $\text{Fe}/\text{cm}^2$  to avoid thickness effects.

Mössbauer spectra were recorded at room temperature (293 K) in transmission mode on a constant acceleration Mössbauer spectrometer. The lines were fitted using a pseudo-Voigt line

## 2. Experimental Methods

form, using the commercially available fitting program NORMOS written by R.A. Brand (distributed by Wissenschaftliche Elektronik, Germany).

Synthetic (Mg,Fe)O spectra consisted in almost all cases of three doublets, two attributed to  $\text{Fe}^{2+}$  and one with very small isomer shift and quadrupole splitting values, attributed to  $\text{Fe}^{3+}$  (McCammon et al., 1998). The range of  $\text{Fe}^{3+}/\Sigma\text{Fe}$  was between 1 and 15 at%.

### 2.4.1 The basic principles

The Mössbauer effect is defined as the recoilless emission and resonant absorption of  $\gamma$ -rays by atomic nuclei in solids. The recoil-free emission  $E_R$  is proportional to the square of the recoil free energy of the  $\gamma$  rays and decreases as a function of the mass  $M$  of the emitting atom, as shown by the following equation:

$$E_R = \frac{E_\gamma^2}{2Mc^2}. \quad (2.1)$$

Recoil-free emission is possible in the case of a solid, as  $M$  tends to infinite values and thus  $E_R$  tends to zero. The recoil free fraction  $f$  - known also as the Debye-Waller factor or Lamb-Mössbauer factor - is defined as the portion of  $\gamma$  rays emitted without loss of energy of the quantum. The recoil-free fraction in Mössbauer spectroscopy increases with decreasing recoil energy, decreasing temperature and increasing Debye temperature  $\Theta_D$ . Stronger absorption is observed at lower temperatures, and materials with stronger bonding show stronger absorption.

The Coulomb interactions between the nucleus and the atomic electrons depend strongly on the electronic and crystallographic configuration, chemical and magnetic state of the atom. The so-called hyperfine parameters that we can extract from a Mössbauer spectrum provide information regarding these hyperfine interactions.

The interaction between the positive charged nucleus of finite size and the negative electronic charge is defined as the electronic monopole interaction, which causes a shift in the energies of the nuclear levels. Electrons belonging to the s-orbitals are involved in this type of interaction, since they have the ability to penetrate the nucleus, whereas electrons with non-zero angular momentum (p-, d-, f-electrons) do not.

## 2. Experimental Methods

The shift is known as isomer shift  $\delta_0$  ( $IS_0$ , alternatively called the chemical shift, Fig. 2.3a), and it is affected by the difference in the averaged nuclear radii of the ground (g) and isomeric excited (e) states. The nuclear transition energy between the source and the absorber are not the same, due to their different electronic and crystallographic configurations.

For the difference in the electrostatic shift between the source and the absorber, the following expression of the isomer shift is obtained:

$$\delta = \frac{2}{3} \pi Z e^2 |\varphi(0)|_A^2 |\varphi(0)|_S^2 \left[ \langle r^2 \rangle_e - \langle r^2 \rangle_g \right], \quad (2.2)$$

where  $Ze$  is the nuclear charge,  $|\varphi(0)|_A^2$  and  $|\varphi(0)|_S^2$  are the s-electron density at the absorber nuclei and at the source nuclei, respectively, and  $r$  is the radii of the nuclei in the excited state and ground state. The temperature dependence of the isomer shift is due primarily to the so-called second-order-Doppler shift  $\delta_{SOD}$ . Thus, the total isomer shift  $\delta$  is determined by the addition of the latter term to the isomer shift  $\delta_0$  caused by the electric monopole interaction:

$$\delta = \delta_0 + \delta_{SOD}. \quad (2.3)$$

The total isomer shift corresponds to the distance between the centroid of the doublets and the zero point of the velocity scale (mm/s) determined by the  $\alpha$ -iron foil calibration (Fig. 2.3b).

The second-order-Doppler shift  $\delta_{SOD}$  depends on the force constant  $K$  and the mean square displacement  $\langle x^2 \rangle$  of the emitting or absorbing nucleus with mass  $M$  according to the formula:

$$\delta_{SOD} = -\frac{K}{2Mc^2} \langle x^2 \rangle. \quad (2.4)$$

As the mean square displacement increases with temperature,  $|\delta_{SOD}|$  also increases.

The quadrupole interaction between the nuclear quadrupole moment and the electric field gradient (EFG) at the nucleus due to the surrounding electrons takes the name of quadrupole splitting ( $\Delta E_Q$ ), and causes a lifting of the degeneracy of the nuclear energy states (Fig.2.3b). The excited state splits into two levels, which translates into a doublet with equal component linewidths and areas for the ideal random absorber case (Fig. 2.3c). The quadrupole splitting measures the difference in energy between the excited states and it can be expressed as follows:

## 2. Experimental Methods

$$\Delta E_Q = \frac{1}{2} e Q V_{ZZ} \sqrt{1 + \frac{\eta^2}{3}}, \quad (2.5)$$

where  $Q$  is the nuclear quadrupole moment,  $e$  is the electron charge,  $V_{ZZ}$  is the principal component of the EFG tensor and  $\eta$  is the asymmetry parameter ( $\eta = \frac{V_{XX} - V_{YY}}{V_{ZZ}}$  and  $0 \leq \eta \leq 1$ ).

The quadrupole splitting, as well as the isomer shift, depends not only on the valence, spin state and coordination of the absorber atoms, but also on the degree of distortion of the crystallographic site. The quadrupole splitting can also provide information regarding the atomic environment (next nearest neighbors). The quadrupole splitting is temperature dependent primarily due to the contribution of the valence electrons, and pressure dependent due to both the valence electrons of the absorbing nucleus and effects from adjoining atoms.

Each site contributes to the Mössbauer spectrum, giving a subspectrum (e.g. quadrupole doublet) whose area is proportional to the relative abundance of that particular site in the absorber. Another important parameter of a Mössbauer subspectrum is the linewidth of the absorption line, as it can provide information about the degree of uniformity of the crystallographic sites occupied by iron. However in addition, the linewidth can be affected by instrumental characteristics (vibrational, geometrical, thermal, and electronic), the source (self-absorption due to decay) and sample (thickness broadening, next-nearest neighbour effects).

## 2. Experimental Methods

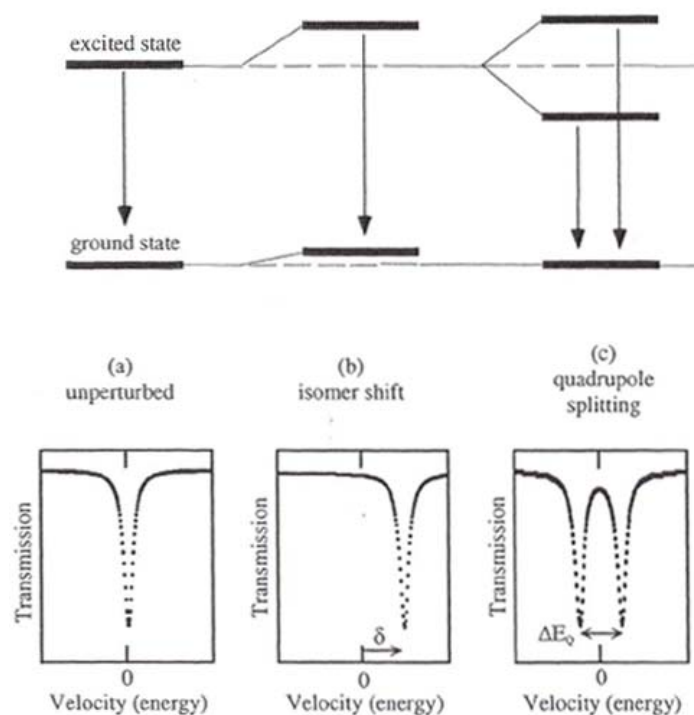


**Fig. 2.3** – Nuclear energy level diagram and resulting Mössbauer spectra illustrating the hyperfine parameters isomer shift and quadrupole splitting (*from McCammon, 2000*).

### 2.4.2 Conventional source and point source

A Mössbauer source consists of a radioactive isotope parent of the chemical species that we are interested to determine the oxidation state for. The  $\gamma$ -rays are produced by nuclear decay of the radioactive parent. In case of iron, the radioactive parent is  $^{57}\text{Co}$ , decaying to the isotope  $^{57}\text{Fe}$ , commonly present in nature with an abundance of about 2.2%, whereas the stable form of iron –  $^{56}\text{Fe}$  – represents an abundance of 91.72%. The half-life of  $^{57}\text{Co}$  is relatively long (270 days) compared to typical Mössbauer data collection times.

The nuclear decay of  $^{57}\text{Co}$  to  $^{57}\text{Fe}$  produces (among other things)  $\gamma$ -rays with energy equal to 14.413 keV, which represents the transition from the first excited state of the  $^{57}\text{Fe}$  nucleus (spin 3/2) to the ground energy state (spin 1/2). The  $\gamma$ -rays produced can then excite ground state  $^{57}\text{Fe}$  nuclei in the absorber to the excited state. The resonant absorption conditions can be maintained by modulating the  $\gamma$ -ray energy through motion of the source relative to the absorber using an electromechanical drive system, causing a Doppler shift of energy of the emitted  $\gamma$  radiation (Fig. 2.4). Whenever the resonant absorption conditions are fulfilled in the absorber, the absorbed  $\gamma$ -rays are re-emitted in all directions and only primarily the non-

## 2. Experimental Methods

absorbed  $\gamma$ -rays will be collected by the detector. In this way the shifts and splitting of the nuclear energy levels can be recorded through the Mössbauer effect. The drive oscillating the source is usually operated at constant acceleration with a symmetric velocity shape. A Mössbauer spectrum is expressed in counts as a function of source velocity (mm/s), and the velocity scale is calibrated using a standard material, generally alpha-iron at room temperature.

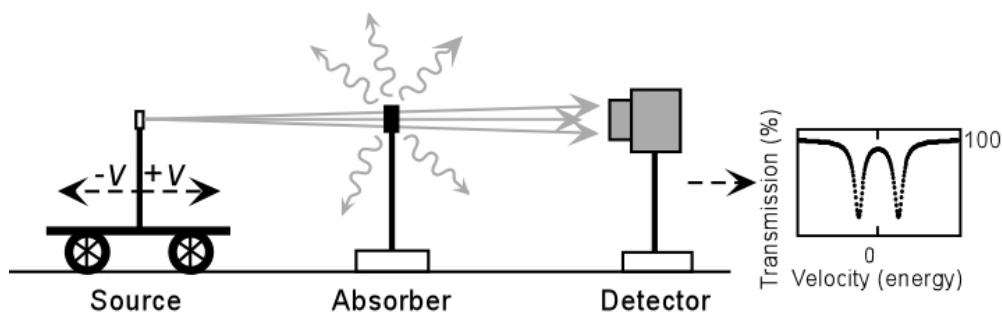


**Fig. 2.4** – Schematic diagram of a Mössbauer spectrometer (from McCammon, 2004, based on a drawing from Gütlich et al., 1978).

Depending of the nature of the investigation, Mössbauer measurements can be performed at room temperature (RT), low temperature (LT, in this case the absorber is cooled by liquid  $N_2$  or He) or high temperature (HT), within a temperature range from near absolute zero to  $1600^\circ\text{C}$ , and measurements can also be made at high pressure using a diamond anvil cell (up to at least 100 GPa) or under the influence of an external magnetic field.

A conventional  $^{57}\text{Co}$  source has a diameter of about 1 cm, which provides a sufficiently high count rate to collect a spectrum. The source diameter can be significantly reduced if the number of parent nuclei per unit area is increased. In this way the diameter of a  $^{57}\text{Co}$  source can be reduced to as low as 500  $\mu\text{m}$ , which is the diameter of a typical so-called “point source”. The disadvantage of a point source is a rapid increase in source thickness with time as a consequence of the  $^{57}\text{Co}$  higher density. This reduces the usable life time of the source.

The quality of the signal is dependent on the absorber density ( $\text{mg Fe}/\text{cm}^2$ ). In the case of a conventional source, the absorber (i.e., the sample) is normally in the form of a fine-grained powder distributed over a sample holder with 1.2 cm in diameter. If a point source is used, the sample diameter limit is roughly 100  $\mu\text{m}$ . In both cases, the sample thickness must be appropriately calculated to allow for effects due to electronic absorption and thickness. Particular care is needed for samples enriched in  $^{57}\text{Fe}$  due to their potentially high  $^{57}\text{Fe}$  concentrations.

## 2.5 Powder X-Ray Diffraction

In a crystalline material, X-rays are diffracted by the atoms distributed in the crystal lattice according to Bragg's law:

$$n\lambda = 2d \sin \theta, \quad (2.6)$$

where the integer number  $n$  is the order of reflection,  $\lambda$  is the wavelength of the radiation,  $d$  is the spacing between the parallel planes involved in the X-ray path, and  $\theta$  is the Bragg angle. The interference of the incident X-ray with a certain angle of incidence and the reflected ray will be constructive when the difference in path is an integer multiple number of wavelengths (Fig. 2.5). Since the X-rays are diffracted with the same angle as the incident beam, Bragg's law is written in terms of reflection of X-rays from the lattice planes. The undiffracted incident beam and the diffracted beam form between them an angle of  $2\theta$ .

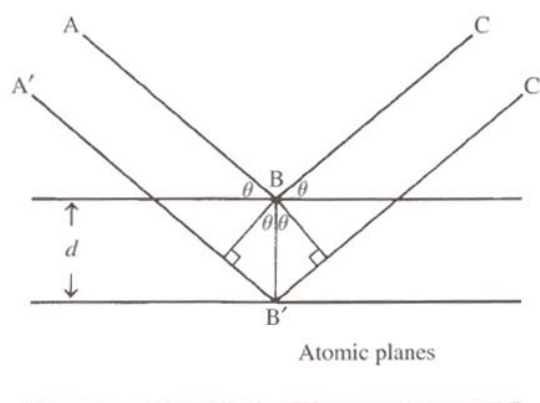


**Fig. 2.5** – Bragg reflection: diffracted rays are in phase when the distance  $A'B'C'$  differs from  $ABC$  by an integral number of wavelengths (*from Reed, 2005*).

The synthesized (Mg,Fe)O powders were characterized before and after gas mixing re-equilibration by means of X-ray powder diffraction. X-ray diffraction patterns were collected on a Siemens D5000 diffractometer at Bayerisches Geoinstitut for all samples to check phase identification and homogeneity. Data collection was carried out at 40 kV and 35 mA, and  $2\theta$  was varied from  $15^\circ$  to  $150^\circ$ . The radiation used was  $\text{CuK}\alpha$  ( $\lambda = 1.542 \text{ \AA}$ ). Phase identification was determined using the software Stoe-WinXPOW (distributed by Stoe & Cie GmbH, 2004).

In some cases, a Philips X'Pert diffractometer with  $\text{CoK}\alpha$  radiation ( $\lambda = 1.78897 \text{ \AA}$ ) was used to perform long scans in order to obtain a more accurate diffraction pattern in order to extract unit cell parameters. Silicon powder was used as an internal standard for the

## 2. Experimental Methods

refinements (the proportion between silicon and the sample was 3:1). Data collection was carried out at 40 kV and 40 mA, and  $2\theta$  was varied between  $20^\circ$  and  $120^\circ$ . When necessary, refinements were done using the General Structure Analysis System (GSAS, Larson and Von Dreele, 1994) program and the windows interface, EXPGUI (Tobi, 2001).

### 2.6 Electron MicroProbe Analysis (EMPA)

Electron microprobe analyses were performed on a Jeol XA-8200 to determine the chemical composition of (Mg,Fe)O (quantitative analysis) and the  $\text{Fe}^{3+}/\sum\text{Fe}$  ratios by studying the X-ray emission spectra (qualitative analysis).

#### *Basic principle*

Electron MicroProbe Analysis (EMPA) is a technique intended to determine the chemical composition on small selected areas of solid materials. The sample surface is subjected to a focused electron beam and, as a consequence, X-rays will be produced.

The commonly used emitter of electrons is a tungsten filament (about 0.1 mm in diameter), which is kept at a negative potential (typically 10-30kV) to accelerate electrons towards the sample. Each microprobe instrument consists of up to 5 spectrometers of type WD (Wavelength-Dispersive), and often has one ED (Energy-Dispersive) spectrometer. WD and ED spectrometers are complementary.

The WD spectrometers make use of Bragg reflection by a crystal (eq. 2.6), and they operate by measuring one particular wavelength at a time. Thus, several crystals are needed to cover the required range of wavelengths. Each element analyzed in the sample corresponds to a line at a given wavelength in the X-ray spectrum collected. A qualitative analysis is straightforward to perform simply by identifying elements by their wavelengths. A quantitative analysis involves comparing the wavelength observed for the elements present with those emitted by standard materials (either pure elements or compounds with known composition). Electron microprobe analysis achieves high accuracy (approaching  $\pm 1\%$ ) and detection limits can extend as low as tens of parts per million (by weight). Under normal conditions, spatial resolution is limited to about 1  $\mu\text{m}$  by the spreading beam within the sample. This represents a large advantage of the electron microprobe compared to Mössbauer spectroscopy.

## 2. Experimental Methods

### *X-ray emission spectra and electronic transitions*

X-rays are produced by two distinct mechanisms as a consequence of bombarding a solid by an electron beam: electrons interact with atomic nuclei, producing a smooth “continuous” spectrum, while a “characteristic” spectrum is produced as a result of electron transitions between energy levels specific to each element (Fig. 2.6). In the first mechanism, the passage of an electron through the electronic field close to the atomic nucleus causes the electron to make a quantum jump to a lower energy state, accompanied by emission of an X-ray photon with associated energy  $E_0$  (initial energy of the electron).

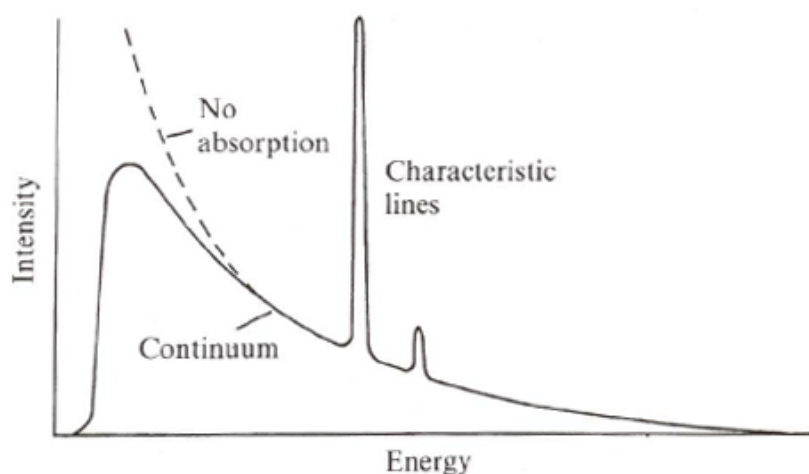


**Fig. 2.6** – X-ray spectrum as a function of photon energy, showing characteristic lines superimposed on the continuous X-ray spectrum (or “continuum”) produced by incident electrons involved in inelastic collisions with atomic nuclei (from Reed, 2005).

The intensity  $I$ , associated with a continuum spectrum, can be represented by the following relation (Kramer’s law):

$$I = \frac{c \times Z(E_0 - E)}{E}, \quad (2.7)$$

where  $c$  is a constant,  $E$  is the energy associated with the X-ray photon [ $E = \frac{12.398}{\lambda}$ , where  $E$  is expressed in keV and  $\lambda$  in ångström units (Å)] and  $Z$  refers to the atomic number (or mean atomic number in the case of a compound). The detectability of the characteristic lines of elements present in low concentration is limited for the continuous X-ray spectrum.

## 2. Experimental Methods

Characteristic X-rays are produced by electron transitions between bound electron orbits, whose energies are governed mainly by the principal quantum number  $n$ . Therefore, the X-ray photon energy corresponds to the difference in energies between the initial and final levels involved in the transition. In an atom it is possible to define closed shells within the inner orbits as a function of distance from the nucleus and decreasing energy. Those shells are named K ( $n = 1$ ), L ( $n = 2$ ), M ( $n = 3$ ) etc. These shells are normally completely filled by electrons.

The number of electrons occupying these shells varies based on quantum numbers relating to the angular momentum, so that the K shell can contain a maximum of 2 electrons, the L shell 8, the M shell 18, and so on. Each shell is additionally split into sub-shells, each corresponding to a different quantum configuration. In the case of the L shell, which is the one involved in the flank method measurements, three sub-shells are present (L1, L2 and L3).

Whenever an electron occupying one of the inner shells is removed, the atom is ionized and a characteristic X-ray photon is produced. In order to produce a characteristic X-ray line,  $E_0$  (incident electron energy) must exceed the “critical excitation energy” ( $E_c$ ) necessary to ionize the relevant shell of the element concerned.

The lines designated for each shell are ordered by intensity and indicated with Greek letters, so that  $\alpha$  refers to the most intense line,  $\beta$  to the next most intense line, and so on. In each group the lines can be additionally subdivided and numbered in order of intensity (e.g.  $L\alpha_1$  for the first order). The energy of a given line varies according to Moseley’s law as the square of the atomic number of the emitting element.

## 2. Experimental Methods

### *X-rays: Intensity and absorption effects*

When electrons hit solid materials (e.g. the sample intended to be analyzed), part of the characteristic X-rays can be absorbed by the sample itself, in proportions depending on the sample composition. As a consequence, the observed intensity of the characteristic X-ray lines may be significantly affected. Thus, the intensity can be estimated with the following expression:

$$I = I_0 \exp(-\mu\rho x), \quad (2.8)$$

where  $I_0$  is the initial intensity,  $I$  is the intensity corrected for the absorption,  $\mu$  is the “mass absorption coefficient” ( $\text{cm}^2\text{g}^{-1}$ ),  $\rho$  is the density ( $\text{g cm}^{-3}$ ) and  $x$  is the path length (cm). The mass absorption coefficient  $\mu$  ranges from less than 100 for X-rays of high energy for absorbers of low atomic number, to more than 10000 for X-rays of low energy for absorbers of high atomic number. In the latter case, strong absorption can occur already for values of  $x$  less than 1  $\mu\text{m}$  in thickness.

The absorption depends on the factor  $\chi$ , which is defined as  $\mu \text{ cosec } \psi$ , where  $\psi$  is the X-ray take-off angle (Fig. 2.7). If we consider the X-rays produced at a certain depth  $z$  within the sample, the X-ray intensity will be reduced by absorption of a factor equal to  $\exp(-\chi\rho z)$ , where  $\rho$  is the density of the specimen. The correction methods commonly used to correct the measurement concentrations for absorption are ZAF (atomic number, absorption, fluorescence) and phi-rho-z. Both methods take into account self-absorption and matrix effects. The peak intensity measured is also partially affected by the background contribution (mainly originating from the X-ray continuum), even though it is only a weak function of wavelength.

## 2. Experimental Methods

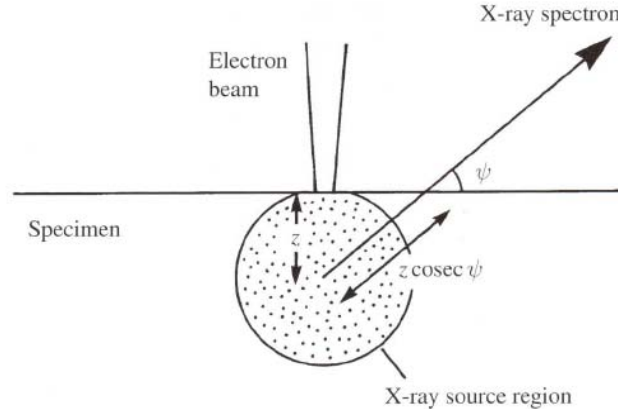


**Fig. 2.7** – X-rays produced at depth  $z$  within the specimen, emerging with travel distance  $z \operatorname{cosec} \psi$ .  $\psi$  is the take-off angle (from Reed, 2005).

### *Heat production*

One of the main problems associated with the incident electron beam is the heat which is produced by the small fraction of its energy that usually is converted into X-rays and light. The increase in temperature is proportional to the incident electron energy ( $E_0$ , expressed in keV) and to the current in use ( $i$ ,  $\mu\text{A}$ ) according to the following expression:

$$\Delta T = \frac{4.8E_0 i}{kd}; \quad (2.9)$$

however temperature decreases with thermal conductivity  $k$  ( $\text{W cm}^{-1} \text{K}^{-1}$ ) and beam diameter  $d$  ( $\mu\text{m}$ ). In the case of metals, the thermal conductivity ranges between 1 and 4, and normally the heat produced is negligible. Nevertheless, in the case of mineral phases showing a low thermal conductivity, the heat produced cannot be neglected.

### *Wavelength Dispersive Spectrometers*

By using Wavelength Dispersive (WD) spectrometers, X-rays are dispersed according to their wavelength by means of Bragg reflection. High spectral resolution can be achieved, but for a given beam current, intensities appear to be lower than the ones achieved for the ED spectrometer. Normally the most intense reflections involved in the use of a WD spectrometer

## 2. Experimental Methods

are of the first order ( $n = 1$ , see eq. 2.6). Orders higher than 1 produce extra peaks in the spectrum, and therefore they are more difficult to treat.

As Bragg's law limits for each wavelength only a certain value of  $2d$ , several crystals are necessary to cover the entire range of wavelengths of interest. Table 2.1 reports the crystals most commonly used in WD spectrometers with their related  $2d$  values. The wavelength coverage is shown in Figure 2.8.

**Table 2.1:**  $2d$  values for the different kind of crystals used in WD spectrometers

WD Crystal type	$2d$ (Å)
LIF	4.026
PET	8.742
TAP	25.9

Crystals are curved in order to obtain a large reflecting area, and crystals and source are designed to be located on an imaginary Rowland circle where the geometry is in such a way that the Bragg angle would remain the same at all points.

Narrow slits can be placed in front of the counter in cases where higher resolution is needed. As a result, peaks will become sharper. It is not ideal to use narrow slits for quantitative analysis, since the higher resolution of the peak is also associated with a larger error relative to the Bragg angle.

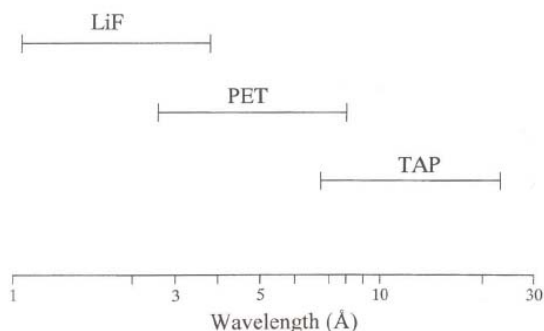


**Fig. 2.8** – Wavelength coverage of crystals used in WD spectrometers (*from Reed, 2005*).

## 2.6.1 Major element analysis plus qualitative analysis

*Flank method procedure: spectrometer calibration*

In order to apply the flank method for  $\text{Fe}^{3+}/\Sigma\text{Fe}$  measurements using the electron microprobe, there are several adjustments that are necessary to be made on the qualitative analysis setup. The  $L\beta$  and  $L\alpha$  measurement positions have to be determined once for the microprobe in use. The determination of these two energy positions is done by collecting the FeL X-ray emission spectra for one  $\text{Fe}^{2+}$ -bearing phase (almandine) and one  $\text{Fe}^{3+}$ -bearing phase (andradite). For andradite the peak maxima are shifted to higher energies if compared to almandine (Fig. 2.9) and the intensity ratios would also be higher. As already discussed in the introduction, measuring  $L\beta/L\alpha$  ratios on the flank positions (corresponding to the minima and maxima of the difference of the two spectra almandine-andradite) offers the best accuracy for the determination of  $\text{Fe}^{3+}/\Sigma\text{Fe}$ .

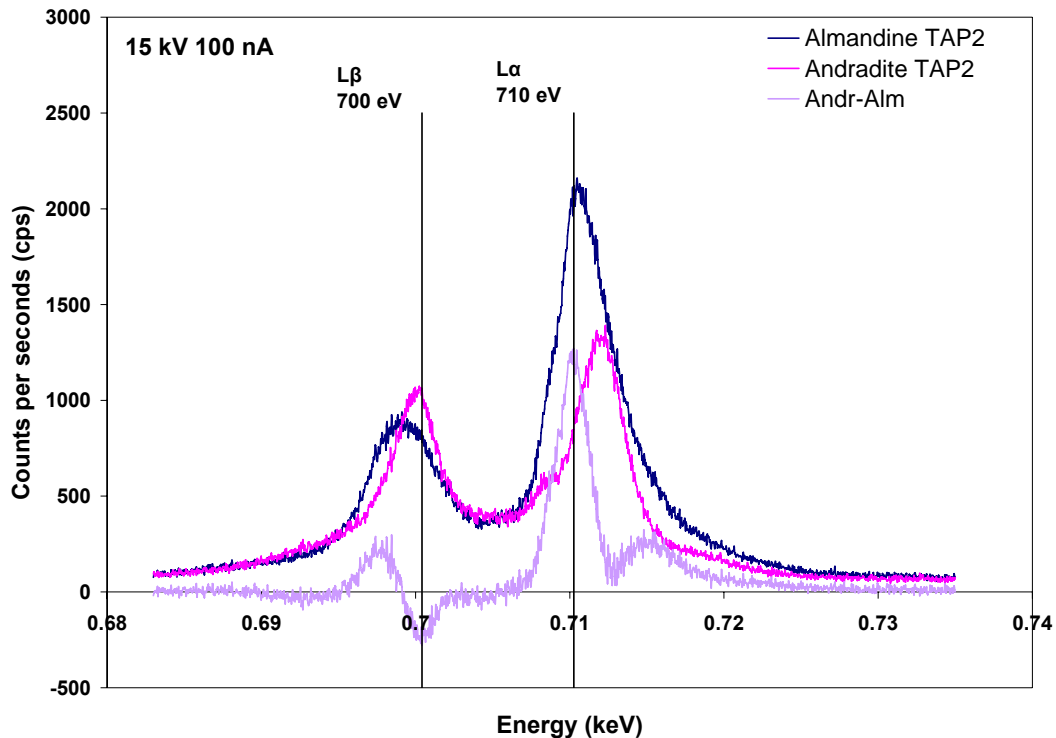


**Fig. 2.9** – FeL X-ray emission spectra of pyrope-rich almandine and andradite showing also the difference spectrum. Spectra were collected at 15kV and 80 nA. The flank method measurement positions are defined as the regions of largest difference between the two spectra.

## 2. Experimental Methods

It was shown that the voltage affects the peak intensities (Höfer and Brey, 2007); therefore the almandine-andradite spectra were collected at conditions of 15 kV and 100 nA (for a better resolution of the spectra). Because the  $L_3$  absorption line overlaps with the  $FeL\alpha$  measuring position and moves across this position as a function of  $Fe^{3+}$  content, the determination of intensities at this position enhance the effect of the valence-dependent variation on the absorption edge.

The spectra were collected on both the TAP spectrometers available (TAP2 and TAP3) to test their accuracy. Results are slightly different: TAP2 showed higher resolution of the spectra, and therefore was chosen for the flank method measurements. For this spectrometer, the detector slits are set to be the smallest possible, in order to obtain higher resolution during measurements.

In order to quantify the daily spectrometer shift, the  $FeK\alpha_1$  (9<sup>th</sup> order) needs to be defined on Fe metal using one of the TAP spectrometers for better resolution (quick peak search on Fe metal, starting with the known position for the  $FeK\alpha_1$  9<sup>th</sup> order line; Integral mode; optimize SCA (PHA)). To offer the best resolution possible, the detector slits are reduced to the smallest aperture possible for the spectrometer involved in the flank method procedure (300  $\mu$ m). Once the correct position of the  $FeK\alpha_1$  9<sup>th</sup> line is known, the software PeakFitH (kindly provided by Heidi Höfer, University of Frankfurt) runs to calculate the daily shift, which enables a correction of the two flank method  $L\alpha$  and  $L\beta$  measuring positions. The program runs 3 repetitions of measurements on 6 spectrometer positions, calculated on the basis of the input position ( $FeK\alpha_1$  9<sup>th</sup> order after quick peak search). These calculated positions are the symmetrical distances of fe1 and fe2 around the peak maximum (see Fig. 3 in Höfer et al. 2000). The counting time is 100 s for each position. The entire procedure, including the quick peak search on Fe metal, must be performed at 25kV and 80nA in order to increase counting statistics.

After running the PeakFit program, the results are transferred (number of counts, intensities and beam current values) into an Excel spreadsheet in order to calculate the beam current-normalized ratios fe1/fe2 (according to Höfer et al. 2000). In order to calculate the corresponding regression line and the spectrometer shift for fe1/fe2 = 1 for the current measuring day, the 3 values for fe1/fe2 are plotted versus the spectrometer position (fe1/fe2 = 1 if the peak is symmetrical in this region).

## 2. Experimental Methods

### *Flank Method measurements*

Flank method measurements are performed at 15kV and 80 nA. In order to perform major element analysis plus flank method measurements, two dummy elements for the flank method have to be added to the element list needed for the major elements analysis. Normally, As is chosen for FeL $\alpha$  and Br for FeL $\beta$ . The TAP dummy peak positions corrected for the daily shift are added at this stage as measurement conditions for the two dummy elements. The measuring time is proportional to bulk Fe (wt%), and in the case of ferroperricite, the measuring time was 180 s each. The background is set to be as small as possible. A narrow energy window is set to avoid overlaps with higher-order X-ray emission lines, and optimized SCA (PHA) conditions for FeL $\alpha$  on Fe metal. At this stage, measuring conditions are in differential mode. To avoid contamination artifacts, L $\beta$  is measured before L $\alpha$  on the same spectrometer. Before starting the measurements of unknown samples, it is necessary to measure a sample of known composition and L $\beta$ /L $\alpha$  ratio in order to monitor the accuracy of the measurements. It can then be used as a standard once the measurements start on unknown samples to monitor any possible drifts of the spectrometer which may cause a shift in L $\beta$ /L $\alpha$  ratio.

The L $\beta$ /L $\alpha$  ratio is determined as the ratio between the net intensities only relative to the two dummy elements Br and As. Therefore, flank method measurements are defined as counts per second (cps). Once the ratios are determined, it is possible to correlate them to the iron oxidation state.

### *Major element analysis combined with flank method measurements*

The flank method procedure was initially tested on garnets on the microprobe at Bayerisches Geoinstitut to check the reproducibility of the method as calibrated by Höfer and Brey (2007). According to the procedure described, major element analysis plus qualitative analysis was performed simultaneously at an acceleration voltage of 15 kV and a current of 80 nA. Routine major element analysis is usually performed at the conditions 15 kV and 20nA; however a higher current (80 nA instead of 20nA) enables the collection of more counts during the flank method measurements. The X-ray emission counts were measured for the two positions L $\alpha$  and L $\beta$  for 180 seconds each, for a total time of 360 seconds at each

## 2. Experimental Methods

measured spot. When possible, measurements were performed along line profiles with an average of minimum 20-30 spots for each sample at each microprobe session.

In order to perform major element analysis for natural garnets, up to nine elements were calibrated using the five spectrometers available. The elements calibrated for the measurements were Si, Al, Mg, Ca, Cr, Fe, Na, Mn, and Ti, with counting times of 20/10s. The point beam was focused and set to the smallest diameter possible (1 $\mu$ m). Fe was calibrated using an almandine standard, the McGuire almandine (McGuire et al. 1992), kindly provided by Heidi Höfer, which was used for the first calibration of the Flank Method for garnet (Höfer and Brey, 2007). The oxygen concentration was calculated from the oxides and not directly measured. Detector slits for the spectrometer TAP were chosen to have the smallest aperture possible (which corresponds to 300  $\mu$ m for a TAP spectrometer) in order to reduce as much as possible the background contribution during flank method measurements.

All synthetic (Mg,Fe)O samples previously analyzed by Mössbauer spectroscopy were mounted on epoxy or glass for the Electron Microprobe measurements. Sample homogeneity was tested during microprobe analysis, and any evidence for diffusion processes during synthesis using the Multi-Anvil apparatus were excluded from the gradient from the inner to the outer region of each sample. For major element analysis on synthetic (Mg,Fe)O, initially only Fe and Mg were calibrated. For the analysis of natural (Mg,Fe)O, up to eight elements have been additionally calibrated: Si, Al, Mg, Ca, Cr, Fe, Na, Mn. Only one spectrometer type (TAP) was used to perform flank method measurements, and the correction used for self-absorption and matrix effect was the type *phi-rho-z*.

### 3. Results (1): Flank Method Calibration

#### 3.1 Flank Method Results: Determination of the L $\beta$ and L $\alpha$ flank method measuring positions

The FeL $\beta$  and FeL $\alpha$  positions were determined for the Jeol XA-8200 at Bayerisches Geoinstitut and are reported in Table 3.1 with the correspondent energy positions. For comparison, FeO-Fe<sub>2</sub>O<sub>3</sub> spectra were also collected to verify that the determination of FeL $\beta$  and FeL $\alpha$  is reproducible using any Fe<sup>2+</sup>- and Fe<sup>3+</sup>-bearing phases other than almandine (Fe<sub>3</sub>Al<sub>2</sub>(SiO<sub>4</sub>)<sub>3</sub>) and andradite (Ca<sub>3</sub>Fe<sub>2</sub>(SiO<sub>4</sub>)<sub>3</sub>). As a result, L $\beta$  and L $\alpha$  values determined using the two different couple of Fe<sup>2+</sup>- and Fe<sup>3+</sup>-bearing phases are comparable.

**Table 3.1** - Flank method positions L $\alpha$  and L $\beta$  for the microprobe Jeol JXA-8200 at BGI

	Almandine-Andradite		FeO-Fe <sub>2</sub> O <sub>3</sub>	
	FeL $\alpha$	FeL $\beta$	FeL $\alpha$	FeL $\beta$
<b>Energy (eV)</b>	710	700	711	700
<b>mm*</b>	190.74	188.09	190.82	187.98

\*\* distance between the position of the Fe L $\alpha$  and Fe L $\beta$  on the spectrometer crystal and the beam spot in the Rowland circle geometry

Following the flank method procedure established by Höfer and Brey (2007) and illustrated in § 2.6.1, the corrections for the spectrometer shift that daily occurs at the electron microprobe have been calculated and applied to correct the two flank method measuring positions. Table 3.2 reports examples of repeated microprobe sessions and the relative spectrometer shift calculated to show its sensitivity to the drift. The Fe K $\alpha$  9<sup>th</sup> order position (given in millimeters and corresponding to the distance between the position of the Fe K $\alpha$  9<sup>th</sup> on the spectrometer crystal and the beam spot in the Rowland circle geometry) is reported in Figure 3.1 for all microprobe sessions (indicated in days), showing a non linear variation. Therefore, if L $\beta$  and L $\alpha$  are not corrected for the shift, it might affect the accuracy of flank method measurements over time. Spectrometer drifts are also monitored during microprobe measurements by analyzing one of the standard samples at the start and finish of each

### 3. Results (1): Flank Method Calibration

session and measurements on the standard are repeated after a certain number of measurements of unknown samples.

**Table 3.2** - FeL $\alpha$  and FeL $\beta$  positions corrected after the spectrometer shift measurements for each microprobe session (indicated by date)

<b>Day</b>	<b>Starting FeK<math>\alpha_1</math>, 9<sup>th</sup> order (mm)</b>	<b>Shift* measured each working day</b>	<b>FeL<math>\alpha</math> (shift corrected)</b>	<b>FeL<math>\beta</math> (shift corrected)</b>
18.01.07	189.372	0.045	190.727	188.057
15.02.07	189.366	0.051	190.688	188.038
21.02.07	189.375	0.042	190.698	188.048
13.03.07	189.397	0.02	190.717	188.067
30.03.07	189.395	0.022	190.712	189.062
17.04.07	189.384	0.033	190.706	188.056
18.06.07	189.393	0.024	190.716	188.066
19.07.07	189.393	0.024	190.716	188.066
15.10.07	189.352	0.065	190.676	188.026
23.10.07	189.361	0.056	190.682	188.032
06.11.07	189.351	0.066	190.672	188.022
19.11.07	189.345	0.072	190.665	188.015
07.01.08	189.349	0.068	190.681	188.031
14.01.08	189.359	0.058	190.679	188.029
14.02.08	189.359	0.058	190.680	188.030
06.03.08	189.362	0.055	190.684	188.034
10.03.08	189.347	0.07	190.671	188.021
15.04.08	189.435	-0.018	190.760	188.110
23.04.08	189.435	-0.018	190.754	188.104
28.04.08	189.432	-0.015	190.751	188.101
30.04.08	189.453	-0.036	190.774	188.124
17.07.08	189.458	-0.041	190.776	188.126
24.08.08	189.453	-0.036	190.771	188.121
04.09.08	189.463	-0.046	190.787	188.137

### 3. Results (1): Flank Method Calibration

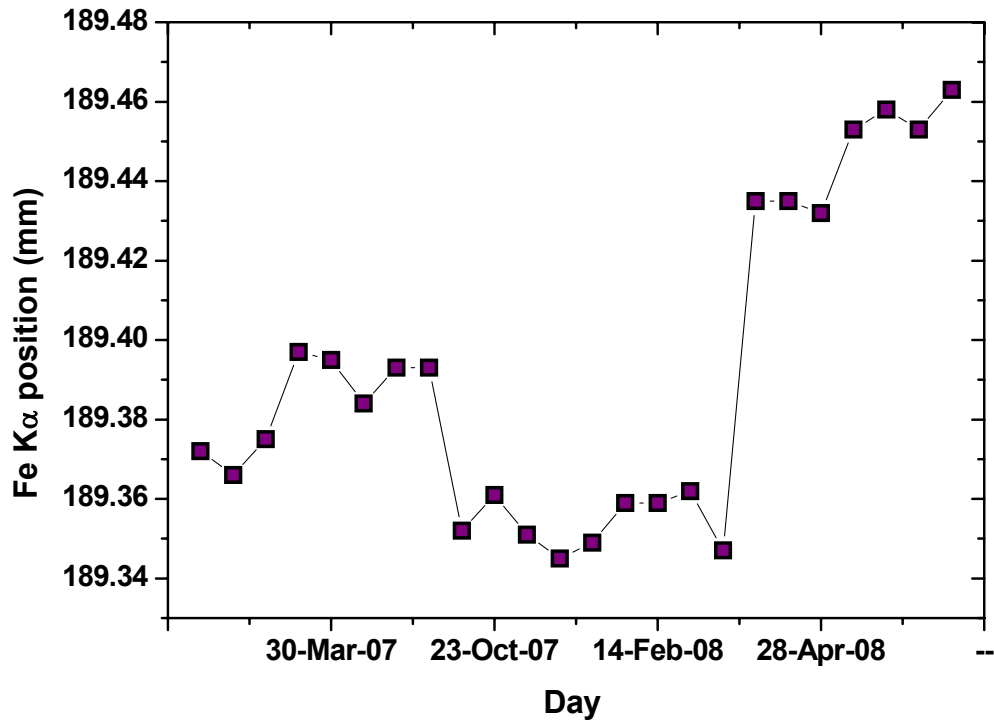


**Fig. 3.1** – Spectrometer drift expressed as the K $\alpha$  9<sup>th</sup> order position (in mm) as a function of microprobe session (indicated by date).

### 3.2 Flank Method calibration for natural garnets on the Jeol JXA-8200 @

#### BGI

Ten natural microxenolithic garnets (UA standard set) recovered from the Central Slave Craton (Diavik diamond mine, Canada) were kindly provided by Thomas Stachel (University of Alberta, Canada) for Flank Method measurements. Samples were investigated by electron microprobe for both quantitative analysis and qualitative analysis with the aim to reproduce the calibration for garnets on the microprobe Jeol JXA-8200 at Bayerisches Geoinstitut. For this purpose, a standard set of garnets used for the garnet calibration were kindly provided by Heidi Höfer and included in the electron microprobe measurements.

Fe bulk composition for the UA set ranges between 4.81 and 6.50 wt%. The  $\text{Fe}^{3+}/\Sigma\text{Fe}$  ratio was previously determined by Catherine McCammon at Bayerisches Geoinstitut using Mössbauer spectroscopy showing a variability from 3.7 to 13.0%. Flank method measurements were carried out according to the procedure described in § 2.6.1. Major element analysis for the UA standard set are reported in Table 3.3a, whereas major element analysis for the set of standards used for the garnet calibration established by Hofer and Brey (2007) are reported in Table 3.3b.

Table 3.4 summarizes bulk Fe composition (wt%), flank method measurements  $L\beta$  and  $L\alpha$  and the  $\text{Fe}^{3+}/\Sigma\text{Fe}$  ratios for all garnets. The  $\text{Fe}^{3+}/\Sigma\text{Fe}$  ratios for the set of 7 standards used for the garnet calibration (McGuire, Damkoll, KerGB, Mir23, Mir13, Mir2) are taken from Höfer and Brey (2007) and references therein, whereas  $\text{Fe}^{3+}/\Sigma\text{Fe}$  referred to Mir1 garnet standard was previously determined using Mössbauer spectroscopy by Catherine McCammon at Bayerisches Geoinstitut.

$L\beta/L\alpha$  ratios show a linear positive correlation as a function of  $\Sigma\text{Fe}$  and  $\text{Fe}^{2+}$  (wt%) (Fig. 3.2 and Fig. 3.3), which is in good agreement with previous studies by Höfer and Brey (2007). Error bars for  $L\beta/L\alpha$  ratio correspond to the 1  $\sigma$  uncertainty of the mean value from 20-30 independent measurements at 15 kV and 80 nA and a minimum diameter, whereas error bars for  $\text{Fe}^{2+}$  correspond to the propagation of the Mössbauer uncertainty and the uncertainty obtained from the  $\Sigma\text{Fe}$  mean values from 20-30 independent measurements at 15 kV and 80 nA and a minimum diameter. As can be observed in Figure 3.2, the two sets of garnets do not show the same slope as a function of the bulk Fe composition.

### 3. Results (1): Flank Method Calibration

**Table 3.3a** – Major element analysis for the garnets UA set. Oxides are expressed in weight percent.

Oxides	UA1	UA4	UA5	UA7	UA10	UA13	UA17	UA19	UA22	UA28	UA13 test*
SiO <sub>2</sub>	41.600	41.489	41.053	41.201	41.223	41.018	40.846	40.571	40.138	40.697	40.881
TiO <sub>2</sub>	0.0349	0.0489	0.781	0.285	0.084	0.122	0.019	0.208	0.849	0.047	0.138
Al <sub>2</sub> O <sub>3</sub>	20.986	19.606	19.359	19.572	20.253	18.607	19.122	17.801	16.716	18.218	18.484
Cr <sub>2</sub> O <sub>3</sub>	4.819	7.305	4.923	6.438	5.768	8.193	7.949	9.078	9.439	8.903	8.287
FeO	6.217	6.599	8.234	6.520	7.809	6.116	7.912	7.149	6.837	7.629	6.102
MnO	0.439	0.512	0.464	0.482	0.594	0.494	0.705	0.5835	0.574	0.750	0.478
MgO	20.206	20.838	18.542	18.952	18.337	18.759	18.445	18.100	16.802	18.365	18.806
CaO	3.716	2.279	5.119	5.153	4.895	5.552	4.261	5.515	7.620	4.667	5.518
Na <sub>2</sub> O	0.015	0.027	0.054	0.033	0.026	0.018	0.013	0.034	0.0757	0.024	0.02
K <sub>2</sub> O	0.002	0.003	0.003	0.002	0.001	0	0.002	0.002	0.001	0.001	0
Tot	98.033	98.706	98.530	98.637	98.991	98.879	99.275	99.043	99.051	99.300	98.714

\*sample UA13 was used as a standard to test for the spectrometer drifting. Measurements on UA13 were repeated after having measured all the other samples.

**Table 3.3b** – Major element analysis performed in the present study for the Standard garnet set. Oxides are expressed in weight percent.

Oxides (wt%)	McGuire	Damkoll	KerGB	Mir23	Mir13	Mir2	Mir1
SiO <sub>2</sub>	38.551	38.925	40.941	40.806	40.151	40.439	40.544
TiO <sub>2</sub>	0.091	0.4078	0.426	0.493	0.500	0.397	0.429
Al <sub>2</sub> O <sub>3</sub>	22.613	22.443	23.594	23.511	23.180	23.287	23.344
Cr <sub>2</sub> O <sub>3</sub>	0.032	0.016	0.125	0.0283	0.009	0.012	0.019
FeO	26.386	19.921	10.345	10.731	13.970	13.334	11.728
MnO	3.861	0.851	0.477	0.495	0.561	0.551	0.523
MgO	8.344	9.679	17.010	16.689	14.294	14.870	16.099
CaO	1.725	7.314	5.143	5.365	5.987	5.762	5.45
Na <sub>2</sub> O	0.009	0.0438	0.019	0.016	0.026	0.021	0.022
K <sub>2</sub> O	0.001	0.001	0.002	0.002	0.001	0.003	0.003
Tot	101.614	99.601	98.081	98.137	98.680	98.675	98.162

### 3. Results (1): Flank Method Calibration

**Table 3.4** –  $\Sigma\text{Fe}$  (wt%), flank method measurement results and  $\text{Fe}^{3+}/\Sigma\text{Fe}$  for the UA garnet set and the garnet standards.  $\text{Fe}^{3+}/\Sigma\text{Fe}$  data from Mössbauer measurements.

<b>Sample</b>	<b><math>\Sigma\text{Fe}</math> (wt%)</b>	<b><math>L\beta/L\alpha</math></b>	<b><math>\text{Fe}^{3+}/\Sigma\text{Fe}</math></b>	<b><math>\text{Fe}^{2+}</math> (wt%) Mössbauer</b>
<b>UA1</b>	4.93(4)	0.77(2)	0.04(1)	4.73(4)
<b>UA4</b>	5.20(2)	0.77(2)	0.05(1)	4.94(2)
<b>UA5</b>	6.50(3)	0.78(1)	0.13(2)	5.68(3)
<b>UA7</b>	5.14(2)	0.77(2)	0.05(1)	4.86(2)
<b>UA10</b>	6.13(4)	0.79(2)	0.07(2)	5.72(4)
<b>UA13</b>	4.81(3)	0.76(2)	0.09(2)	4.39(2)
<b>UA17</b>	6.20(2)	0.80(2)	0.04(1)	5.94(2)
<b>UA19</b>	5.61(2)	0.77(2)	0.08(1)	5.19(2)
<b>UA22</b>	5.37(3)	0.77(2)	0.08(2)	4.91(3)
<b>UA28</b>	5.97(3)	0.79(2)	0.04(1)	5.75(3)
<b>UA13 test</b>	4.81(5)	0.76(2)	0.09(2)	4.39(5)
<b>McGuire*</b>	20.19(7)	1.21(2)	0.04(1)	19.38(7)
<b>Damknohle*</b>	15.55(5)	1.05(2)	0.05(1)	14.75(5)
<b>KerGB*</b>	8.20(4)	0.85(1)	0.05(1)	7.81(4)
<b>Mir13*</b>	11.00(4)	0.92(1)	0.05(1)	10.45(4)
<b>Mir23*</b>	8.50(3)	0.86(3)	0.05(1)	8.05(3)
<b>Mir2*</b>	10.50(5)	0.91(1)	0.05(1)	9.97(5)
<b>Mir1</b>	9.29(4)	0.87(2)	0.05(2)	8.83(4)

\*Standards for  $\text{Fe}^{2+}/\text{Fe}^{3+}$  kindly supplied by Heidi Höfer;  $\text{Fe}^{3+}/\Sigma\text{Fe}$  data from Höfer and Brey (2007) and references therein.

3. Results (1): Flank Method Calibration

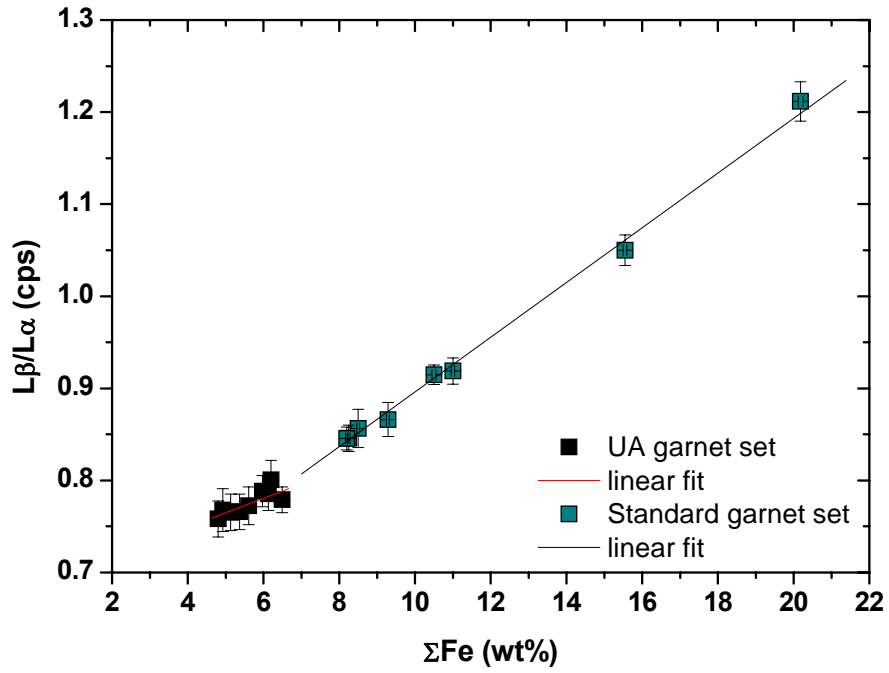


Fig. 3.2 -  $L\beta/L\alpha$  variation as a function of  $\Sigma\text{Fe}$  (wt%) for natural garnets.

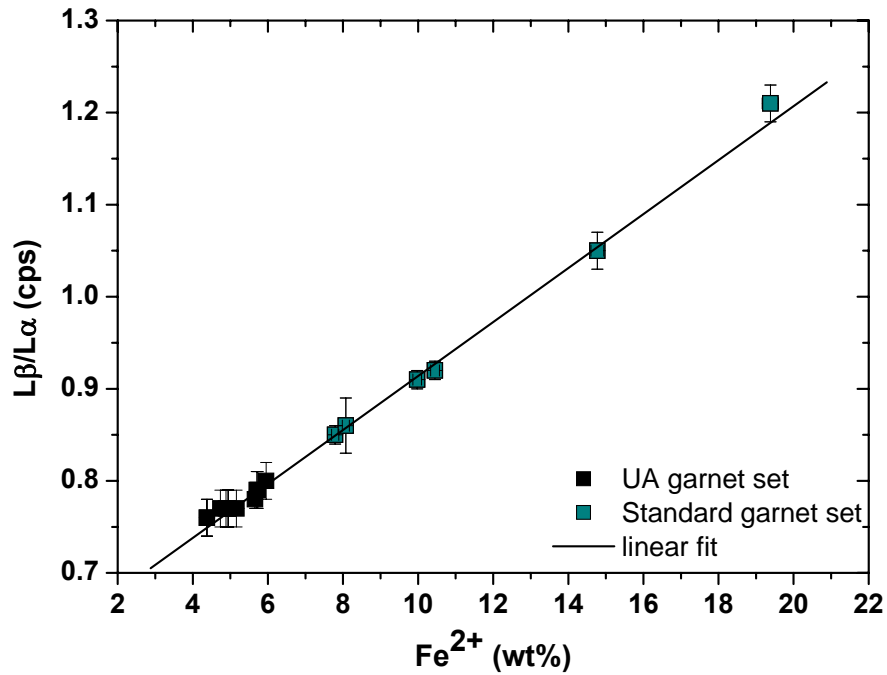


Fig. 3.3 –  $L\beta/L\alpha$  variation as a function of  $\text{Fe}^{2+}$  (wt%) for natural garnets calculated from Mössbauer data.

### 3. Results (1): Flank Method Calibration

In order to test the flank method calibration procedure and to be able to reproduce the calibration curve suggested by Höfer and Brey (2007) on the electron microprobe at Bayerisches Geoinstitut,  $\text{Fe}^{2+}$  contents (wt.%) were calculated for all measured garnets using the equation reported as follows:

$$\text{Fe}^{2+} = -10.11(17) + 18.02(19) * \text{L}\beta/\text{L}\alpha + 0.015(8) * \sum\text{Fe} + 0.159(7) * \sum\text{Fe} * \text{L}\beta/\text{L}\alpha. R^2=0.994 \quad (1)$$

$\text{Fe}^{3+}/\sum\text{Fe}$  ratios were then calculated as the difference between  $\sum\text{Fe}$  (wt%) and  $\text{Fe}^{2+}$  (wt%) and compared with the  $\text{Fe}^{3+}/\sum\text{Fe}$  value previously determined by Mössbauer spectroscopy (measured by Catherine McCammon at BGI). Results for  $\text{Fe}^{3+}/\sum\text{Fe}$  determined by Flank method using equation (1) are reported in Figure 3.4a plotted against the 1:1 line, indicating the lack of agreement between  $\text{Fe}^{3+}/\sum\text{Fe}$  determined by flank method and  $\text{Fe}^{3+}/\sum\text{Fe}$  determined by Mössbauer spectroscopy. The trend described by the UA garnet set plus the Standard garnets used in Höfer and Brey (2007) appears to fall apart with respect to the 1:1 line. The displacement of flank method results is also remarkable when comparing the  $\text{Fe}^{2+}$  contents (wt%) calculated from Mössbauer data and the ones calculated from the Flank method using equation (1) (Fig. 3.4b).

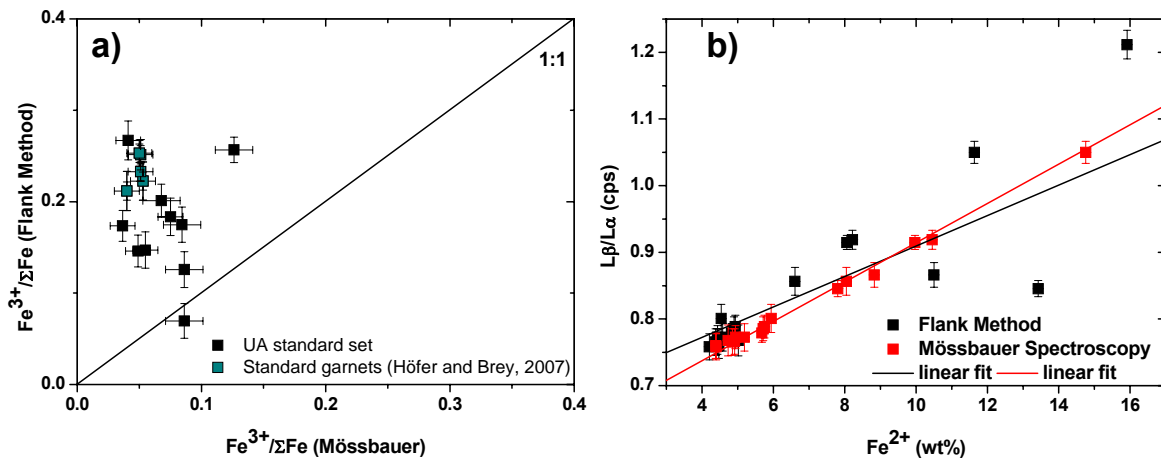


**Fig. 3.4** – a)  $\text{Fe}^{3+}/\sum\text{Fe}$  calculated for the UA garnet set using equation (1) compared to Mössbauer data; b)  $\text{L}\beta/\text{L}\alpha$  as a function of  $\text{Fe}^{2+}$  (wt%): red data set represents the Mössbauer data, whereas the black data set represents the Flank Method data. Vertical error bars in a) correspond to the  $1\sigma$  uncertainty of the mean value from 20-30 independent measurements at 15 kV and 80 nA, whereas the horizontal error bars correspond to the uncertainty reported for Mössbauer  $\text{Fe}^{3+}/\sum\text{Fe}$  ratios in Table 3.4. Error bars in b) referred to the  $\text{Fe}^{2+}$  obtained using equation (1) correspond to the propagation of independent errors such as  $\sum\text{Fe}$  uncertainty and  $\text{L}\beta/\text{L}\alpha$  obtained from the mean value of 20-30 independent measurements at 15 kV and 80 nA.

### 3. Results (1): Flank Method Calibration

On the basis of these observations, the calibration curve for garnets expressed through equation (1) cannot be considered universal. For this reason, data were fit to constrain a new calibration of the Flank Method for the Jeol JXA-8200 currently used at BGI. Since the variation of  $L\beta/L\alpha$  as a function of  $\sum\text{Fe}$  (wt%) and  $\text{Fe}^{2+}$  (wt%) appear to have the same behavior observed by Höfer and Brey (2007), the same calibration procedure adopted by previous authors was followed.

The general equation can be written as:

$$\text{Fe}^{2+} = A + B*(L\beta/L\alpha) + C*\sum\text{Fe} + D*\sum\text{Fe}*(L\beta/L\alpha). \quad (2)$$

The coefficients A, B, C and D have been determined applying a least-square regression model, and equation (2) becomes as follows:

$$\text{Fe}^{2+} = -11.614 + 17.883*(L\beta/L\alpha) + 0.648*\sum\text{Fe} - 0.153*\sum\text{Fe}*(L\beta/L\alpha). \quad (3)$$

$\text{Fe}^{3+}/\sum\text{Fe}$  values were calculated using the new equation (3) and compared with  $\text{Fe}^{3+}/\sum\text{Fe}$  calculated by Mössbauer spectroscopy. This time, results show a good agreement between Mössbauer and Flank method results (Fig. 3.5).

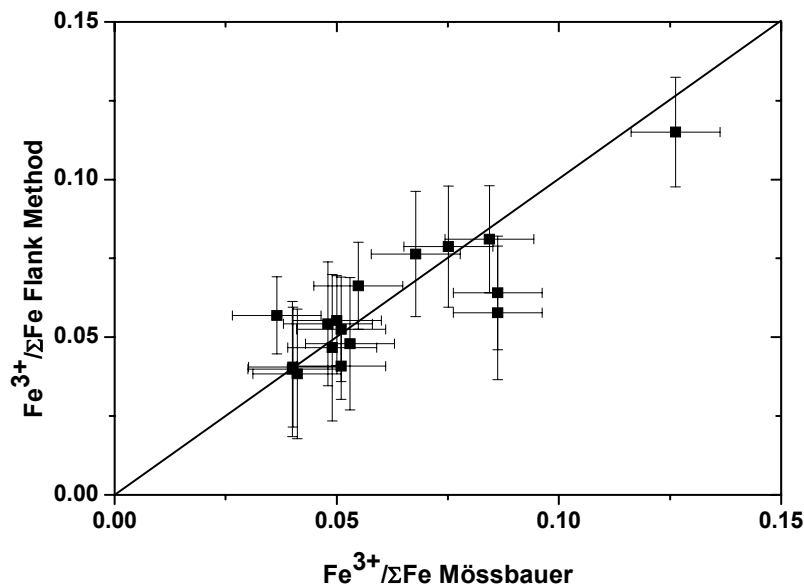


**Fig. 3.5** - Flank method calibration for the UA garnet set and the Standard garnet set on Jeol JXA-8200 currently used at BGI. The straight line represents the 1:1 ratio.

### 3. Results (1): Flank Method Calibration

To investigate the reliability of the calibration line, one of the standards (Mir1 sample) was excluded from the least-square regression model and the obtained equation (3) was applied to measure the  $\text{Fe}^{3+}/\Sigma\text{Fe}$  value to be compared to Mössbauer spectroscopy data. The variation of the  $L\beta/L\alpha$  ratio as a function of  $\text{Fe}^{2+}$  (wt%) shows good agreement with the trend described by the garnet sets (Fig. 3.6a). The comparison between the  $\text{Fe}^{3+}/\Sigma\text{Fe}$  ratio determined using equation (3) and that obtained by Mössbauer spectroscopy shows also good agreement for the Mir1 sample (Fig. 3.6b), as data fall within the error bars and are consistent with the garnet sets used for the calibration.

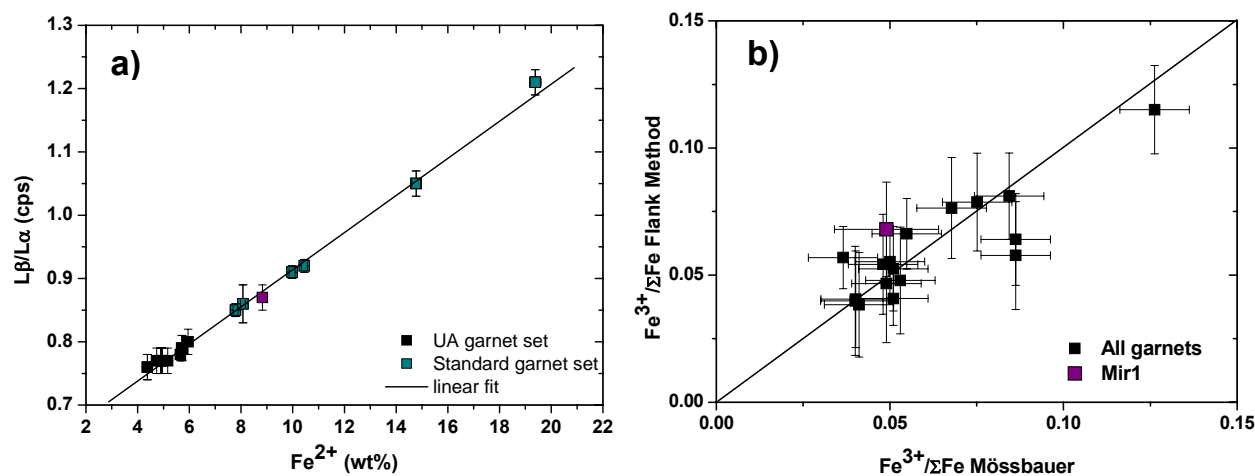


**Fig. 3.6** – a)  $L\beta/L\alpha$  variation as a function of  $\text{Fe}^{2+}$  (wt%) for Mir1 (purple data point) compared to the natural garnet sets; b)  $\text{Fe}^{3+}/\Sigma\text{Fe}$  determined by flank method compared to  $\text{Fe}^{3+}/\Sigma\text{Fe}$  determined by Mössbauer spectroscopy for the test Mir1, treated as unknown sample.

Regarding the flank method calibration for garnets, it can therefore be concluded that the equation cannot be considered universal for every microprobe in use. Thus, in order to measure the  $\text{Fe}^{3+}/\Sigma\text{Fe}$  ratio by electron microprobe, the calibration needs to be re-fit at each microprobe session using a set of garnet standards of known  $\text{Fe}^{3+}/\Sigma\text{Fe}$ .

### 3.3 Flank Method calibration for synthetic (Mg,Fe)O ferropericlyase: present study

All (Mg,Fe)O samples previously analyzed by Mössbauer spectroscopy were mounted on epoxy or on glass (thin section) and coated with a thin layer of carbon (10 nm) for electron microprobe analysis. A fresh coating is needed for flank method measurements, as it was shown that a bad coating can affect the results (Höfer and Brey, 2007). The temperature in the laboratory was monitored to ensure that it remained constant during measurements (no significant variation was observed), as temperature changes can affect the  $L\beta/L\alpha$  ratio and its stability through time. Major element analysis and flank method measurements were performed simultaneously. The bulk Fe content was initially measured as FeO, and subsequently corrected for the  $Fe^{3+}$  content using the  $Fe^{3+}/\Sigma Fe$  previously determined by Mössbauer spectroscopy.

The (Mg,Fe)O ferropericlyase set is the result of up to forty multi anvil experiments. Of all the experiments, only twenty-one synthetic (Mg,Fe)O samples were selected on the basis of their high homogeneity and high quality of the crystals. A subset of these samples were chosen to repeat the flank method measurements during different microprobe sessions in order to monitor the  $L\beta/L\alpha$  values and ensure their reproducibility and the stability of flank method measurements as a function of time (Fig. 3.7).

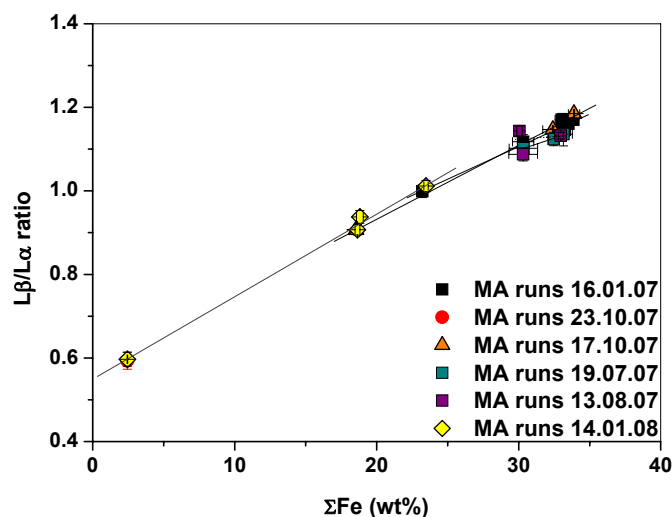


**Fig.3.7** – Reproducibility of flank method measurements on different days (date indicated) for the same set of (Fe,Mg)O crystals. No significant change in slope is apparent for different electron microprobe measuring days.

### 3. Results (1): Flank Method Calibration

Following the same approach used for the garnet calibration (see § 3.1), the behavior of the  $L\beta/L\alpha$  ratio was studied for the entire solid solution  $(Mg_xFe_{1-x})O$ -FeO as a function of bulk  $\Sigma Fe$  (wt%) and  $Fe^{2+}$  (wt%) concentration. Flank method measurements ( $L\beta/L\alpha$ ) show a strong correlation as a function of  $\Sigma Fe$  (wt%) within a Fe compositional range of 0.2-35wt.% (Fig. 3.8). This proves that the  $L\beta/L\alpha$  ratio is strongly sensitive also for ferropericlase and in particular for a low range of Fe content, which makes the flank method suitable to investigate natural  $(Mg,Fe)O$  occurring as diamond inclusions (typically covering such a range of  $\Sigma Fe$  bulk composition at lower mantle depths).

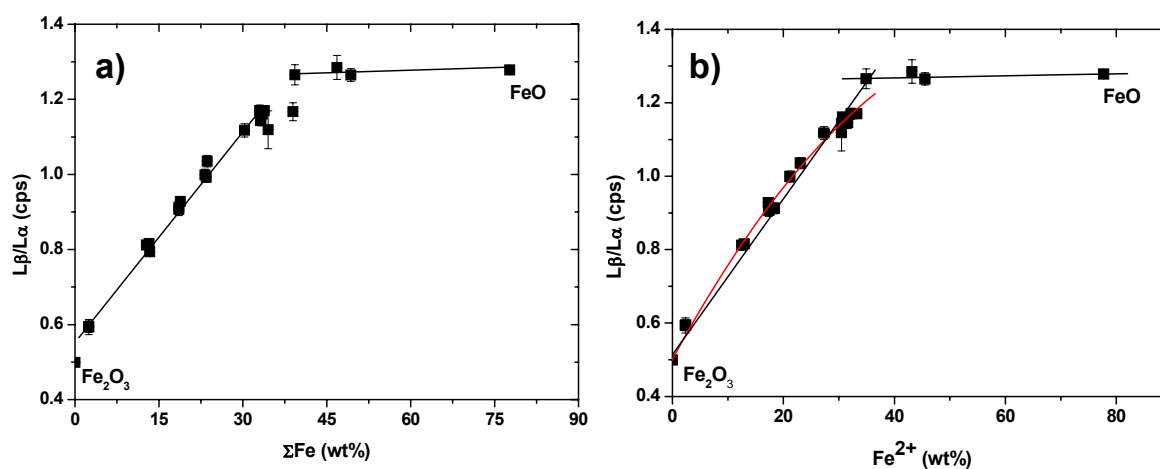


**Fig. 3.8** – a)  $L\beta/L\alpha$  variation as a function of  $\Sigma Fe$  (wt%) and b) as a function of  $Fe^{2+}$  (wt%) for synthetic  $(Mg,Fe)O$  crystals. All linear trends are represented by a black line, whereas the polynomial trend is represented by a red line.

As observed in Figure 3.8a, the slope described by the  $L\beta/L\alpha$  trend changes for  $\Sigma Fe$  concentrations higher than 35 wt.%, showing a decrease of  $L\beta/L\alpha$  values, and reaching a plateau for compositions close to the end member FeO. Therefore the  $L\beta/L\alpha$  ratio was measured also for the two end members  $Fe_2O_3$  and FeO, with the aim to study the variation of flank method measurements as a function of oxidation state. Results show that the values are consistent with the trend described for the complete solid solution. A similar trend to that observed for  $L\beta/L\alpha$  ratios versus  $\Sigma Fe$  (wt%) can also be observed as a function of  $Fe^{2+}$  (wt%) (Fig. 3.8b).

In the compositional range from zero to 35 wt.%, the trend appears to be close to linear as a function of  $\Sigma Fe$  (Fig. 3.8a), but deviates from the linear trend as a function of  $Fe^{2+}$  (wt%) (Fig. 3.8b).

### 3. Results (1): Flank Method Calibration

In contrast, the variation of  $L\beta/L\alpha$  versus  $Fe^{3+}$  (wt%) does not show a strong correlation (Fig. 3.9), mainly due to the matrix effect (see § 2.6).

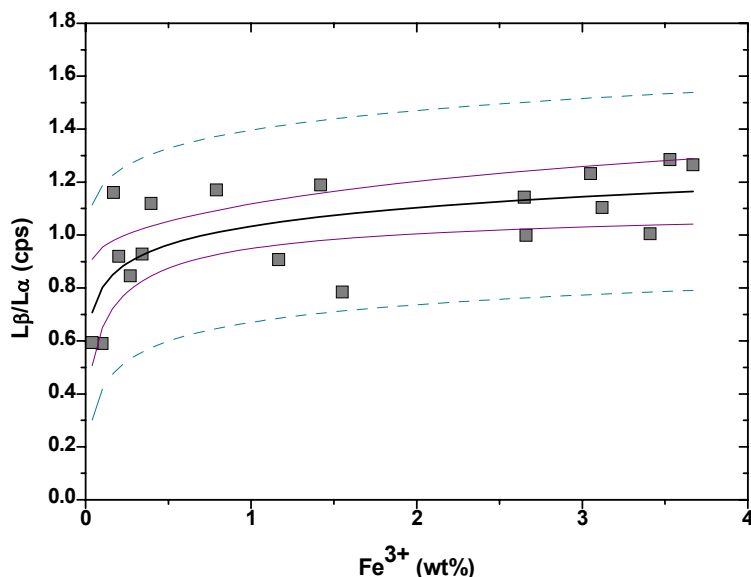


**Fig. 3.9** –  $L\beta/L\alpha$  measurements as a function of the  $Fe^{3+}$  (wt%) contents. Dashed green and solid purple lines indicate the 95% confidence and prediction intervals, respectively, obtained for the polynomial fit.

The sensitivity of the flank method for (Mg,Fe)O as a function of  $Fe^{2+}$  (wt%) decreases due to the Fe mass absorption coefficient, reaching saturation for FeO. This behavior is more evident for ferropericlasite than for garnet due to the higher amount of Fe in wt% in the former compared to the latter (Fig. 3.10), and therefore the effect is greater on the  $L\beta/L\alpha$  measurements. As a result, the nature of the correlation is also compromised (e.g., linear for garnets and polynomial for ferropericlasite).

### 3. Results (1): Flank Method Calibration

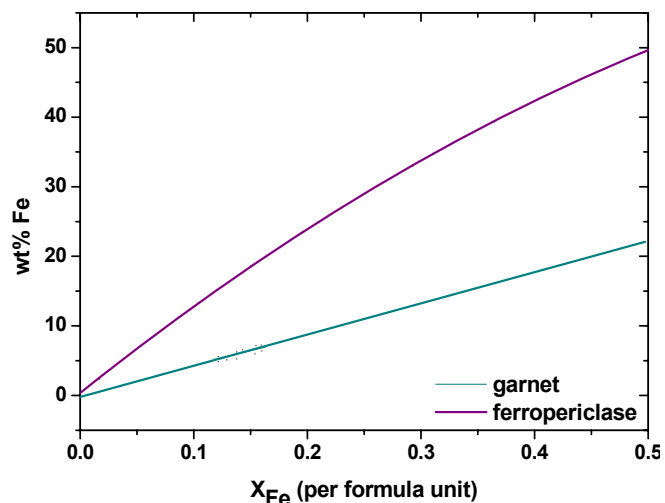


**Fig. 3.10** – Variation of Fe (wt%) as a function of the Fe molar fraction: comparison between ferropericlasite and garnet.

Flank method measurements were also performed directly on polycrystalline (Mg,Fe)O powders before performing multi anvil experiments, and although a positive correlation of  $L\beta/L\alpha$  as a function of  $Fe^{2+}$  can be observed following the same trend as the multi anvil run products, the poor quality of the surface analyzed leads to less accurate data which cannot be included in the data set. Figure 3.11 shows a comparison between the surface of a polycrystalline (Mg,Fe)O powder pellet (a) and of a (Mg,Fe)O single crystal after a Multi Anvil experiment (b).

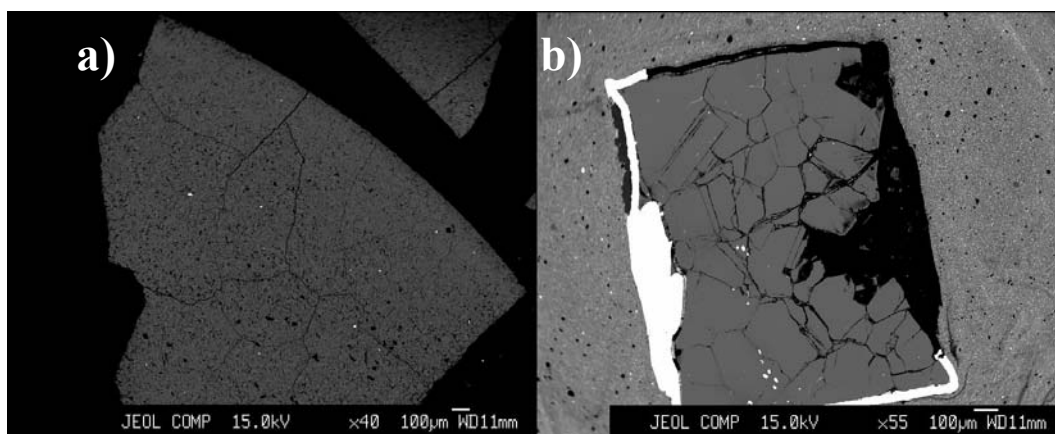


**Fig. 3.11** – Backscattered images taken at the Jeol JXA-8200 of a) (Mg,Fe)O polycrystalline powder (pellet fragment) and b) “quasi” single crystal (longitudinal capsule section). Multi anvil run products show a better surface for probe measurements. Scale corresponds to 100  $\mu$ m.

### 3. Results (1): Flank Method Calibration

In order to constrain the flank method calibration for (Mg,Fe)O, a first attempt was made assuming a linear correlation as a function of  $\text{Fe}^{2+}$  (wt%) for the compositional range from zero to 35 wt% (Fig.3.12a). As in the case of garnet, a least-square regression model was applied. As a result, the following equation was obtained:

$$\text{Fe}^{2+} = -20.463 + 38.453*(L\beta/L\alpha) + 0.147*\sum\text{Fe} - 0.311*\sum\text{Fe}*(L\beta/L\alpha). \quad \chi^2 = 0.294 \quad (4)$$

However, flank method results obtained using equation (4) do not show good agreement with the  $\text{Fe}^{3+}/\sum\text{Fe}$  determined by Mössbauer spectroscopy in the case of very low  $\text{Fe}^{3+}/\sum\text{Fe}$  ratios (<0.05), whereas they become more accurate for concentrations higher than >0.05 (Fig. 3.12b). Therefore the range 0-35 wt.% will be fit as a polynomial trend.

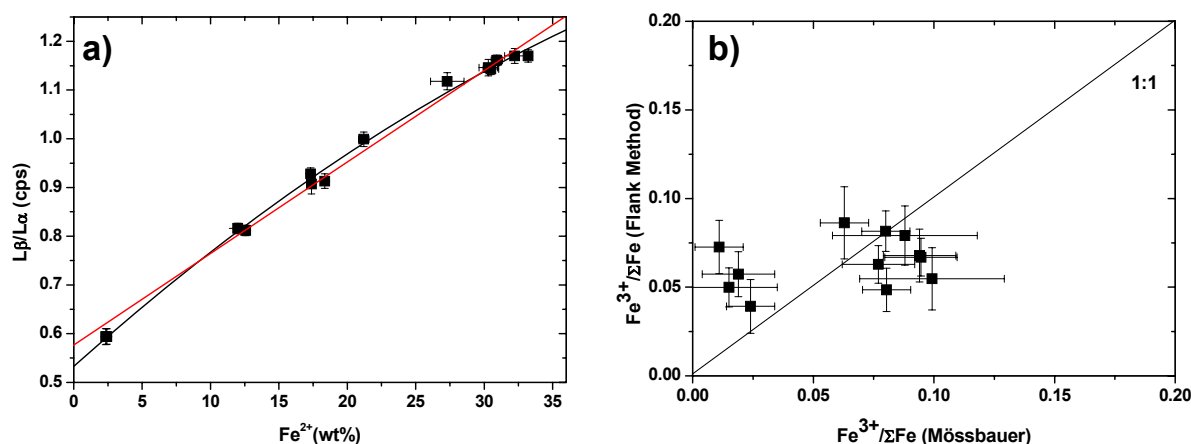


**Fig. 3.12** – **a)** Selected Multi Anvil run products using a linear trend (red line) plot. **b)** calibration line after fitting data according to a linear correlation expressed by equation (4).  $\chi^2 = 0.294$

Synthetic (Mg,Fe)O crystals in the Fe compositional range from 2 to 36.6% were selected for their high homogeneity to constrain a polynomial calibration curve. A least-squares regression model was applied to fit the three variables  $\sum\text{Fe}$ ,  $L\beta/L\alpha$  and  $\text{Fe}^{2+}$ . Linear regression lines were fit using MATLAB (Copyright 1984-2005, The MathWorks, Inc.; Version 7.1.0.246); whereas polynomial trends were fit using the software Table 3D Curve (Copyright © SYSTAT Software Inc., 1993-2002; Version 4.0). All of the mathematical solutions found from the software were analyzed. The best solution was selected considering the following criteria:

### 3. Results (1): Flank Method Calibration

- analyzing carefully the characteristics of the equations (e.g., function type, order of the equation) that better approximates the surface described by  $\Sigma\text{Fe}$ ,  $\text{Fe}^{2+}$  and  $L\beta/L\alpha$  values for the chosen compositional range;
- the number of parameters used to fit the three variables (in the case of garnets a maximum of 4 parameters were necessary to fit a linear correlation line);
- the goodness of fit (e.g.,  $R^2$  values).

Among all the equations found by the software, the ones characterized by a logarithmic component were selected, as the trends described by  $L\beta/L\alpha$  versus  $\Sigma\text{Fe}$  and  $\text{Fe}^{2+}$  (wt%) seem to follow a logarithmic behavior. Thus, three equations were selected as the best compromises for good fit and complexity and then compared to test the accuracy of the related calibration curves.

#### *Attempt no 1:*

The correlation between  $L\beta/L\alpha$  ratios and  $\text{Fe}^{2+}$  was considered polynomial for all samples with  $\text{Fe}^{2+}(\text{wt}\%) < 35$ , described by the following equation:

$$\text{Fe}^{2+} = 22.667 + 5.457 \cdot \ln(\Sigma\text{Fe}) - 77.549 \cdot (L\beta/L\alpha) + 59.117 \cdot (L\beta/L\alpha)^2. \quad R^2 = 0.996 \quad (5)$$

The  $\text{Fe}^{3+}/\Sigma\text{Fe}$  ratios were calculated indirectly applying equation (5) and compared to those measured by Mössbauer spectroscopy. Results are reported in Figure 3.13. Equation (5) does not appear to be sensitive to the variation of  $\text{Fe}^{3+}/\Sigma\text{Fe}$  compared to the Mössbauer data.

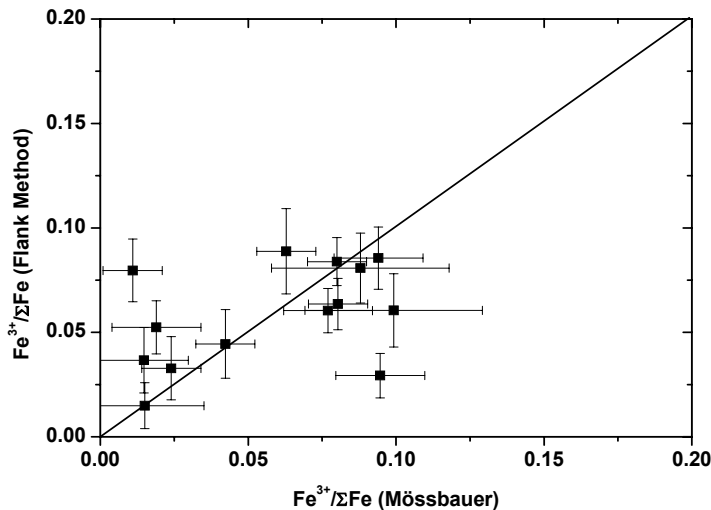


**Fig. 3.13** –  $\text{Fe}^{3+}/\Sigma\text{Fe}$ : comparison between Mössbauer data and Flank method data using equation (5). The  $\chi^2$  value is 0.278.

### 3. Results (1): Flank Method Calibration

Attempt no 2:

As second attempt, the following equation was considered:

$$\text{Fe}^{2+} = 35.511 + 3.515 \ln(\sum \text{Fe}) + 1.179 * (\ln(\sum \text{Fe}))^2 - 100.479 * \text{L}\beta/\text{L}\alpha + 63.609 * (\text{L}\beta/\text{L}\alpha)^2 \quad R^2 = 0.996 \quad (6)$$

Although equation (6) offers a higher number of degrees of freedom than equation (5), a comparison of  $\text{Fe}^{3+}/\sum \text{Fe}$  determined by Flank Method versus Mössbauer data show that results are not in good agreement along the 1:1 line (Fig. 3.14).

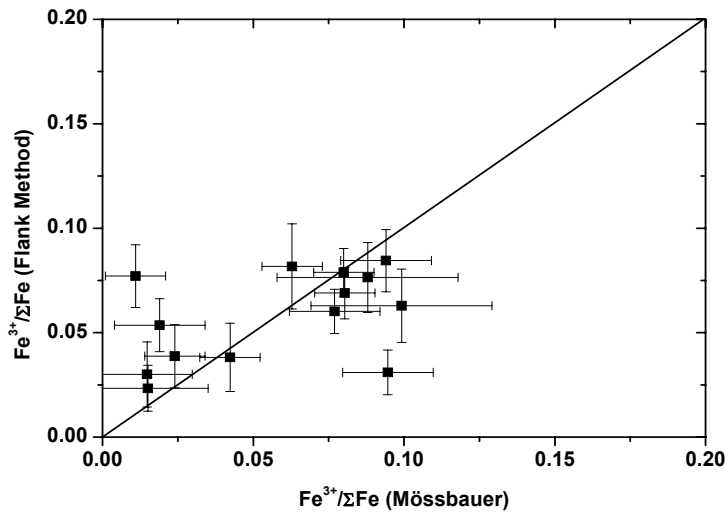


**Fig.3.14** -  $\text{Fe}^{3+}/\sum \text{Fe}$ : comparison between Mössbauer data and Flank method data according to equation (6). The  $\chi^2$  value is 0.265.

Attempt no 3:

As a final attempt, the following equation was chosen for comparison with the previous equations (5) and (6):

$$\text{Fe}^{2+} = 30.475 - 0.821 * \sum \text{Fe} + 0.012 * (\sum \text{Fe})^2 + 50.317 * \ln(\text{L}\beta/\text{L}\alpha) \quad R^2 = 0.9957 \quad (7)$$

Also in this case results for  $\text{Fe}^{3+}/\sum \text{Fe}$  determined by Flank Method versus Mössbauer data do not show a significant improvement along the 1:1 line (Fig. 3.15).

### 3. Results (1): Flank Method Calibration

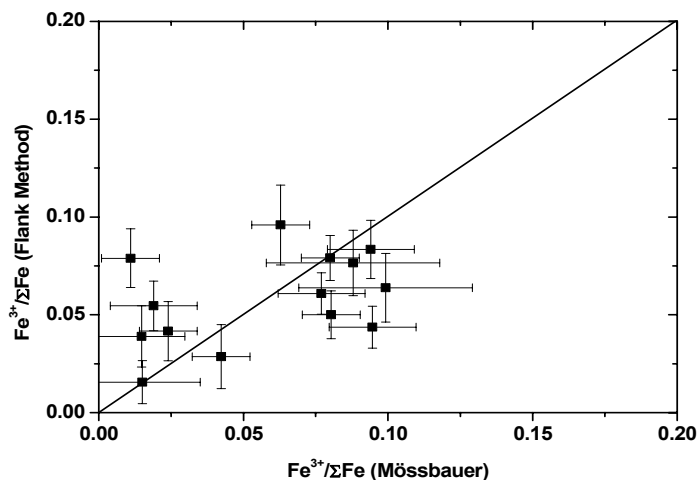


**Fig.3.15** -  $\text{Fe}^{3+}/\Sigma\text{Fe}$ : comparison between Mössbauer data and Flank method data according to equation (7). The  $\chi^2$  value is 0.285.

The  $\text{Fe}^{3+}/\Sigma\text{Fe}$  ratios determined using equations (5), (6) and (7) are summarized and compared in Table 3.7. Results obtained so far using the three different equations do not lead to a good approximation of Mössbauer data for flank method results, which is a requirement to constrain the flank method calibration. Therefore, a different strategy to fit the data set is needed.

### 3. Results (1): Flank Method Calibration

**Tab. 3.7** –  $\text{Fe}^{3+}/\Sigma\text{Fe}$  ratios determined using equation (5), (6) and (7) with relative  $\chi^2$  compared to Mössbauer data

Sample	$\Sigma\text{Fe}$	$L\beta/L\alpha$	$\text{Fe}^{2+}$	$\text{Fe}^{3+}/\Sigma\text{Fe}^*$	$\text{Fe}^{3+}/\Sigma\text{Fe}$ (5)	$\text{Fe}^{3+}/\Sigma\text{Fe}$ (6)	$\text{Fe}^{3+}/\Sigma\text{Fe}$ (7)
S4044	23.40(1)	0.99(1)	21.199	0.094	0.086	0.084	0.083
S4028	33.24(7)	1.15(2)	30.315	0.088	0.081	0.076	0.076
S3996	33.15(32)	1.14(1)	30.494	0.080	0.084	0.079	0.079
S3971	33.50(15)	1.16(1)	30.923	0.077	0.060	0.060	0.061
S3939	30.31(74)	1.12(2)	27.303	0.099	0.061	0.063	0.064
S3941	33.03(46)	1.17(2)	32.233	0.024	0.033	0.039	0.042
S3906	33.85(18)	1.17(1)	33.210	0.019	0.052	0.054	0.055
S3912	18.54(8)	0.91(2)	17.378	0.063	0.089	0.082	0.096
S4068	2.44(15)	0.59(2)	2.339	0.042	0.044	0.038	0.029
S4063	18.56(8)	0.91(2)	18.356	0.011	0.080	0.077	0.079
S4074	18.83(17)	0.93(1)	17.312	0.080	0.064	0.069	0.050
S4139	13.23(20)	0.82(1)	11.978	0.095	0.029	0.031	0.044
S4117	12.76(20)	0.81(1)	12.569	0.015	0.015	0.023	0.016
S4099	2.46(23)	0.59(2)	2.421	0.015	0.037	0.030	0.039
$\chi^2$					0.278	0.265	0.285

\*from Mössbauer data

In order to better constrain the flank method calibration for (Mg,Fe)O ferropericlase, a further attempt was made to improve the quality – whenever possible - of Mössbauer spectroscopy results and Flank Method results. With regard to Mössbauer spectroscopy results, left halves and right halves of all the spectra that showed some anomalies during data collection (unusual asymmetries in the spectrum shape) or of samples showing relevant deviations from the main data trend were fitted independently (without folding the two halves of the spectra) and compared in a second step. In some cases, the separate fit of the two halves produced different  $\text{Fe}^{3+}/\Sigma\text{Fe}$  values, most of the time due to mechanical problems in the spectrometer components (e.g., transducer, instrumental vibrations occurring during the measurements, etc.). In such cases, the fit of the two halves gave different results for the  $\text{Fe}^{3+}/\Sigma\text{Fe}$  and therefore the most accurate ratios were chosen as new  $\text{Fe}^{3+}/\Sigma\text{Fe}$ . At the same time, in order to avoid any kind of problems associated with the electron microprobe (i.e., spectrometer shifts), the highest number of samples possible were measured during the same

### 3. Results (1): Flank Method Calibration

microprobe sessions in order to compare data collected in the same day, avoiding comparison of those collected during different working sessions.

Table 3.8 reports bulk Fe compositions, the related  $L\beta/L\alpha$  ratios for the selected twenty-one (Mg,Fe)O and new  $Fe^{3+}/\Sigma Fe$  values after re-fitting some of the Mössbauer spectra. As a result, the behavior of the  $L\beta/L\alpha$  ratio as a function of bulk  $\Sigma Fe$  and  $Fe^{2+}$  (wt%) has been dramatically improved (Fig. 3.16 and Fig. 3.17).

**Tab. 3.8** –  $\Sigma Fe$  (wt%),  $L\beta/L\alpha$  ratios and  $Fe^{3+}/\Sigma Fe$  for synthetic (Mg,Fe)O single crystals.

Run	$\Sigma Fe$ (wt%)	±	$L\beta/L\alpha$ (cps)	±	$Fe^{3+}/\Sigma Fe$ (%) *	±	$Fe^{2+}$ (wt%)
S3912	18.54	0.08	0.907	0.016	6.29	0.015	17.37
S3971	33.5	0.15	1.161	0.01	7.7	0.015	30.92
S3906	33.85	0.18	1.17	0.01	1.19	0.015	33.45
S4149	34.51	0.26	1.119	0.05	11.63	0.015	26.92
S4074	18.83	0.17	0.928	0.01	8.04	0.015	17.32
S4068	2.44	0.15	0.594	0.02	4.23	0.01	2.34
S4099	2.46	0.23	0.594	0.02	1.55	0.01	2.42
S4117	12.57	0.15	0.846	0.019	2.11	0.02	12.3
S4139	13.23	0.07	0.816	0.013	11.72	0.015	11.68
S4063 II	18.4	0.04	0.919	0.029	1.1	0.015	18.19
S4044 II	22.79	0.15	0.999	0.022	11.66	0.015	20.13
S4123	22.98	0.08	1.005	0.021	14.82	0.01	19.57
S3855	18.73	1.51	0.911	0.025	5	0.01	17.79
S3939	29.58	0.75	1.1042	0.026	10.55	0.025	26.46
S3941	33.06	0.46	1.1702	0.0151	2.4	0.01	32.27
S3996	33.15	0.32	1.143	0.0114	8	0.01	30.49
S4028 II	34.439	0.46	1.189	0.021	4.26	0.03	32.01
S4153 t	39.72	0.53	1.232	0.022	7.69	0.015	36.67
S4155	46.82	0.26	1.285	0.033	7.53	0.015	43.29
S4265	77.71	0.31	1.4303	0.016	-	-	-
S4179	38.946	0.25	1.165	0.022	-	-	-
S4080	49.31	0.237	1.265	0.016	8.058	0.015	41.84

\*Measured by Mössbauer spectroscopy

3. Results (1): Flank Method Calibration

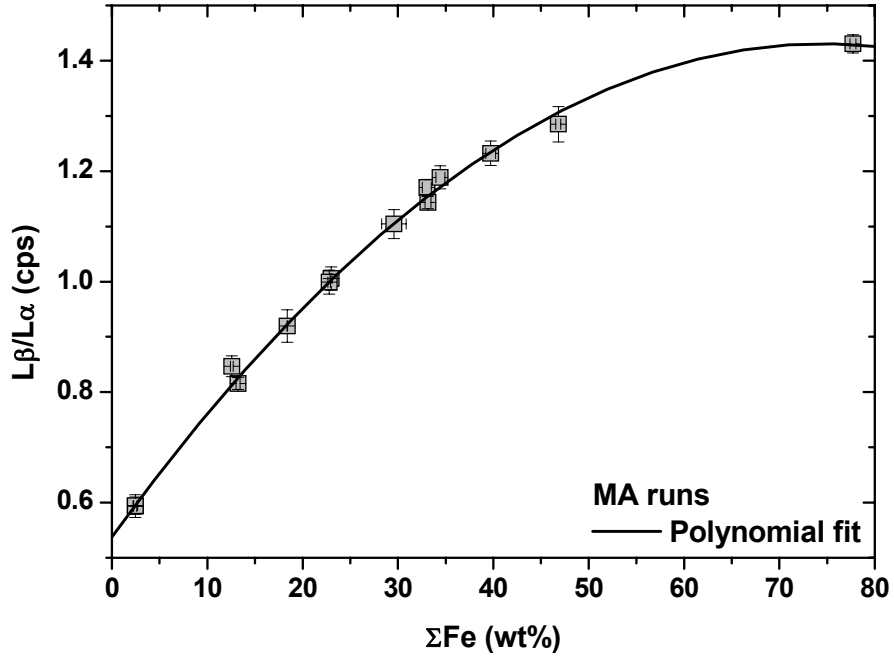


Fig.3.16 –  $L\beta/L\alpha$  variation as a function of  $\Sigma\text{Fe}$  (wt%) for synthetic (Mg,Fe)O crystals.

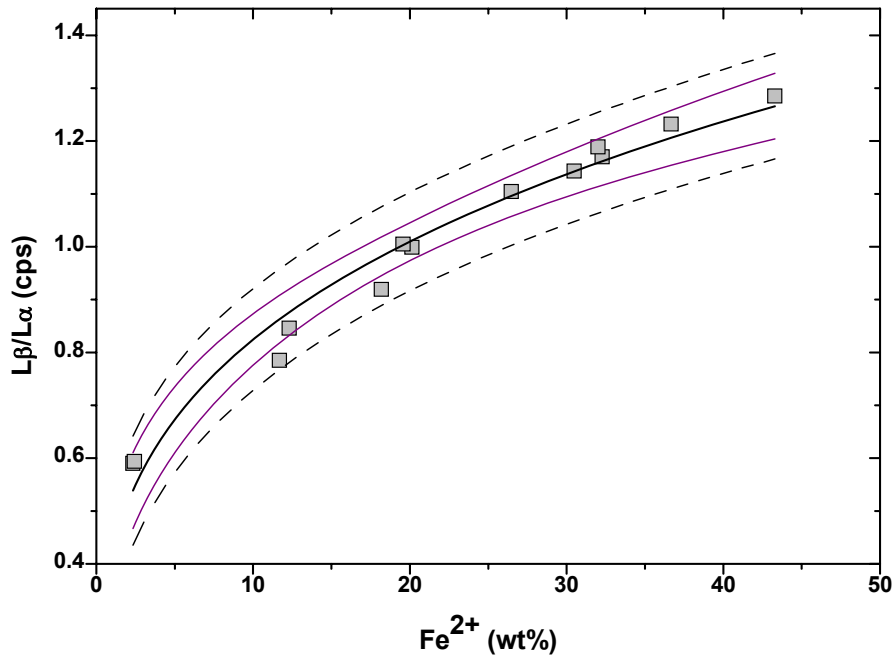


Fig. 3.17 –  $L\beta/L\alpha$  variation as a function of  $\text{Fe}^{2+}$  (wt%) for synthetic (Mg,Fe)O crystals calculated from Mössbauer data. Dashed grey and solid purple lines indicate the 95% confidence and prediction intervals, respectively, obtained for the polynomial fit.

### 3. Results (1): Flank Method Calibration

Of all the (Mg,Fe)O crystals synthesized, only eleven samples in the Fe compositional range from 2 to 46.8 % were selected for their high homogeneity to constrain a robust flank method calibration using a relative simple equation. Results provide a new regression curve using an equation with four terms to fit the data set  $z = a + b \cdot \ln x + cy + dy^2$ , where a,b,c and d are constants, x is  $\sum\text{Fe}$  (wt%), y corresponds to  $L\beta/L\alpha$  and z corresponds to the unknown  $\text{Fe}^{2+}$  (wt%). Therefore the calibration established for (Mg,Fe)O becomes:

$$\text{Fe}^{2+} = 46.238 + 8.161 * \ln (\sum\text{Fe}) - 137.01 * (L\beta/L\alpha) + 85.57 * (L\beta/L\alpha)^2 . \quad R^2 = 0.997 \quad (8)$$

$$\chi^2 = 0.151$$

Equation (8) was then used to calculate  $\text{Fe}^{3+}/\sum\text{Fe}$  and compare the new values to the  $\text{Fe}^{3+}/\sum\text{Fe}$  ratios previously determined by Mössbauer spectroscopy (Tab.3.9). Figure 3.18 shows that Flank Method results obtained applying equation (8) gives an agreement within 1  $\sigma$  with  $\text{Fe}^{3+}/\sum\text{Fe}$  determined by Mössbauer spectroscopy.

**Table 3.9** - Synthetic (Mg,Fe)O used for the calibration of the flank method.  $\text{Fe}^{3+}/\sum\text{Fe}$  determined using equation (8) and  $\text{Fe}^{3+}/\sum\text{Fe}$  determined by Mössbauer spectroscopy are compared with their relative errors.

Run	$\text{Fe}^{3+}/\sum\text{Fe}$	$\text{Fe}^{3+}/\sum\text{Fe}$ flank	Mössbauer	Flank Method
	Mössbauer	method	error	error
S4068	0.042	0.038	0.010	0.020
S4099	0.016	0.035	0.010	0.020
S4117	0.021	0.026	0.020	0.019
S4139	0.117	0.056	0.015	0.013
S4044	0.117	0.110	0.015	0.022
S4123	0.148	0.105	0.010	0.021
S3939	0.106	0.090	0.025	0.026
S3941	0.024	0.042	0.010	0.015
S3996	0.08	0.094	0.010	0.011
S4028	0.043	0.036	0.030	0.021
S4153	0.077	0.058	0.015	0.022
S4155	0.075	0.084	0.015	0.033

### 3. Results (1): Flank Method Calibration

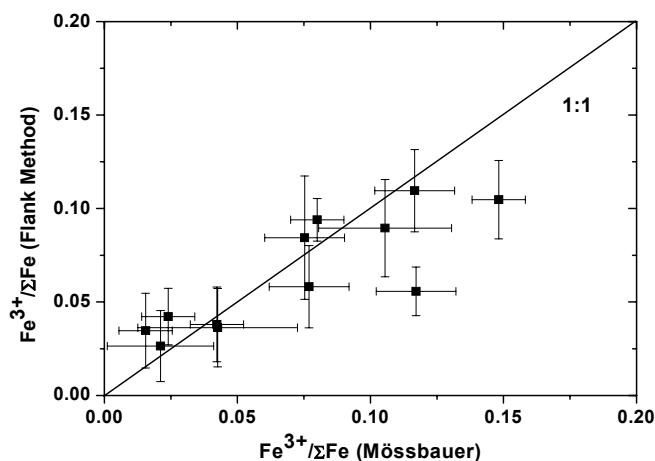


**Fig. 3.18** –  $\text{Fe}^{3+}/\Sigma\text{Fe}$  in synthetic (Mg,Fe)O determined using the flank method according to equation (7) vs.  $\text{Fe}^{3+}/\Sigma\text{Fe}$  determined using Mössbauer spectroscopy. The calibration was made from 11 of the synthetic (Mg,Fe)O crystals.

The established calibration was additionally tested on a synthetic (Mg,Fe)O sample of unknown  $\text{Fe}^{3+}/\Sigma\text{Fe}$  not included in the calibration fit. The  $\text{Fe}^{3+}/\Sigma\text{Fe}$  value was initially determined by Mössbauer spectroscopy and subsequently by flank method using equation (8). Results are reported in Figure 3.19 and show that Mössbauer measurements and flank method measurements are consistent and the data point (in red) falls within the experimental error.

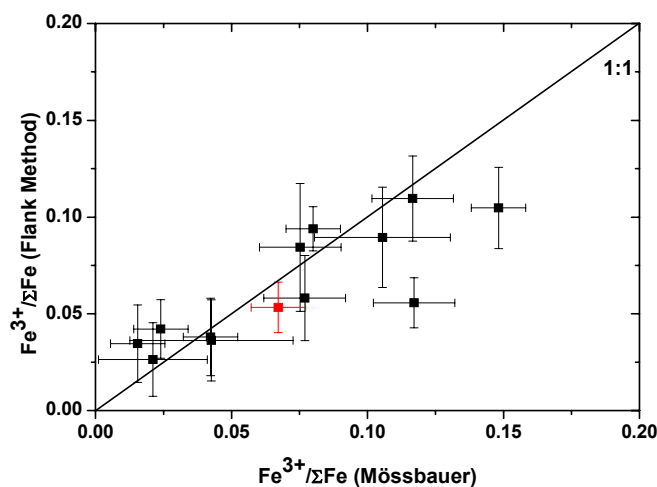


**Fig. 3.19** –  $\text{Fe}^{3+}/\Sigma\text{Fe}$  in synthetic (Mg,Fe)O: Comparison between Mössbauer data and Flank method data for the run product S4251 (in red). Results obtained by the two different methods are consistent with the calibration curve and show good agreement within the experimental error.

### 3. Results (1): Flank Method Calibration

**Table 3.10** – Comparison between  $\text{Fe}^{3+}/\Sigma\text{Fe}$  determined by Mössbauer spectroscopy and flank method collected for the same sample.

Sample	$\text{Fe}^{3+}$ (wt%)	$\text{Fe}^{3+}/\Sigma\text{Fe}$
S4251 Mössbauer spectroscopy	0.70(1)	0.05(1)
S4251 Flank Method	0.79(1)	0.07(1)

#### 3.3.1 A new calibration after spectrometer adjustments

In the timeframe between September 2008 and January 2009 maintenance was done on the electron microprobe at Bayerisches Geoinstitut, and new adjustments of the spectrometers were needed. As a consequence, flank method measurements were affected by instrumental changes in the characteristics and the  $L\beta/L\alpha$  ratio suffered of a shift of the measurements, which so far had showed to be reproducible over time (Fig. 3.7). The variation of  $L\beta/L\alpha$  ratios as a function of Fe bulk composition (wt%) in Fig. 3.20 shows the trend for synthetic (Mg,Fe)O before December 2008 and the shift after spectrometer adjustments. As equation (8) can no longer be applied, a new calibration curve needed to be established for the new mechanical setup of the electron microprobe at Bayerisches Geoinstitut.

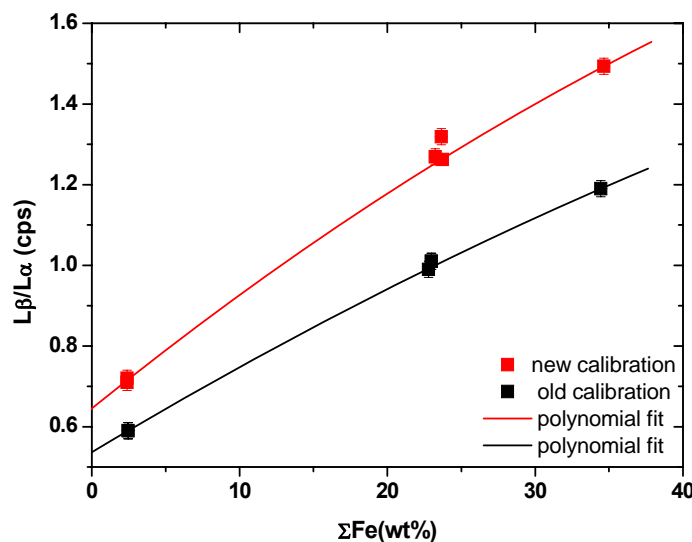


**Fig. 3.20** – Variation of the  $L\beta/L\alpha$  (cps) intensities after adjustments made on the TAP spectrometer used for flank method measurements.

### 3. Results (1): Flank Method Calibration

The same approach used to obtain equation (8) was applied to the new data set. The new calibration curve was established using eight synthetic (Mg,Fe)O ferropericlasite samples and an equation of the same type as equation (8) ( $z = a + b \cdot \ln x + cy + dy^2$ ), so that:

$$\text{Fe}^{2+} = -13.521 - 1.044 \ln \sum \text{Fe} + 15.522 \text{L}\beta/\text{L}\alpha + 11.258 (\text{L}\beta/\text{L}\alpha)^2. \quad R^2 = 0.995 \quad (9)$$

$$\chi^2 = 0.1436$$

$\text{Fe}^{3+}/\sum \text{Fe}$  measured by the flank method is again in good agreement with  $\text{Fe}^{3+}/\sum \text{Fe}$  measured by Mössbauer spectroscopy (Fig. 3.21), showing a lower  $\chi^2$  compared to the one reported for equation (8).

Equation (9) was additionally tested on an unknown synthetic (Mg,Fe)O sample which was not included in the calibration fit. Results obtained are consistent with the trend observed between flank method and Mössbauer spectroscopy measurements. Thus, the new calibration can be applied for the determination of  $\text{Fe}^{3+}/\sum \text{Fe}$  in synthetic and natural (Mg,Fe)O ferropericlasite over a compositional range between 2 and 40 wt.%.

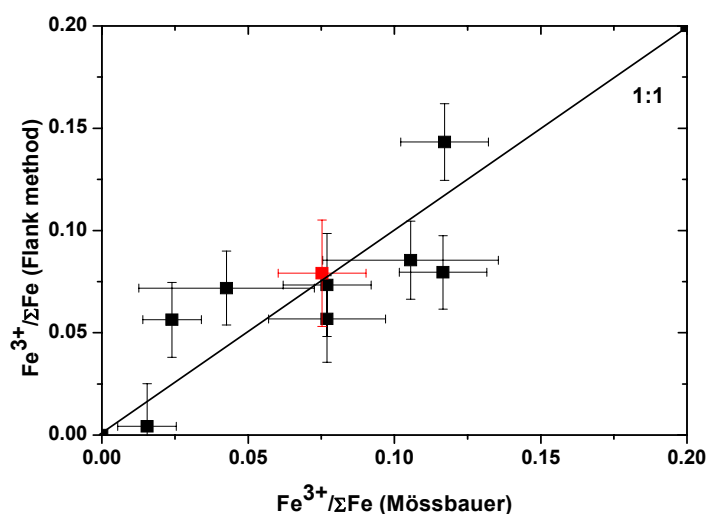


**Fig. 3.21** –  $\text{Fe}^{3+}/\sum \text{Fe}$  in synthetic (Mg,Fe)O: Comparison between Mössbauer data and Flank method data after spectrometer adjustments. The run product S4123 (in red) was used as unknown sample to test the new calibration (equation 9). Results are consistent with the calibration curve and show good agreement within the experimental error.

Bulk  $\sum \text{Fe}$  (wt%) and  $\text{L}\beta/\text{L}\alpha$  ratios remain constant at each microprobe session and are not affected by mechanical variations during different microprobe sessions (provided no maintenance adjustments are made to the spectrometers). Therefore the data collected are comparable with all

### 3. Results (1): Flank Method Calibration

results previously measured during different microprobe sessions. This represents a big advantage of the flank method calibration on (Mg,Fe)O, and the calibration equation (8 or 9) can be applied at every microprobe session, with no need to extrapolate a new equation every working day (as in the case of the garnet calibration), with consequent saving of time. Thus, once the calibration curve is established for a given electron microprobe, the calibration curve can be considered universal if the spectrometer adjustments remain identical with time. In order to ensure that there have been no changing from previous microprobe session, it would only be necessary to measure one sample as a standard to check the bulk  $\Sigma\text{Fe}$  (wt%) and the  $L\beta/L\alpha$  ratio. On the other hand, as shown above, a new calibration curve would need to be made after any kind of maintenance regarding spectrometer adjustments or replacements.

All samples were also tested during microprobe sessions to check their homogeneity. As already mentioned, nearly all synthetic (Mg,Fe)O crystals appeared to be homogeneous, with a random variation of  $L\beta/L\alpha$  vs. bulk Fe (wt%) within experimental error. However, sample S4149 showed a strong variation of  $L\beta/L\alpha$  ratios, ranging from 1.03 to 1.23 cps, with an increase of FeO content of about 10 wt% between the outer and inner regions of the crystal (Fig. 3.22).

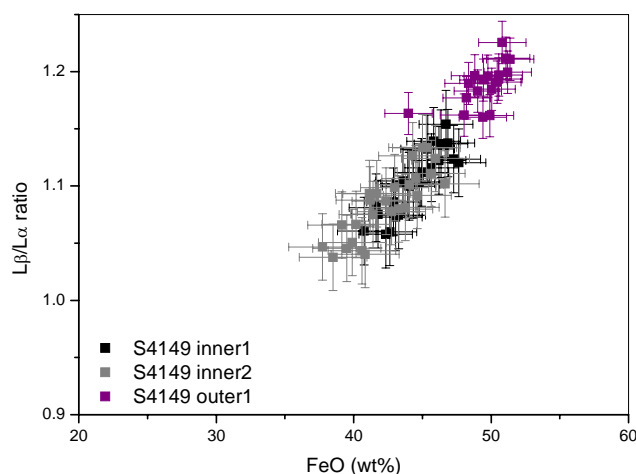


**Fig. 3.22** –  $L\beta/L\alpha$  as a function of FeO (wt%) in one of the synthetic samples which was shown to be inhomogeneous.

The strong correlation found might be due to diffusion processes occurring during synthesis that caused the zoning. The sample was therefore omitted from calibration regression curve calculations. However this result raises the possibility that the flank method might be useful in diffusion studies.

## 4. Results (2): Flank Method Applications

### 4.1 Synthetic (Mg,Fe)O from a different study

#### 4.1.1 (Mg,Fe)O containing secondary mineral phases

Flank method measurements were carried out also on 8 synthetic (Mg,Fe)O samples synthesized by inter-diffusion of Fe and Mg between single-crystal MgO and (Mg,Fe)O pre-reacted powders. The final iron compositional range was between 6-75 wt.%, with  $\text{Fe}^{3+}/\Sigma\text{Fe}$  ranging from 1 to 13 at.% (Jacobsen et al., 2002). The 8 synthetic (Mg,Fe)O samples were kindly supplied by Steven Jacobsen and Stephen Mackwell.

Flank method measurements show that the  $L\beta/L\alpha$  ratio increases with increasing bulk  $\Sigma\text{Fe}$  (wt%) and  $\text{Fe}^{2+}$  (wt%), but the comparison with the theoretical trend described by synthetic (Mg,Fe)O single crystals from the present study reveals that the  $L\beta/L\alpha$  ratio is either underestimated or overestimated, except for two experimental data points (Fig. 4.1). The deviation of data points from the theoretical trend described for synthetic (Mg,Fe)O (present work) becomes more clear for the variation of the  $L\beta/L\alpha$  ratio as a function of  $\text{Fe}^{2+}$  (wt%).

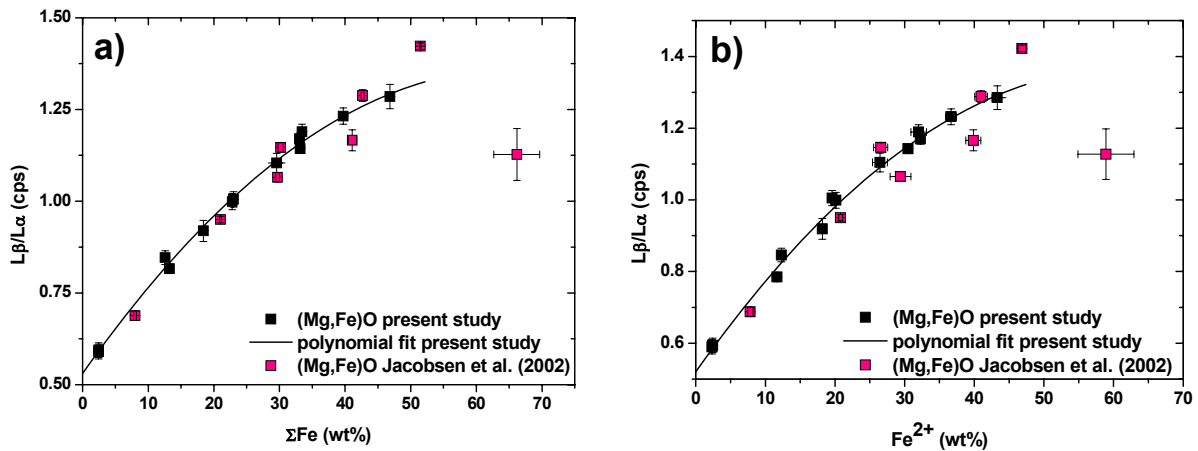


**Fig. 4** – Flank method measurements versus  $\Sigma\text{Fe}$  (%) (a) and  $\text{Fe}^{2+}$  (%) (b) on (Mg,Fe)O samples from Jacobsen et al. (2002) (in red) compared to synthetic (Mg,Fe)O samples from the present study (in black). Error bars for  $\text{Fe}^{2+}$  (b) are propagated using equation (2).

#### 4. Results (2): Flank Method Applications

A more careful investigation by Mössbauer spectroscopy on the new set of (Mg,Fe)O samples revealed that a reasonable amount of magnesioferrite (Mg,Fe)Fe<sub>2</sub>O<sub>4</sub> can be detected and was estimated to be between 0.2 and 11% by volume. In fact, additional peaks in the Mössbauer spectrum appeared over the velocity range of 4 mm/s, typically due to the presence of magnetic components (Fig. 4.2). Two additional components (magnetic sextets) were needed to fit the spectra (compared to pure ferropericlase which needed only three different doublets for the fitting procedure), and were assigned to the magnesioferrite contribution.

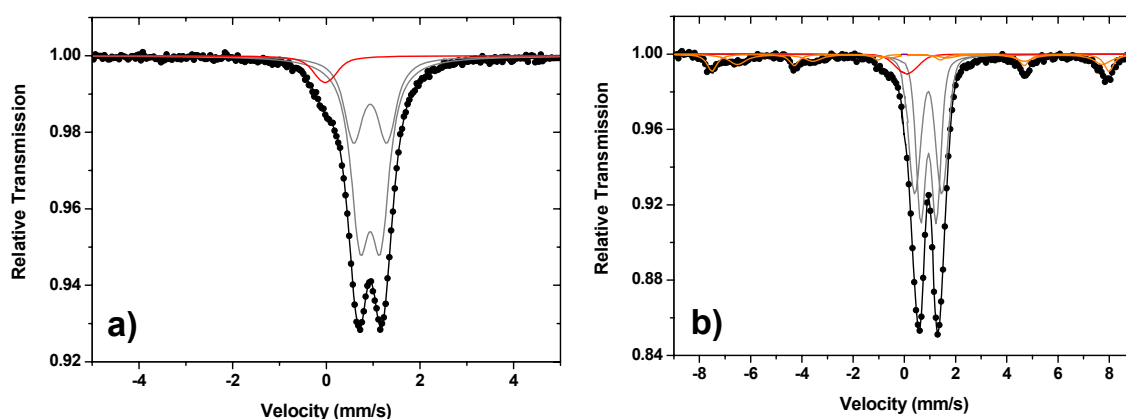


**Fig. 4.2** – a) Mössbauer spectrum for a pure (Mg,Fe)O from the present study (sample S4251); b) Mössbauer spectrum for a (Mg,Fe)O sample containing a percentage of magnesioferrite (Mg,Fe)Fe<sub>2</sub>O<sub>4</sub> (sample #27). Dots represent experimental data, black lines the fitted curves, grey lines Fe<sup>2+</sup> doublets, and red lines Fe<sup>3+</sup> doublets. In addition, the orange lines in b) represent the magnetic component (recognizable as sextets).

The amount of magnesioferrite exsolved from the primary (Mg,Fe)O during re-equilibration experiments is present in amounts proportional to the relative areas and corrected for the Fe molar fraction in each phase (Table 4.1).

#### 4. Results (2): Flank Method Applications

**Tab. 4.1-** L $\beta$ /L $\alpha$  ratios as a function of Fe<sup>2+</sup> (wt%) and the (Mg,Fe)Fe<sub>2</sub>O<sub>4</sub> % by volume

Sample	Fe <sup>2+</sup> (wt%)	±	L $\beta$ /L $\alpha$	±	xFe	Fe <sup>3+</sup> / $\Sigma$ Fe	±	vol% (Mg,Fe)Fe <sub>2</sub> O <sub>4</sub>	±
#6	7.828	0.195	0.688	0.013	0.058	0.02	0.01	0.2	0.1
#15	20.798	0.147	0.950	0.009	0.149	0.01	0.01	0.7	0.5
#24	29.409	0.646	1.065	0.013	0.239	0.01	0.03	Not detected	-
#27	39.047	0.276	1.166	0.029	0.265	0.05	0.03	1	1
#37	41.49	0.205	1.288	0.016	0.366	0.04	0.02	7	4
#53	46.847	0.100	1.423	0.009	0.527	0.09	0.01	Not detected	-
#56	26.261	0.414	1.146	0.013	0.561	0.12	0.02	9	5
#75	58.236	3.49	1.127	0.071	0.75	0.11	0.03	11	6

The presence of magnesioferrite was additionally proved by comparing Transmission Electron Microscopy (TEM) studies conducted on two (Mg,Fe)O samples with the same Fe molar fraction and similar Fe<sup>3+</sup>/ $\Sigma$ Fe ratio chosen from each set. Thus, a synthetic (Mg,Fe)O sample chosen from the present study and one (Mg,Fe)O chosen from Jacobsen et al. (2002) with xFe (at.%) = 15 were compared. Dark Field (DF) microphotographs are reported in Figure 4.3 to show the differences in texture between the two samples. Figure 4.3a shows clearly cubic shaped magnesioferrite impurities of sizes smaller than 1  $\mu$ m in the (Mg,Fe)O matrix; whereas Figure 4.3b shows pure (Mg,Fe)O free of additional phases.

#### 4. Results (2): Flank Method Applications

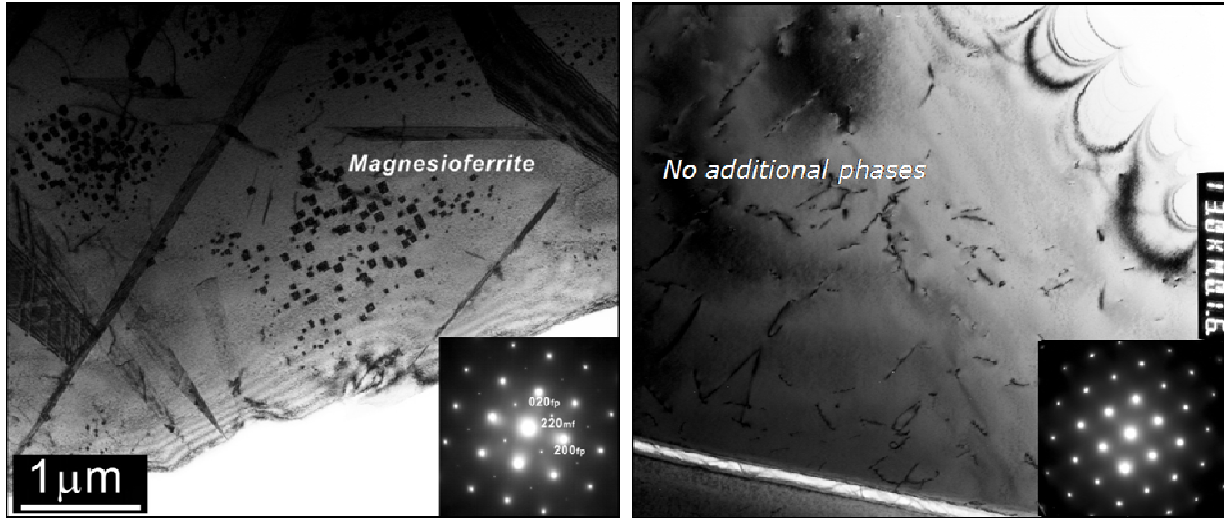


**Fig. 4.3** –TEM Dark Field microphotographs showing a comparison between (Mg,Fe)O from a) (Mg,Fe)O from Jacobsen et al. (2002) (sample Fe15) and b) (Mg,Fe)O from the present study (sample S3855). Lamellar structures visible in both textures are caused by stacking faults.

A possible explanation of the presence of magnesioferrite in (Mg,Fe)O lies in a variation of the oxygen fugacity conditions during the re-equilibration experiments, which crossed into the (Mg,Fe)Fe<sub>2</sub>O<sub>4</sub> stability field. As a result, a secondary phase exsolved from the primary (Mg,Fe)O crystals.

The deviation from the theoretical trend for the second set of (Mg,Fe)O samples observed in Figure 4.1 is possibly due to the sensitivity of flank method measurements able to detect the presence of magnesioferrite in (Mg,Fe)O. In fact, due to the small size of the impurities in (Mg,Fe)O, their contribution to major element analysis and flank method measurements cannot be avoided. Thus,  $\Sigma\text{Fe}$  (wt%) and  $L\beta/L\alpha$  ratios would be affected by the contribution of extra phases.

On the basis of estimations of the ferrite content (vol.%) from Mössbauer data, an attempt was made to correct the bulk Fe contents (wt%) in order to exclude the magnesioferrite contribution from the measurements. The flank method calibration was therefore applied to calculate the expected  $L\beta/L\alpha$  ratio using equation (8) (see § 3.3) by knowing the corrected  $\Sigma\text{Fe}$  (wt%). The re-calculated  $L\beta/L\alpha$  ratios refer only to (Mg,Fe)O phase, excluding the magnesioferrite contribution (Tab. 4.2).

#### 4. Results (2): Flank Method Applications

**Tab. 4.2** - Difference between  $L\beta/L\alpha$  observed and  $L\beta/L\alpha$  calculated, after omitting the ferrite contribution.

Sample	$\Sigma\text{Fe}$ (wt%)	(Mg,Fe)Fe <sub>2</sub> O <sub>4</sub> (vol.%)	$L\beta/L\alpha$ obs	$L\beta/L\alpha$ calc	$\Delta L\beta/L\alpha$
#6	7.989	0.2	0.688	-	
#15	21.001	0.7	0.950	1.029	-0.079
#27	41.102	1	1.166	1.257	-0.091
#37	42.669	7	1.288	1.288	0.0001
#56	30.185	9	1.146	1.059	0.086
#75	66.177	11	1.127	1.364	-0.237

By comparison with the theoretical trend for pure (Mg,Fe)O it can be observed that the new corrected values for  $L\beta/L\alpha$  as a function of the corrected  $\Sigma\text{Fe}$  (wt%) now fall on the calibration line (Fig. 4.4). Therefore it was possible to isolate the contribution of magnesioferrite and treat the samples as pure (Mg,Fe)O.

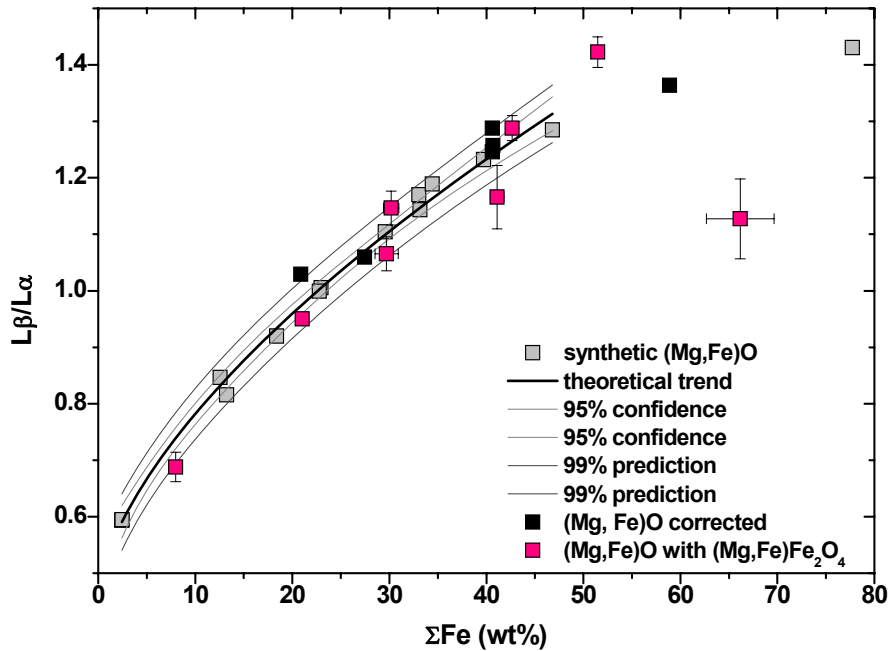


**Fig. 4.4** – Flank method measurements on samples with presence of Fe<sub>3</sub>O<sub>4</sub> impurities (in red) compared to the theoretical trend described by pure (Mg,Fe)O samples (in gray). In black are the corrected (Mg,Fe)O data after isolating the Fe<sub>3</sub>O<sub>4</sub> contribution to bulk Fe (wt%) and  $L\beta/L\alpha$  measurements.

#### 4. Results (2): Flank Method Applications

The flank method could be potentially extended to natural (Mg,Fe)O inclusions from lower mantle diamonds to investigate the presence of exsolution. Ideally it may be possible to quantify the amount of magnesioferrite in natural samples by knowing the variation of  $L\beta/L\alpha$  as a function of  $\Sigma\text{Fe}$  (wt%). However, on the basis of data obtained so far, there is no consistent increase of  $L\beta/L\alpha$  ratio as a function of (Mg,Fe)Fe<sub>2</sub>O<sub>4</sub> content; hence it is not feasible to extrapolate theoretical curves (which would be a family of curves for different  $\Sigma\text{Fe}$  values) characterized by the same amount of (Mg,Fe)Fe<sub>2</sub>O<sub>4</sub> content to correct  $L\beta/L\alpha$  ratios of natural samples for a magnesioferrite contribution.

##### 4.1.2 (Mg,Fe)O from High Pressure High Temperature diffusion experiments

In order to enlarge the data set, flank method studies were expanded to an additional set of (Mg,Fe)O samples involving an investigation of diffusion. Samples were synthesized with the aim to investigate point defect and point defect-related properties (kindly provided by Kazuhiko Otsuka, University of Yale). Three (Mg,Fe)O crystals from a much larger set of run products were measured by the flank method in order to test the sensitivity and accuracy of the method for very small variations of bulk  $\Sigma\text{Fe}$  (wt%) and  $\text{Fe}^{3+}/\Sigma\text{Fe}$  along diffusion profiles.

High pressure high temperature diffusion experiments using a multi anvil apparatus were carried out on (Mg,Fe)O crystals with the aim to study the variation of ferric iron and hydrogen in (Mg,Fe)O as a function of pressure, temperature, oxygen fugacity and water fugacity. Experiments were performed by Kazuhiko Otsuka under the supervision of Prof. Shun Karato at Yale University (USA) as part of a Ph.D project. Samples were then kindly made available for flank method measurements. Experiments were performed in the pressure range of 3-27 GPa using tungsten carbide anvils and a temperature range of 1300-1400 K. (Mg<sub>x</sub>,Fe<sub>1-x</sub>)O single crystals were initially equilibrated in a gas mixing furnace in order to obtain a wide range of  $\text{Fe}^{3+}/\Sigma\text{Fe}$ . Subsequently the equilibrated crystals were loaded as diffusion couples with MgO single crystals into a metal capsule. The two crystals were surrounded by (Mg<sub>x</sub>,Fe<sub>1-x</sub>)O powder of the same composition as the equilibrated single crystals.

For the three samples of interest, experiments were conducted at pressures between 5 and 8 GPa and a temperature of 1400 °C (Tab. 4.3). The oxygen fugacity was controlled during the experiments using a Mo-MoO<sub>2</sub> buffer. Mo foil was placed between the sample and the AuPd

#### 4. Results (2): Flank Method Applications

capsule in the assembly, and metal oxide powder was placed next to the metal foil to buffer the oxygen fugacity.

**Table 4.3** – Experimental conditions for diffusion run products

Run	Material	Composition	Pressure (GPa)	Temperature (°C)	Capsule
K685	(Mg,Fe)O pairs	Mg# 100/80	5	1400	AuPd
K688	(Mg,Fe)O pairs	Mg# 100/80	8	1400	AuPd
K700	(Mg,Fe)O pairs	Mg# 100/80	5	1400	AuPd

Mg-Fe diffusion profiles were measured by electron microprobe for quantitative analysis simultaneously with flank method measurements. Starting material and experimental conditions for the synthetic (Mg,Fe)O are reported in Table 4.3.

Figure 4.6 reports the three measured samples K688, K700 and K685. Areas characterized by different intensities of grey correspond to different amounts of Fe in the mineral composition of (Mg,Fe)O. Dark-grey regions are Fe-depleted (ideally of MgO composition), whereas light grey regions are Fe-rich. Mg-Fe diffusion profiles were carefully located to cross the boundary of crystals of different compositions (Tab. 4.4) where diffusion took place (Fig. 4.6).

$\text{Fe}^{3+}/\sum\text{Fe}$  ratios were determined using equation (8) (see § 3.3) and results are reported in Table 4.4.

4. Results (2): Flank Method Applications

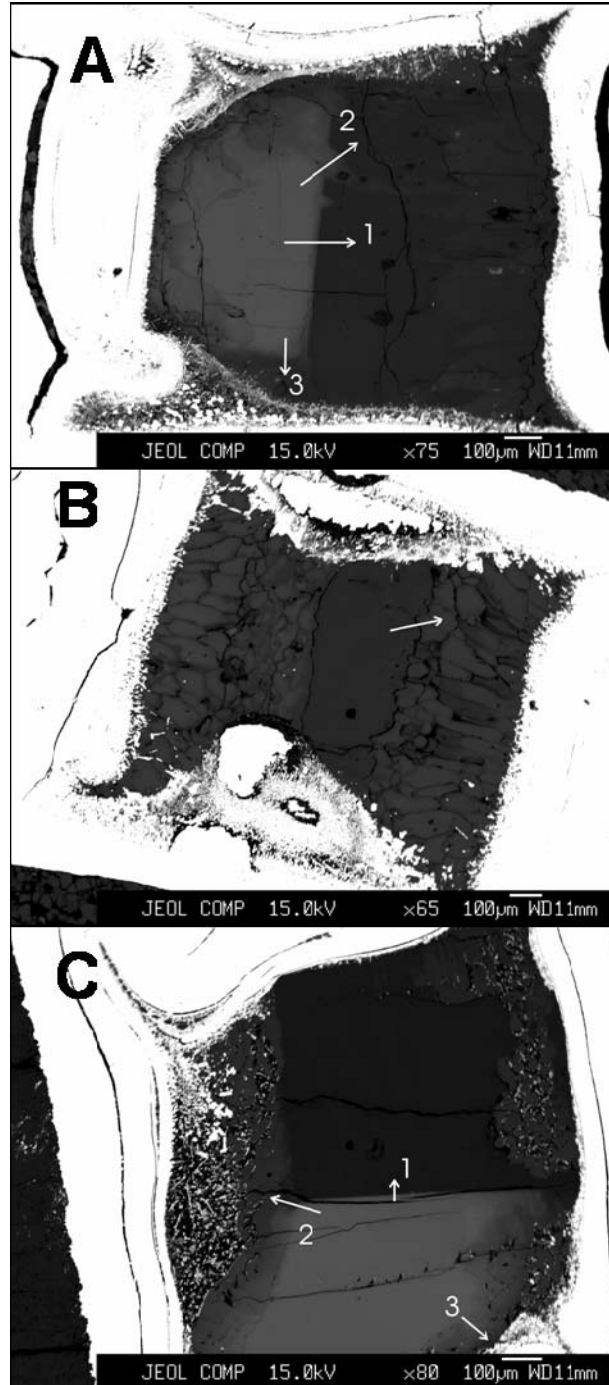


**Fig. 4.6** – Back Scattered electron images of (Mg,Fe)O diffusion couples from the electron microprobe: A) K688, B) K700, C)K685. The light grey regions represent the FeO-rich crystals, whereas the dark grey regions represent the MgO-rich crystals. Measurement profiles are indicated by white lines.

#### 4. Results (2): Flank Method Applications

**Table 4.4** – Diffusion profiles measured by electron microprobe for synthetic (Mg,Fe)O from Otsuka et al. (not published)

<b>Diffusion profile</b>	<b>Chemical variation</b>	<b>L<math>\beta</math>/L<math>\alpha</math> range</b>	<b>Fe<sup>3+</sup>/<math>\Sigma</math>Fe range</b>	<b>Fe<sup>3+</sup>/<math>\Sigma</math>Fe average</b>
<b>K685_1</b>	(Mg <sub>80</sub> Fe <sub>20</sub> )O → MgO	1.04-0.80	0.08-0.14	0.13(9)
<b>K685_2</b>	(Mg <sub>94</sub> Fe <sub>6</sub> )O → (Mg <sub>80</sub> Fe <sub>20</sub> )O	0.85-1.05	0.06-0.13	0.09(2)
<b>K685_3</b>	(Mg <sub>87</sub> Fe <sub>13</sub> )O → (Mg <sub>78</sub> Fe <sub>22</sub> )O	0.89-1.05	0.09-0.17	0.13(2)
<b>K688_1</b>	(Mg <sub>80</sub> Fe <sub>20</sub> )O → MgO	1.01-0.61	0.01-0.14	0.06(4)
<b>K688_2</b>	(Mg <sub>80</sub> Fe <sub>20</sub> )O → MgO	1.03-0.67	0.02-0.34	0.27(9)
<b>K688_3 powder</b>	(Mg <sub>85</sub> Fe <sub>15</sub> )O → MgO	0.95-0.81	0.001-0.106	0.07(3)
<b>K700_1</b>	(Mg <sub>95</sub> Fe <sub>5</sub> )O → MgO	0.612-1.02	Not determined*	
<b>K700_2</b>	(Mg <sub>92</sub> Fe <sub>8</sub> )O → MgO	0.66-1.04	Not determined*	
<b>K700_3</b>	(Mg <sub>83</sub> Fe <sub>17</sub> )O → MgO	0.996-0.81	0.03-0.15	0.08(4)

\*It was not possible to determine Fe<sup>3+</sup>/ $\Sigma$ Fe for sample K700\_1 and K700\_2 due to the low Fe concentration

#### 4. Results (2): Flank Method Applications

The behavior of the  $L\beta/L\alpha$  ratio was studied as a function of Fe bulk composition (wt%) (Fig.4.7a,b) and of  $Fe^{2+}$  (wt%) (Fig.4.8a,b) for nearly all of the diffusion profiles. Measurements were performed using a 2 to 3  $\mu\text{m}$  step between measurements. By looking at Figure 4.7a,b it can be noticed that  $L\beta/L\alpha$  measurements are not sensitive for bulk Fe concentrations lower than  $\sim 3$  wt%. As a consequence, flank method measurements for Fe compositions lower than this value do not follow the theoretical trend described by synthetic (Mg,Fe)O from the present study. In fact, for almost all the diffusion profiles, the measured  $L\beta/L\alpha$  ratio drops rapidly from 1.3 to 0.6 counts per seconds, and then at about 2 wt% starts increasing as a function of  $\Sigma\text{Fe}$  (wt%) in agreement with the theoretical trend described by synthetic (Mg,Fe)O from the present study. Only few data points do not plot along the curve (Fig. 4.7a).

An anomalous behavior of  $L\beta/L\alpha$  as a function of  $\Sigma\text{Fe}$  (wt%) was obtained for the diffusion profile K688\_2. Results do not follow the trend described by the other diffusion profiles (Fig. 4.7b), which is also evident as a function of  $Fe^{2+}$  (wt%) (Fig. 4.8b). One possible explanation of this anomalous behavior is the occurrence of different oxidation processes in the proximity of the capsule, possibly due to the interaction of MgO-FeO with the Mo-MoO<sub>2</sub> buffer. In fact the K688\_2 diffusion profile shows complexities in the variation of composition which has not been observed for any other diffusion profiles, associated with significantly higher  $Fe^{3+}/\Sigma\text{Fe}$  values compared to all other diffusion profiles.

4. Results (2): Flank Method Applications

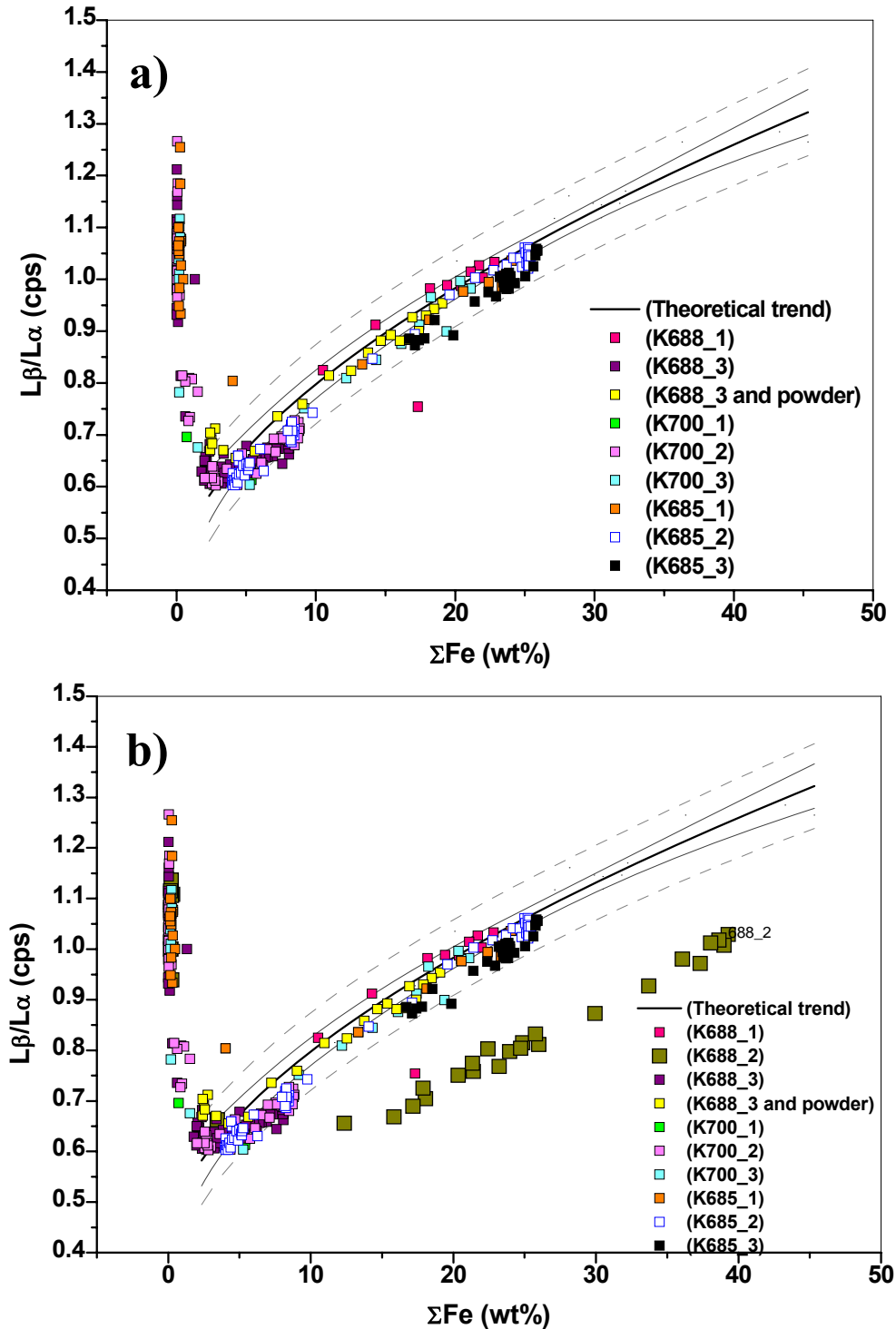


**Fig. 4.7** – a)  $L\beta/L\alpha$  variation as a function of  $\Sigma\text{Fe}$  (wt%) for synthetic (Mg,Fe)O crystals from Otsuka et al. (not published) compared to b) K688\_2 diffusion profile (in olive green) compared to all other diffusion profiles. Solid grey lines are the upper and lower 95% confidence limits, whereas the dashed light grey lines are the upper and lower 95% prediction limits respectively. Confidence and prediction limits refer to the theoretical trend described by (Mg,Fe)O from the present work.

4. Results (2): Flank Method Applications

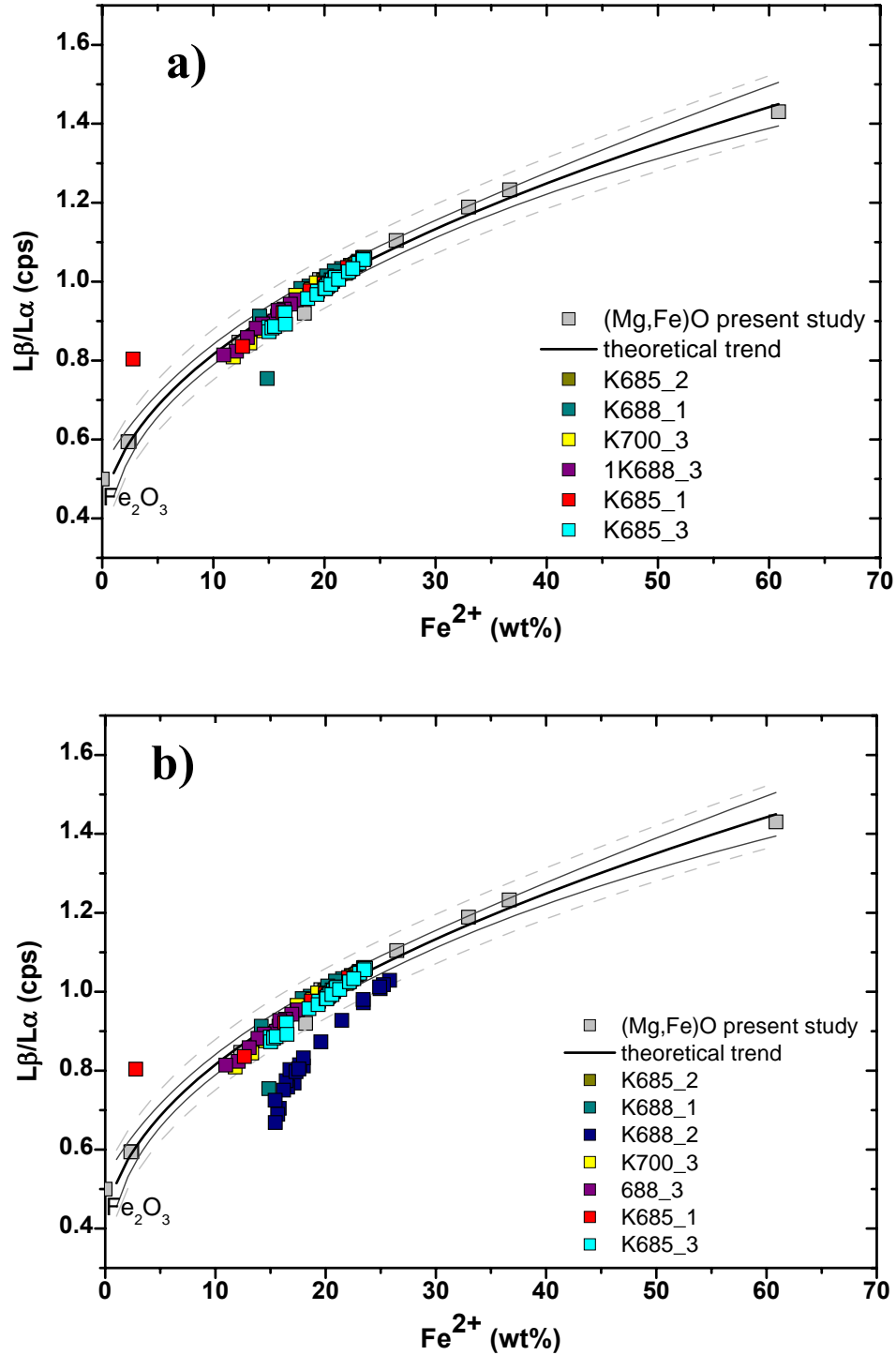


**Fig. 4.8** – a)  $L\beta/L\alpha$  variation as a function of  $Fe^{2+}$  (wt%) for synthetic (Mg,Fe)O crystals from Otsuka et al. (not published) compared to b) K688\_2 diffusion profile (in dark blue). Solid grey lines are the upper and lower 95% confidence limits, whereas the dashed light grey lines are the upper and lower 95% prediction limits.

#### 4. Results (2): Flank Method Applications

Sample K688 was additionally investigated by Mössbauer spectroscopy with the aim to:

- determine the bulk  $\text{Fe}^{3+}/\sum\text{Fe}$  ratio for the  $(\text{Mg}_{80}\text{Fe}_{20})\text{O}$  single crystal;
- confirm the measurement near the diffusion profile between  $(\text{Mg}_{80}\text{Fe}_{20})\text{O}$  single crystal and MgO single crystal (K688\_1).

The two selected areas chosen for Mössbauer measurements are shown in Figure 4.9 and Mössbauer spectra are shown in Figure 4.10. A summary of results is reported in Table 4.5.

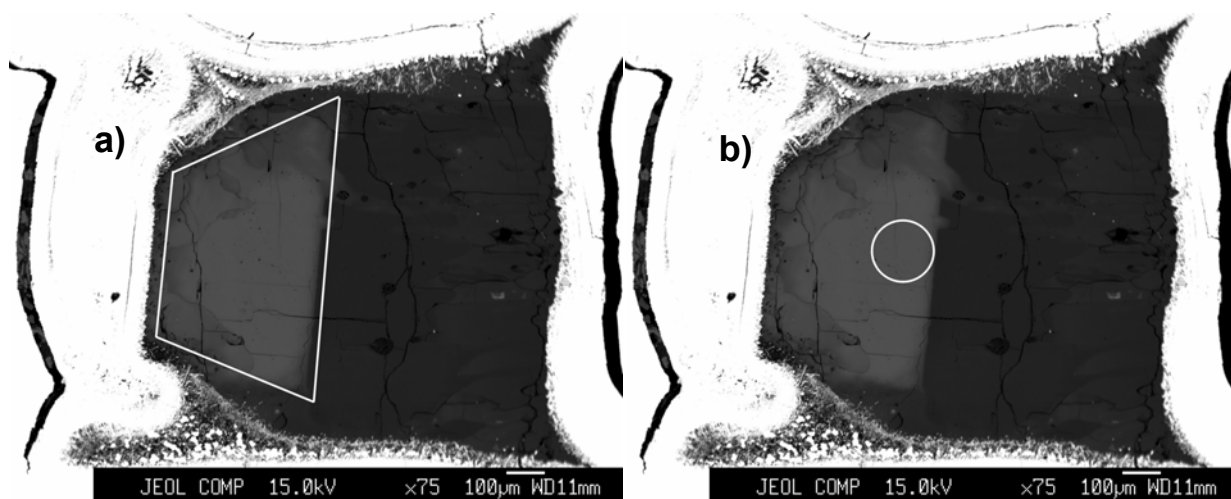


**Fig. 4.9** - Back Scattered electron images from the electron microprobe for sample K688 with areas measured by Mössbauer spectroscopy indicated in white: a) bulk measurement on the entire  $(\text{Mg}_{80}\text{Fe}_{20})\text{O}$  single crystal ( $300 \times 700 \mu\text{m}$ ) and b) *in situ* measurement on a  $150 \mu\text{m}$  circular area near the  $(\text{Mg}_{80}\text{Fe}_{20})\text{O}$ -MgO boundary.

#### 4. Results (2): Flank Method Applications

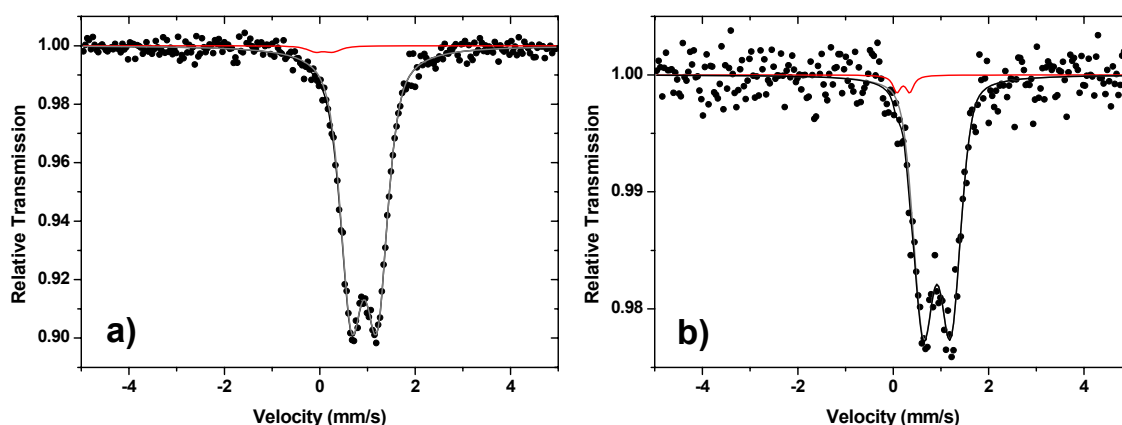


**Fig. 4.10** – Mössbauer spectra collected for the regions shown in Fig. 4.9 for sample K688: a) bulk measurement on the entire  $(\text{Mg}_{80}\text{Fe}_{20})\text{O}$  single crystal and b) *in situ* measurement on a spot with 150  $\mu\text{m}$  diameter near the  $(\text{Mg}_{80}\text{Fe}_{20})\text{O}$ -MgO boundary. The latter spectrum gives a lower signal to noise ratio due to the smaller solid angle for  $\gamma$  rays during the measurement. Dots correspond to experimental data, black lines to fitted curves, grey lines to  $\text{Fe}^{2+}$  doublets (representing the dominant contribution) and red lines to  $\text{Fe}^{3+}$  doublets.

**Table 4.5** – Comparison between  $\text{Fe}^{3+}/\sum\text{Fe}$  determined by Mössbauer spectroscopy and flank method

Diffusion profile	Dimension	Composition	$\text{Fe}^{3+}/\sum\text{Fe}$	$\text{Fe}^{3+}/\sum\text{Fe}^*$
<b>K688</b>	Bulk (300x700 $\mu\text{m}$ )	$(\text{Mg}_{80}\text{Fe}_{20})\text{O}$	0.02(1)	
<b>K688_1</b>	150 $\mu\text{m}$ diameter	$(\text{Mg}_{80}\text{Fe}_{20})\text{O} \rightarrow \text{MgO}$	0.03(3)	0.06(4)

\* average of  $\text{Fe}^{3+}/\sum\text{Fe}$  measurements by flank method along the K688\_1 diffusion profile

Data collected for the bulk  $(\text{Mg}_{80}\text{Fe}_{20})\text{O}$  single crystal are similar to the data collected for a 150  $\mu\text{m}$  diameter spot on the crystal investigated near the diffusion couple boundary, giving a  $\text{Fe}^{3+}/\sum\text{Fe}$  value of 2%. Flank method results obtained for the K688\_1 diffusion profile give  $\text{Fe}^{3+}/\sum\text{Fe}$  values ranging from 0.01 to 0.14, with an average of  $0.06 \pm 0.04$  (Tab. 4.6). Therefore flank method measurements and Mössbauer measurements are in agreement within experimental error. It has therefore been demonstrated that the flank method is able to measure  $\text{Fe}^{3+}/\sum\text{Fe}$  along the diffusion profile with micron scale resolution, compared to Mössbauer spectroscopy which can only give a bulk measurement averaged over variations in oxidation state that may occur along the diffusion profile.

4. Results (2): Flank Method Applications

**Table 4.6-** Fe<sup>3+</sup>/ΣFe measured along the K688\_1 and K688\_2 diffusion profiles

Sample	K688_1		K688_2		
	Measurements	ΣFe (wt%)*	Fe <sup>3+</sup> /ΣFe**	ΣFe (wt%)*	Fe <sup>3+</sup> /ΣFe**
#1		23.39	0.11	39.27	0.34
#2		22.83	0.06	38.99	0.36
#3		21.98	0.08	38.63	0.35
#4		21.72	0.04	38.05	0.35
#5		21.11	0.04	37.31	0.37
#6		20.39	0.07	36.06	0.35
#7		19.42	0.04	33.72	0.36
#8		18.19	0.02	29.93	0.35
#9		17.32	0.14	25.99	0.31
#10		14.29	0.01	23.22	0.26
#11		-	-	21.39	0.23
#12		-	-	21.34	0.23
#13		-	-	22.42	0.25
#14		-	-	23.96	0.28
#15		-	-	24.87	0.29
#16		-	-	25.75	0.30
#17		-	-	24.73	0.29
#18		-	-	20.34	0.20
#19		-	-	18.04	0.12
#20		-	-	17.89	0.14
#21		-	-	17.169	0.09
#22		-	-	15.83	0.03
#23		-	-	22.42	0.25
#24		-	-	23.96	0.28
<b>Average</b>			<b>0.06</b>		<b>0.27</b>
<b>Standard Deviation</b>			<b>0.04</b>		<b>0.1</b>

\* Fe bulk composition variation along the diffusion profile

\*\* Fe<sup>3+</sup>/ΣFe determined by flank method

#### 4. Results (2): Flank Method Applications

The variation of  $\text{Fe}^{2+}$  and  $\text{Fe}^{3+}$  (wt%) as determined using equation (8) (§ 3.2), as well as the variation of  $L\beta/L\alpha$  ratios, were studied as a function of  $\Sigma\text{Fe}$  (wt%) along the diffusion profile. As an example, results obtained for the K685\_1 diffusion profile were chosen and plotted in Fig 4.11.  $\text{Fe}^{2+}$  and  $\text{Fe}^{3+}$  concentrations (wt%) show a negative correlation as a function of distance in  $\mu\text{m}$  (Fig. 4.11b and Fig. 4.11d), in accordance with the trend described for the variation of Fe bulk composition along the diffusion profile (Fig. 4.11a). The variation of  $\text{Fe}^{3+}$  (wt%) is smaller than the one observed for  $\text{Fe}^{2+}$  (wt%), due to the low  $\text{Fe}^{3+}$  content (maximum 3.5 wt%), compared to the  $\text{Fe}^{2+}$  (wt%) content (maximum 24 wt%).

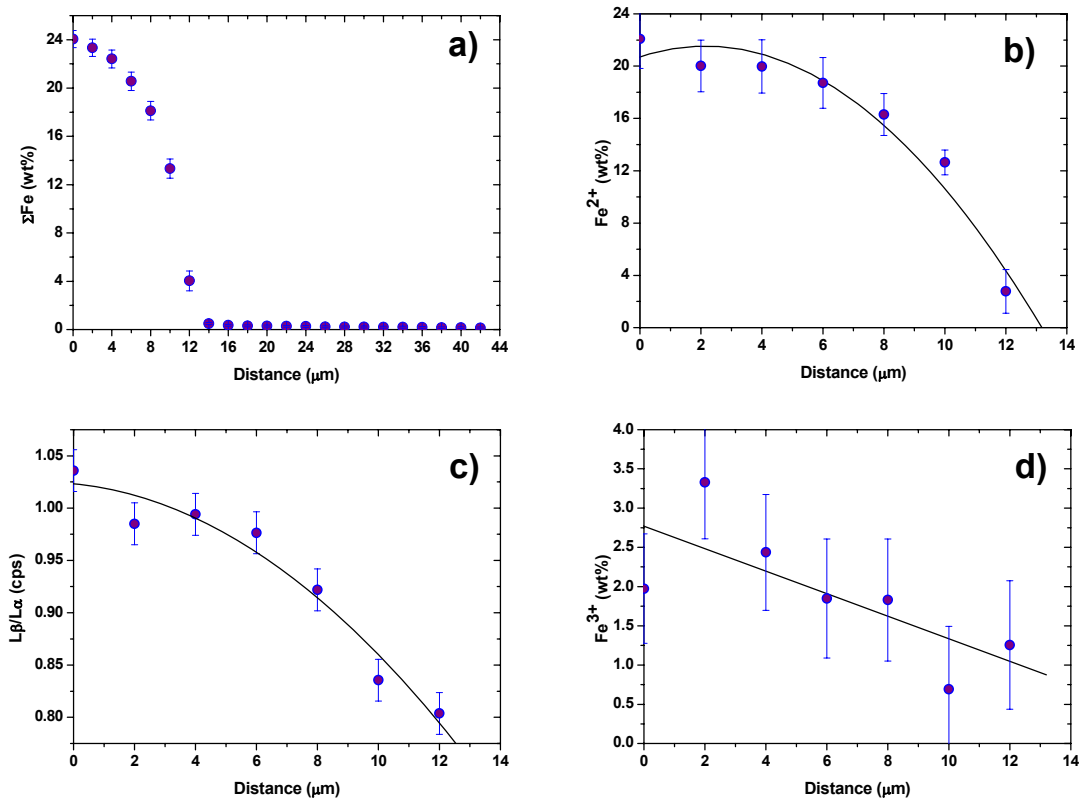


**Fig. 4.11** - Variation of a)  $\Sigma\text{Fe}$  (wt%), b)  $\text{Fe}^{2+}$  (wt%) c)  $L\beta/L\alpha$  (cps) and d)  $\text{Fe}^{3+}$  (wt%) vs. measurement position, reported as distance in  $\mu\text{m}$  along the diffusion profile. Data refer to sample K685\_1. Error bars for the  $\Sigma\text{Fe}$  (wt%) were estimated from the EMP analyses as  $[A+B(\text{wt}\% \text{ oxide})]$ , where A is equal to 0.07 and B equal to 0.005 (Canil and O'Neill, 1996). Assuming higher error as  $\Sigma\text{Fe}$  (wt%) decreases, error bars are increased to 0.02 for subsequent measurements. In b) the  $L\beta/L\alpha$  standard deviation is fixed to 0.02, which corresponds to the reproducibility of flank method measurements. Error bars for c), and d) are propagated using equation (8) (see § 3.3).

## 4. Results (2): Flank Method Applications

### 4.1.3 Flank Method applied to synthetic (Mg,Fe)O at 24 GPa

Two (Mg,Fe)O samples were chosen from a larger number of run products synthesized from studies on the diamond/carbonate stability field as function of the oxygen fugacity in lower mantle assemblages. Experiments were conducted by Vincenzo Stagno (Ph.D candidate at Bayerisches Geoinstitut) and kindly supplied for flank method measurements. Experiments were performed at 24 GPa and 1500°C using a Hymag Press at Bayerisches Geoinstitut. More detailed experimental conditions and Fe bulk composition are reported in Table 4.7.

Mixtures of MgCO<sub>3</sub>, (Mg<sub>0.75</sub>Fe<sub>0.25</sub>)O and C were loaded into a graphite capsule, which was subsequently covered by Re foil. The oxygen fugacity during the experiment was measured using the Ir-IrFe alloy. The  $\log fO_2$  was determined to be -4.8 relative to the Fayalite-Magnetite-Quartz buffer (FMQ) (Stagno and Frost, in preparation). Run products were then mounted in epoxy, polished and carbon coated for electron microprobe analysis.

Flank method measurements were performed together with major element analysis according to the procedure described in §2.6.1. Fe<sup>2+</sup> (wt%) was measured using equation (9) reported in §3.3.1. Results are shown in Figure 4.12. Fe<sup>3+</sup>/ΣFe was calculated to be 4.1 and 4.9%, and data are in excellent agreement with the theoretical trend described by synthetic (Mg,Fe)O at 15 GPa from the present study. Such reduced Fe<sup>3+</sup>/ΣFe ratios are fully consistent with the oxygen fugacity conditions measured, which are slightly above the IW buffer. Flank method measurements performed for (Mg,Fe)O synthesized at 15 and 24 GPa, as well as natural samples crystallized at pressures likely higher than 24 GPa (transition zone-lower mantle boundary), are consistent with the calibration curve described by equation (9) (see § 3.3.1). Therefore it is possible to conclude that pressure does not affect the Lβ/Lα ratio evolution of (Mg,Fe)O with Fe bulk composition, and data fall on the theoretical trend.

**Table 4.7** – Experimental conditions, Fe bulk composition and Fe<sup>3+</sup>/ΣFe determined by the flank method

Run product	Pressure (GPa)	Temperature (°C)	ΣFe (wt%)	Fe <sup>3+</sup> /ΣFe
H2887	24	1550	22.06	0.049
H2946	24	1500	20.13	0.041

#### 4. Results (2): Flank Method Applications

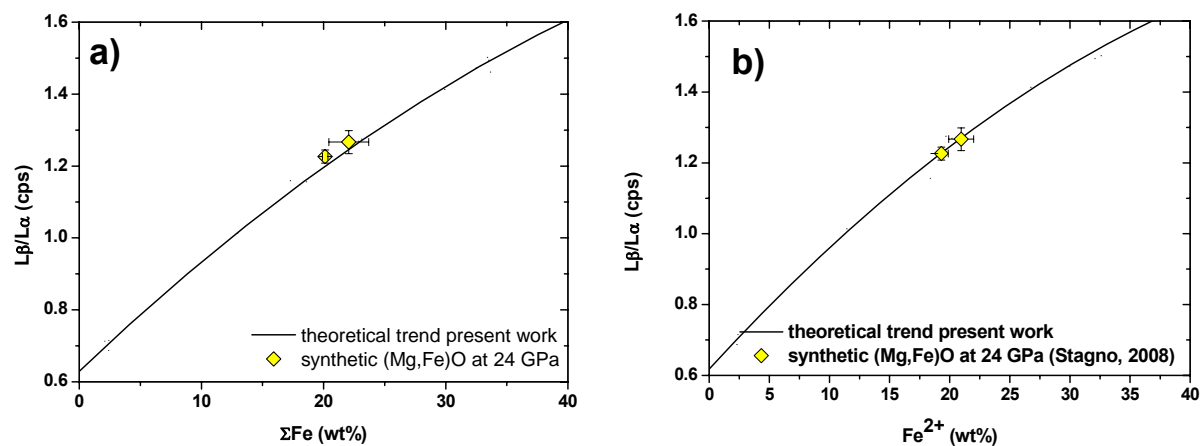


**Fig. 4.12** –  $L\beta/L\alpha$  ratios versus  $\Sigma$  Fe (a) and  $Fe^{2+}$  (b) for synthetic (Mg,Fe)O kindly provided by Vincenzo Stagno. Results for flank method measurements at 24 GPa (yellow diamonds) are consistent with the theoretical line described by synthetic (Mg,Fe)O from this study at 15 GPa (black line). Error bars for  $Fe^{2+}$  (wt%) are propagated using equation (9) (see § 3.3.1).

## 4.2 Natural (Mg,Fe)O diamond inclusions

After obtaining the calibration of the flank method for synthetic (Mg,Fe)O ferropericlase and exploring possible applications for synthetic samples, the calibration was applied to determine  $Fe^{3+}/\Sigma Fe$  by electron microprobe on natural (Mg,Fe)O from lower mantle diamonds, with the aim to provide a high resolution method able to investigate the oxygen fugacity conditions at lower mantle depth. Three sets of ferropericlase inclusions from ultra deep diamonds selected worldwide were analyzed by flank method in order to check the reliability of the calibration curve for natural samples. The data set consists of eighteen (Mg,Fe)O ferropericlase samples: four inclusions from Juina, Brazil (supplied by Felix Kaminsky), two inclusions from Machado River, Brazil (supplied by Galina Bulanova) and twelve inclusions from Ororoo, Australia (supplied by Ralf Tappert) (Fig. 4.13). Inclusions are between 10 and 50  $\mu m$  in size, therefore they are suitable to perform flank method measurements to determine  $Fe^{3+}/\Sigma Fe$ .

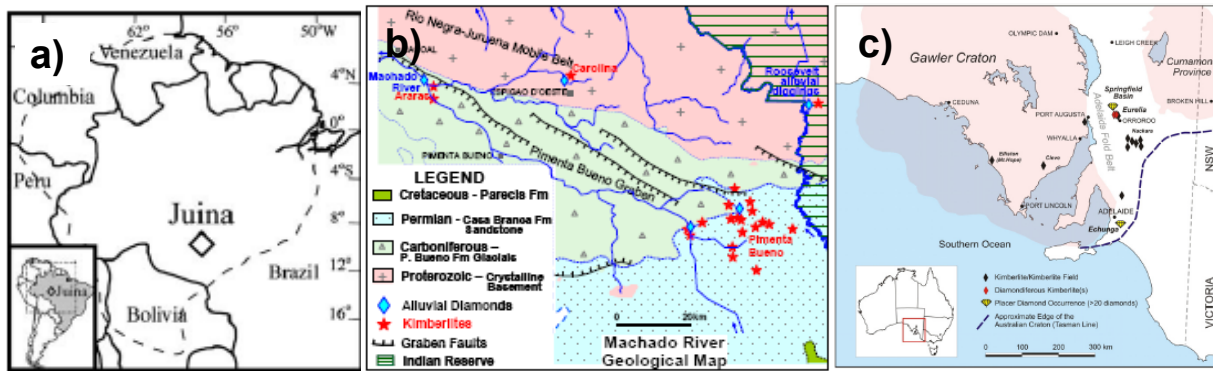


**Fig. 4.13** – a) Location of Juina area in Brazil: dashed line indicates approximate outline of the Amazonian craton (Tassinari and Macambira, 1999); b) Geological map of Machado River territory (Brazil); c) Location of diamond and kimberlite occurrences in South Australia. *From Hayman et al. (2005), Bulanova et al. (2008) and Tappert et al. (2008), respectively.*

#### *4. Results (2): Flank Method Applications*

##### *Juina area, Mato Grosso (Brazil)*

The Juina area (Mato Grosso State, Brazil) is a major diamond mining area in Brazil (Fig. 4.13a). It is located in the Amazonian Craton, and it contains at least 26 kimberlite pipes. Two of the kimberlitic pipes have been dated at 92-95 Ma (U/Pb dating of zircons from kimberlitic breccia) (Heaman et al., 1998). Kimberlites are located near the southwestern margin of the Amazonian Craton and are emplaced in the Permo-Carboniferous sedimentary rocks of the Fazenda da Casa Blanca Formation, while some intrude the older Rio Negro-Juruena Province (Tassinari and Macambira 1999). Some of kimberlites are sub-economic with up to 0.5 carats per tons diamond grade. In the late 1980s-early 1990s 5 to 6 million carats were produced each year. Many of the diamonds recovered were larger than 100-200 carats. All diamond production has been from recent alluvial and colluvial deposits. Examination of the syngenetic mineral inclusions in the Juina diamonds reveals that they are dominated by phases recognized as ultra-deep paragenesis. The identified phases are (Mg,Fe)O ferropericase, MgSiO<sub>3</sub>, CaSiO<sub>3</sub>, magnetite, pyrrhotite, (Mg,Fe)<sub>2</sub>SiO<sub>4</sub>, TAPP, SiO<sub>2</sub>, garnet, titanite and native Ni. MgSiO<sub>3</sub> and CaSiO<sub>3</sub> inclusions have been interpreted to represent pressure-reverted former perovskite phases, and will be subsequently referred to as Mg,Si-perovskite and Ca,Si-perovskite, respectively.

Ferropericase is commonly the most abundant mineral inclusion recovered from Juina diamonds (Hayman et al., 2005). All (Mg,Fe)O inclusions except for one appear to occur always in association with Mg,Si- perovskite, Ca,Si- perovskite, (Mg,Fe)<sub>2</sub>SiO<sub>4</sub> and TAPP. The Mg number is widely variable from 0.45 to 0.89 (average 0.68, Hayman et al., 2005). When ferropericase is associated with TAPP and (Mg,Fe)<sub>2</sub>SiO<sub>4</sub>, the Mg number tends to be richer in MgO. Fe-Ni alloy blebs (< 2 µm in size) were found on ferropericase surfaces in two diamonds, whereas another one was found locally surrounded by secondary magnetite-magnesioferrite.

Four (Mg,Fe)O inclusions were extracted by crushing the host diamonds. Inclusions were very small in size, between 20 and 50 µm.

#### *4. Results (2): Flank Method Applications*

##### *Machado River (Brazil)*

Two of the ferropericlasite inclusions measured by the flank method were recovered from Machado River alluvial diamonds, located in Rondonia (Brazil), downstream from the diamondiferous Pimenta Bueno and Carolina Kimberlites (Fig.4.13b). The nearby Araras kimberlites are barren. The occurrence lies within the 1.55-1.8 Ga Rio Negra-Juruena Mobile Belt on the southern margin of the Amazonian Craton, some 200 km west of the Juina ultradeep diamond field.

Diamonds recovered from this area belong to three different genetic groups: ultradeep, eclogitic and peridotitic. The ones of interest for the present study are those of ultradeep origin, occurring with a frequency of 35% of the total diamonds found. Such diamonds are nitrogen free or show very low amounts (Bulanova et al., 2008). Mineral inclusions of ultradeep paragenesis at Machado River are represented by Mg,Si- and Ca,Si perovskites, (Mg,Fe)O ferropericlasite, majorite and low-Ni sulphides. The most common inclusion (in 6 diamonds) is a Fe-Al-Si mineral, possibly (AlSiO<sub>3</sub>)OH - phase egg of lower mantle derivation. When (Mg,Fe)O and Mg,Si-perovskite are coexisting, the NiO content is higher in (Mg,Fe)O (commonly 1.20 wt%), whereas in perovskite is almost negligible (less than 0.03 wt. %), indicating Ni partitioning between (Mg,Fe)O and Mg,Si perovskite inclusions. Ferropericlasite Mg numbers are similar to those observed for Kankan diamond inclusions (Fig. 4.14).

Diamonds were transparent and about 0.5 mm in size (0.5 x 0.3 x 0.2 mm). Diamonds were polished to expose the ferropericlasite inclusions for electron microprobe measurements (Fig. 4.15a,b). Inclusions were 15 and 50 µm in size.

#### 4. Results (2): Flank Method Applications

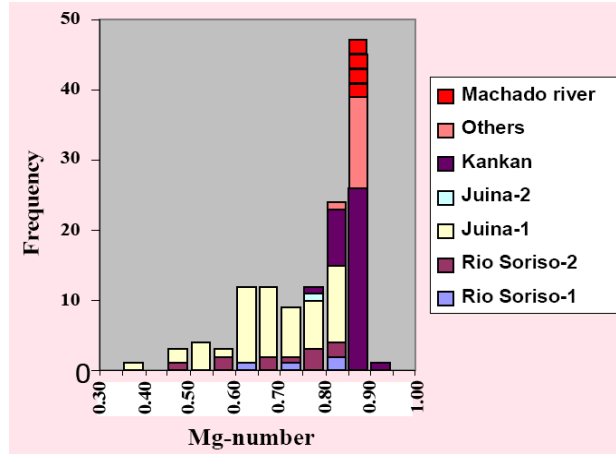


**Fig. 4.14** – Machado (Mg,Fe)O diamond inclusions. Mg# compared to worldwide data. *From Bulanova et al. (2008)*

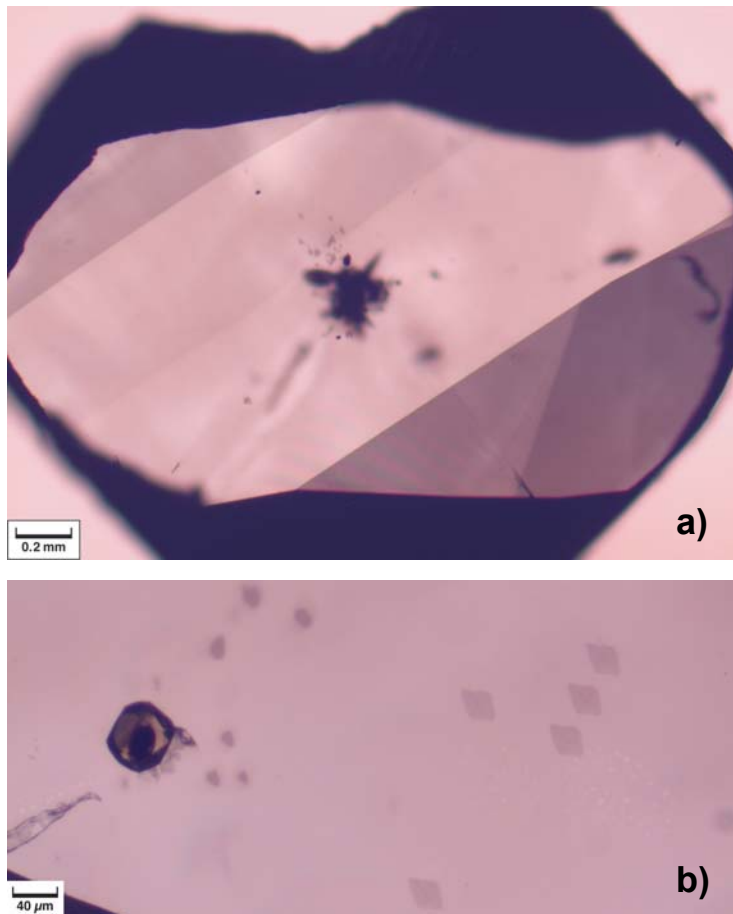


**Fig. 4.15** – a) Ultra deep origin diamond from Machado River (Brazil) with fluid inclusions visible at the centre of the stone; b) (Mg,Fe)O ferropericlase inclusion surrounded by a family of unidentified octahedral inclusions.

## 4. Results (2): Flank Method Applications

### *Eurelia and Springfield Basin (Ororoo, Australia)*

A total amount of twelve (Mg,Fe)O ferropericlasite inclusions were recovered by crushing host diamonds from Jurassic kimberlites occurring at Eurelia and the Springfield Basin (Ororoo, Southern Australia) (Fig. 4.13c). Of the 43 diamonds recovered from three different Jurassic kimberlites at Eurelia, one diamond (FBS5–11) from the K7 kimberlite dike was found to contain 6 coexisting inclusions of (Mg,Fe)O ferropericlasite and one Mg,Si-perovskite. The coexistence of ferropericlasite and Mg,Si-perovskite confirms a lower mantle origin of the diamonds, as at pressures lower than ~24.5 GPa the two phases would react to form an olivine polymorph (Mg<sub>2</sub>SiO<sub>4</sub>) (Ito and Takahashi, 1989). An additional inclusion-bearing diamond (FBS5–12), also recovered from the K7 kimberlite, was found to contain a single inclusion of olivine composition. The remaining 41 diamonds were inclusion free.

Two diamonds from the Springfield Basin contained ferropericlasite inclusions. In one diamond, (Mg,Fe)O ferropericlasite was accompanied by an inclusion of olivine composition. The nitrogen characteristics of the two host diamonds (low N content, high N aggregation) are similar to those of the ferropericlasite-bearing diamond from Eurelia (Tappert et al., 2008). This suggests a sublithospheric origin (even in absence of Mg,Si-perovskite inclusions) for those diamonds and reinforces the similarities between the two diamond sources. Twelve (Mg,Fe)O inclusions, recovered by crushing diamonds, were all between 20 and 50 µm in size. Diamonds were opaque. Therefore, it was not possible to map the position of inclusions into the diamonds before crushing.

### **4.2.1 Sample preparation**

The six inclusions from Mato Grosso (Brazil) and the twelve inclusions from Ororoo (Australia) were mounted in epoxy to perform major element analysis. Each sample was then mounted in brass rings of 6 mm diameter and carbon coated for electron microprobe measurements.

The two ferropericlasite inclusions from Machado River (Brazil) were measured directly from the diamonds, which were polished in order to expose the inclusions to the electron beam. The two diamonds were mounted on conductive vacuum plasticine that is stable at electron microprobe conditions. Diamonds were mounted in a way that the inclusion surfaces were exactly

#### 4. Results (2): Flank Method Applications

perpendicular to the electron beam. To ensure adequate electron conductivity during the measurements, the diamond surface was carbon coated. After coating, the two diamonds were connected by a narrow path of carbon paste on the side of the diamonds. The carbon path was extended until the end of the holder from both sides to ensure that the entire mount would be conductive for electrons.

##### 4.2.2 Flank Method and Major element analysis results for natural (Mg,Fe)O

Since the flank method shows high sensitivity to variations in the chemical composition (in the presence of extra phases) through the  $L\beta/L\alpha$  ratio as a function of  $Fe^{2+}$  (wt%), (Mg,Fe)O ferropericline inclusions were first examined to test for phase homogeneity. Flank method results for nearly all the natural (Mg,Fe)O inclusions show good agreement with the theoretical trend described by the synthetic samples as a function of  $\Sigma Fe$  (wt%), and more importantly as a function of  $Fe^{2+}$  (wt%) (Fig. 4.16a and 4.16b), which confirms high phase homogeneity for most of the samples. Only one of the Machado River inclusions plots slightly below the theoretical line (Fig. 4.16a), possibly suggesting the presence of additional phase(s), which may be most likely due to exsolution of magnesioferrite from the (Mg,Fe)O crystals. Since inclusions are all less than 50  $\mu m$  in diameter, the  $Fe^{3+}/\Sigma Fe$  ratio was determined only using the flank method calibration. The high spatial resolution offered by the electron micro beam made it possible to measure a sample of 15  $\mu m$  in diameter (P11 sample, Machado River, Brazil).  $Fe^{3+}/\Sigma Fe$  ratios of (Mg,Fe)O inclusions from Juina area and Machado River (Brazil) were determined using equation (8) (see § 3.3), whereas  $Fe^{3+}/\Sigma Fe$  ratios of (Mg,Fe)O inclusions from Eurelia kimberlite and Springfield Basin (Australia) were determined using equation (9) (see §3.3.1).

4. Results (2): Flank Method Applications

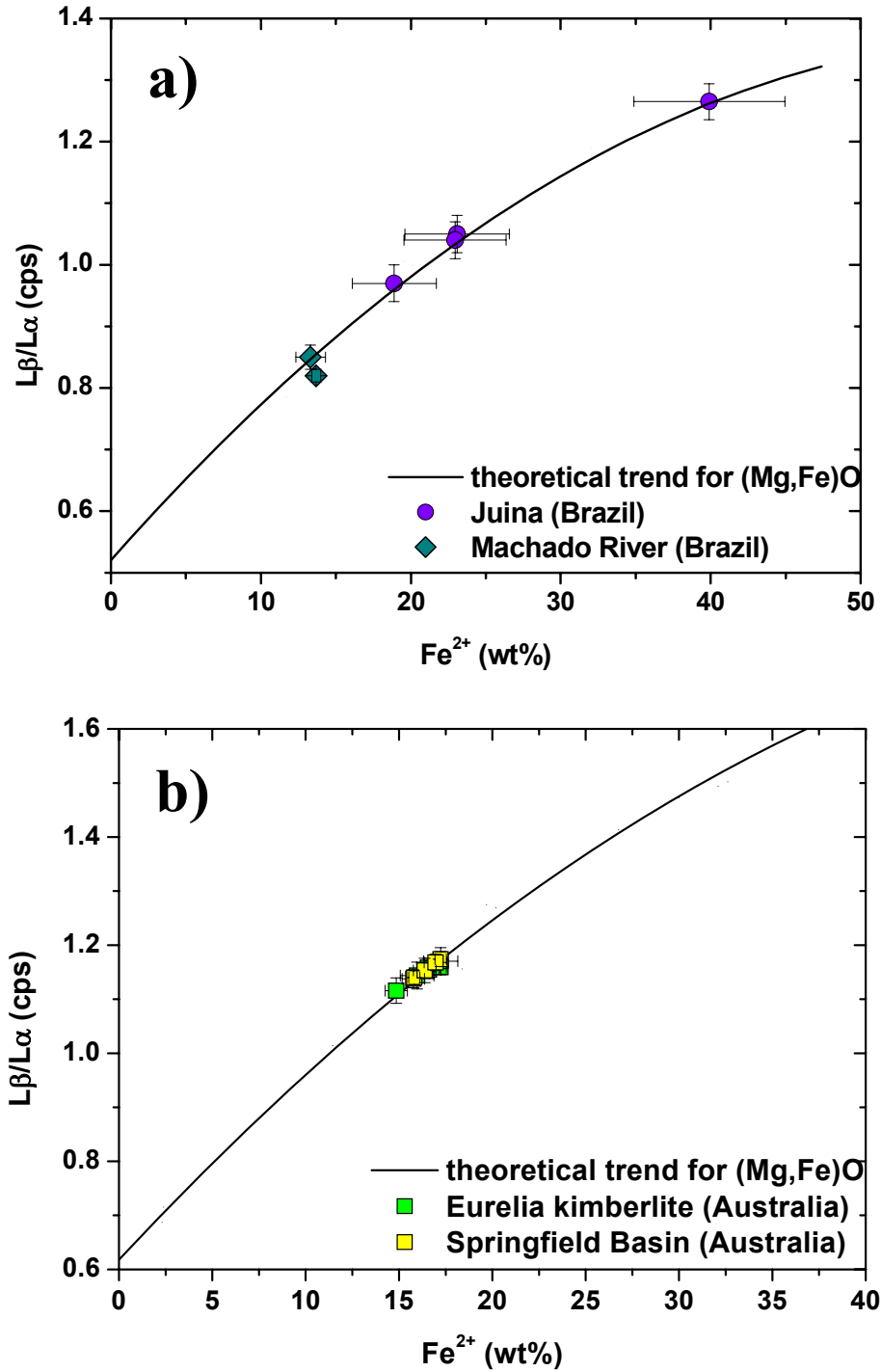


**Fig. 4.16** –  $L\beta/L\alpha$  ratios versus  $Fe^{2+}$  for (Mg,Fe)O. Natural (Mg,Fe)O inclusions from Brazil (a) and from Australia (b) show good agreement with the theoretical line described by synthetic (Mg,Fe)O (black line). Error bars for  $Fe^{2+}$  (wt%) in a) are propagated using equation (8) (see §3.3); whereas error bars for  $Fe^{2+}$  (wt%) in b) are propagated using equation (9) (see § 3.3.1).

#### 4. Results (2): Flank Method Applications

Major element analysis determined by Electron MicroProbe for the natural (Mg,Fe)O inclusions is reported in Tables 4.8 and 4.9. For all inclusions, the FeO content (wt%) ranges from 19 to 50. However, a comparison between inclusions from different localities shows that (Mg,Fe)O recovered from Machado River (Brazil), Eurelia and the Springfield Basin (Australia) are of similar composition, not showing large variations in the Fe content; whereas inclusions from Juina show FeO contents (wt%) variable within a greater range (28-50 wt%).

The NiO content is similar for all natural (Mg,Fe)O inclusions, ranging from 1.06 to 1.35 wt%. However, sample A-7b from the Juina area shows an anomalously high NiO content of 3.3 wt%. The Cr<sub>2</sub>O<sub>3</sub> content (wt.%) varies from 0.08 in Juina and Machado River (Brazil) inclusions to a maximum of 0.54 for inclusions from the Springfield Basin (Australia). NaO is present in small amounts varying from 0 to 0.87 (wt%). Inclusions from Juina and Machado River are more enriched compared to inclusions from Eurelia and the Springfield Basin. MnO is always present, and varies from 0.14 to 0.86 (wt%). Minor elements were detected in small amounts: ZnO (0.03-0.09 wt.%) and V<sub>2</sub>O<sub>3</sub> (0.01 wt.%) were measured for inclusions from Juina area and Machado River, but they were absent in Australian inclusions.

**Table 4.8**– Chemical composition of natural (Mg,Fe)O diamond inclusions recovered from the Juina area and Machado River (Brazil)

	<b>1-49*</b>	<b>7-100*</b>	<b>A-7b*</b>	<b>1-143*</b>	<b>P11**</b>	<b>P12**</b>
SiO <sub>2</sub>	-	-	-	-	0.05	0.24
Al <sub>2</sub> O <sub>3</sub>	0.039	0.085	0.063	0.038	0.008	0.24
Na <sub>2</sub> O	0.187	0.172	0.876	0.011	0	0.09
NiO	1.060	1.347	3.322	1.078	1.20	1.23
Cr <sub>2</sub> O <sub>3</sub>	0.084	0.661	0.509	0.077	0.12	0.30
<b>FeO</b>	<b>33.082</b>	<b>28.000</b>	<b>49.996</b>	<b>34.617</b>	<b>19.27</b>	<b>20.59</b>
<b>MgO</b>	<b>67.829</b>	<b>72.434</b>	<b>46.520</b>	<b>66.223</b>	<b>78.94</b>	<b>77.03</b>
ZnO	0.031	0.065	0.091	0.035	-	-
V <sub>2</sub> O <sub>3</sub>	0.011	0.007	0.015	0.011	-	-
MnO	0.175	0.539	0.855	0.169	0.21	0.14
<b>Total</b>	<b>102.499</b>	<b>103.309</b>	<b>102.246</b>	<b>102.260</b>	<b>99.19</b>	<b>99.86</b>

\* Juina area (Brazil); \*\* Machado River (Brazil)

4. Results (2): Flank Method Applications

**Table 4.9**– Chemical composition of natural (Mg,Fe)O inclusions in lower mantle diamonds recovered from the Ororoo district (South Australia)

	5-11A*	5-11B*	5-11C*	5-11D*	5-11E*	5-11F*	F5-07C**	F5-07D**	F5-07E**	F5-07F**	F6-04B**	F6-04D**
SiO <sub>2</sub>	-	-	-	-	-	-	-	-	-	-	-	-
Al <sub>2</sub> O <sub>3</sub>	-	-	0.006	0.007	0.004	0.002	0.033	-	-	0.004	0.017	0.023
Na <sub>2</sub> O	0.027	0.0236	0.022	0.031	0.025	0.018	0.015	0.0286	0.024	0.026	0.022	0.014
NiO	1.138	1.194	1.116	1.177	1.108	1.093	1.288	1.214	1.249	1.228	1.263	1.266
Cr <sub>2</sub> O <sub>3</sub>	0.158	0.182	0.148	0.190	0.172	0.165	0.271	0.136	0.124	0.137	0.543	0.563
<b>FeO</b>	<b>22.218</b>	<b>22.65</b>	<b>21.754</b>	<b>22.553</b>	<b>22.257</b>	<b>21.055</b>	<b>23.605</b>	<b>22.71</b>	<b>23.07</b>	<b>22.956</b>	<b>22.038</b>	<b>22.088</b>
<b>MgO</b>	<b>77.503</b>	<b>75.602</b>	<b>76.289</b>	<b>76.834</b>	<b>76.02</b>	<b>75.691</b>	<b>75.195</b>	<b>77.2</b>	<b>77.18</b>	<b>76.593</b>	<b>75.333</b>	<b>77.588</b>
ZnO	-	-	-	-	-	-	-	-	-	-	-	-
V <sub>2</sub> O <sub>3</sub>	-	-	-	-	-	-	-	-	-	-	-	-
MnO	0.249	0.249	0.240	0.249	0.228	0.236	0.251	0.244	0.255	0.242	0.244	0.265
<b>Total</b>	<b>101.293</b>	<b>99.901</b>	<b>99.576</b>	<b>101.042</b>	<b>99.814</b>	<b>98.260</b>	<b>100.657</b>	<b>101.534</b>	<b>101.902</b>	<b>101.186</b>	<b>99.458</b>	<b>101.807</b>

\* Eurelia kimberlite K7

\*\* Springfield Basin

#### 4. Results (2): Flank Method Applications

The flank method was applied to determine the  $\text{Fe}^{3+}/\Sigma\text{Fe}$  ratio in (Mg,Fe)O from lower mantle diamonds.  $\text{Fe}^{3+}/\Sigma\text{Fe}$  ratios and  $L\beta/L\alpha$  ratios are reported in Table 4.10. Results show a large range of  $\text{Fe}^{3+}/\Sigma\text{Fe}$ , varying from 0.01 to 0.13. As equation (8) (see § 3.3) was calibrated for a Fe compositional range from 0.2 to 46 wt%, it was not possible to measure  $\text{Fe}^{3+}/\Sigma\text{Fe}$  for sample A7-b recovered from Juina area (Brazil) (Fe = 50 wt%).

**Table 4.10** – Natural (Mg,Fe)O diamond inclusions: flank method  $L\beta/L\alpha$  ratios (counts per second) as a function of the bulk Fe content (wt%) and the related  $\text{Fe}^{3+}/\Sigma\text{Fe}$  ratio obtained using the flank method calibration for ferroperricite.

Sample	Fe (wt%)	$L\beta/L\alpha$	$\text{Fe}^{3+}/\Sigma\text{Fe}$
<b>F6-04B</b>	17.3(1)	1.16(2)	0.04
<b>F6-04D</b>	16.9(2)	1.12(2)	0.12
<b>F5-07C</b>	18.3(1)	1.17(3)	0.01
<b>F5-07D</b>	17.4(2)	1.14(3)	0.08
<b>F5-07E</b>	17.6(1)	1.16(1)	0.01
<b>F5-07F</b>	17.7(1)	1.16(2)	0.06
<b>511A</b>	17.1(1)	1.15(2)	0.04
<b>5-11B</b>	17.6(1)	1.17(2)	0.04
<b>5-11C</b>	-	-	-
<b>5-11D</b>	17.4(2)	1.14(1)	0.09
<b>5-11E</b>	17.4(1)	1.17(1)	0.01
<b>5-11F</b>	16.7(1)	1.14(2)	0.05
<b>1-49 I</b>	25.3(2)	1.05(3)	0.08
<b>7-100</b>	21.5(1)	0.97(3)	0.12
<b>1-143</b>	26.2(2)	1.04(3)	0.13
<b>P11</b>	14.3(2)	0.85(2)	0.08
<b>P12</b>	15.3(1)	0.82(1)	0.12

## 5. Discussion and Future Perspectives

### 5.1 Overview of the present study and research goals achieved

With the aim of providing insight into the redox conditions at which diamonds formed at lower mantle conditions, the present study was focused mainly on the determination of the  $\text{Fe}^{3+}/\Sigma\text{Fe}$  ratios in natural (Mg,Fe)O ferropericlyase from lower mantle diamonds. As already discussed, the lower mantle is inaccessible to direct observations, and hence diamonds with inclusions from such depths are the only samples available. However, diamond inclusions are commonly less than 50 microns and only a few samples with greater sizes (200-300  $\mu\text{m}$ ) are available, which limits the possibility to explore this region of the Earth's mantle. There are only a few experimental techniques that can be applied that are easily accessible and non-destructive in nature. The latter characteristic is crucial as diamonds with their mineral inclusions are sources of precious information about the deep mantle reservoirs, the evolution of the Earth's mantle through the time, and origin of deep mantle magmas.

The flank method using the electron microprobe has been successfully calibrated on synthetic garnets (Höfer and Brey, 2007) for the determination of iron oxidation state and applied to garnet inclusions for thermobarometry and oxybarometry studies (Creighton et al., 2009). As discussed in previous chapters, the advantages offered by the electron microprobe enable the flank method to quantitatively determine the  $\text{Fe}^{3+}/\Sigma\text{Fe}$  ratios for non-destructive and easy routine measurements. The accuracy of flank method measurements is comparable to the widely used Mössbauer spectroscopy method for the determination of  $\text{Fe}^{3+}/\Sigma\text{Fe}$ , with the additional advantage of a spatial resolution on the order of few  $\mu\text{m}$  (compared to no smaller than 100  $\mu\text{m}$  for Mössbauer spectroscopy). Thus, the same approach was applied for (Mg,Fe)O ferropericlyase to expand lower mantle studies to those associated with diamond genesis.

In the present study the flank method was successfully calibrated for a set of synthetic (Mg,Fe)O samples along the MgO-FeO join involving a wide range of redox ratios. In this work the flank method – exploited through the measure of the  $L\beta/L\alpha$  intensity ratios – showed a good correlation as a function of  $\Sigma\text{Fe}$  (wt%) and  $\text{Fe}^{2+}$  (wt%). The trend appears to be different to that observed for garnets, showing a polynomial behavior, in contrast to the linear correlation found for garnets (see chapter 3 for details). The  $L\beta/L\alpha$  ratios are affected by Fe absorption during

## 5. Discussion and Future Perspective

electron microprobe measurements, with a saturation trend for compositions close to the FeO end-member,

Once the method was successfully calibrated for the electron microprobe in use at the Bayerisches Geoinstitut, the study proceeded with the exploration of possible applications, with the aim to answer the following questions:

- Considering the high spatial resolution offered by electron microprobe, is it possible to apply the flank method in order to detect possible compositional variations due to exsolution phenomena in natural (Mg,Fe)O from lower mantle? Previously, (Mg,Fe)Fe<sub>2</sub>O<sub>4</sub> exsolution from primary (Mg,Fe)O have been reported in diamonds, witnessing a variation in redox conditions over the diamond history.

- Is it possible to apply the flank method in order to study the variation of Fe<sup>3+</sup> involved in diffusion processes? So far there are only few techniques able to observe on the micro scale the variation of Fe<sup>3+</sup> along iron diffusion profiles.

Is the flank method calibration obtained for synthetic (Mg,Fe)O applicable to natural (Mg,Fe)O inclusions from lower mantle diamonds? Are the results obtained consistent with the observations obtained for synthetic samples? Is there an innovative contribution of this study to lower mantle diamond studies?

## 5.2 Compositional variation determined by flank method

### 5.2.1 Detection of extra phase(s) other than primary (Mg,Fe)O

In paragraph § 4.1.1 the sensitivity of the flank method was explored for the detection and possible quantification of extra phase(s) in the primary (Mg,Fe)O single crystals. The behavior of the  $L\beta/L\alpha$  ratios as a function of bulk  $\sum\text{Fe}$  and  $\text{Fe}^{2+}$  (wt%) was sensitive to the presence of a variable amount of (Mg,Fe)Fe<sub>2</sub>O<sub>4</sub> in (Mg,Fe)O, showing a deviation of data points from the theoretical trend described by synthetic (Mg,Fe)O. The presence of magnesioferrite exsolving from (Mg,Fe)O can affect the flank method measurements, and the  $L\beta/L\alpha$  ratio can be either underestimated or overestimated. FeFe<sub>2</sub>O<sub>4</sub> magnetite, with structural configuration similar to (Mg,Fe)Fe<sub>2</sub>O<sub>4</sub>, shows a  $L\beta/L\alpha$  ratio of 0.85, which is intermediate between the values for Fe<sub>2</sub>O<sub>3</sub> and FeO (0.59 and 1.40, respectively), but not consistent with the variation of  $L\beta/L\alpha$  observed as a function of  $\sum\text{Fe}$  and  $\text{Fe}^{2+}$  (wt%) for the (Mg<sub>x</sub>Fe<sub>1-x</sub>)O solid solution curve. Therefore, variation of  $L\beta/L\alpha$  may be due to the Fe site occupancy and the possible presence of clusters in the structure. Flank method measurements are affected by a variation in the chemical composition and the structural configuration, and a variation of the  $L\beta/L\alpha$  as a function of (Mg,Fe)Fe<sub>2</sub>O<sub>4</sub> content can be observed for (Mg,Fe)Fe<sub>2</sub>O<sub>4</sub> contents from zero to 11 % by volume. On the basis of these results, in some cases the flank method – complemented by Mössbauer data – may enable the detection of extra phase(s) for reasonable amounts of (Mg,Fe)Fe<sub>2</sub>O<sub>4</sub> as a result of exsolution from (Mg,Fe)O during the diamond genesis and/or exhumation. In fact, an appropriate and careful constraint of variables such as  $\sum\text{Fe}$ ,  $\text{Fe}^{3+}/\sum\text{Fe}$ ,  $L\beta/L\alpha$  and the (Mg,Fe)Fe<sub>2</sub>O<sub>4</sub> content may enable the extrapolation of theoretical lines to correct for impurities in the (Mg,Fe)O bulk composition. However it does not yet appear possible to quantify it solely with flank method measurements. Therefore, at this stage it is possible to detect the presence of extra phases in natural samples (if they occur in a reasonable amount), but there are not enough data to apply corrections for natural inclusions. Further improvements in this regard are needed.

### 5.2.2 Fe<sup>3+</sup> variation along diffusion profiles

In paragraph §4.1.2 the application of the flank method to synthetic (Mg,Fe)O crystals obtained from diffusion experiments is described, in order to test the sensitivity of the method to small variations of Fe<sup>3+</sup> in the presence of diffusion phenomena. The Fe<sup>3+</sup>/ΣFe ratio was determined using equation (8) (see § 4.2.3). Figure 5.1 shows the variation of Fe<sup>3+</sup>/ΣFe for measurements performed along the diffusion profile K685\_1. Measurements were performed using a 2-3 μm step.

Flank method measurements are sensitive to a variation of Fe bulk composition for values higher than 3.4 wt%, which essentially represents the detection limit for flank method measurements on (Mg,Fe)O. This is the first time that the variation of the Fe<sup>3+</sup>/ΣFe ratio has been measured directly along a diffusion profile. The flank method enables the measurement of small variations in Fe<sup>3+</sup> content, which tend to decrease along with ΣFe on the diffusion gradient, moving from a FeO-rich region toward a MgO-rich region. Such behavior follows from the negative correlation observed earlier for Fe<sup>2+</sup> and Fe<sup>3+</sup> (§4.1.2 Fig. 4.11b and 4.11d).

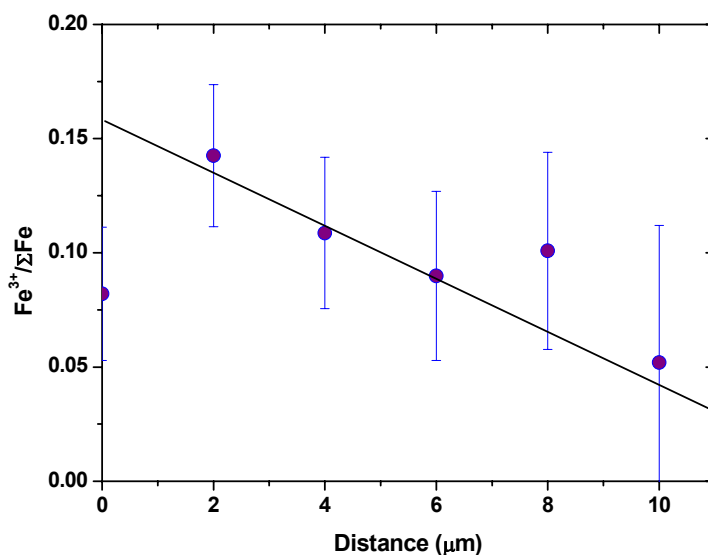


**Fig. 5.1** – Variation of Fe<sup>3+</sup>/ΣFe vs. measurement position along the diffusion profile for sample K685\_1. Measurements are expressed as distance in μm. Error bars are propagated considering independent errors for ΣFe (wt%) and Lβ/Lα ratio using equation (8) (see §3.3).

The variation of Fe<sup>3+</sup>/ΣFe with ΣFe can provide information on the variation of oxygen fugacity conditions along the diffusion gradient. Fe<sup>3+</sup> contents (p.f.u.) plotted versus the Fe number (Fe# = (Fe/Fe+Mg)) can be compared with data from the literature for (Mg,Fe)O equilibrated with iron

## 5. Discussion and Future Perspective

metal (Srećec et al., 1987) (Fig. 5.2). Srećec et al. (1987) observed that the  $\text{Fe}^{3+}$  concentration increases as a function of Fe content, and the variation is temperature independent within the range studied (1433-1573 K). A similar behavior (increasing  $\text{Fe}^{3+}$  concentration with increasing Fe#) was observed at constant oxygen fugacity within the single-phase (Mg,Fe)O stability field (Speidel, 1967). Results obtained for (Mg,Fe)O crystals from diffusion experiments performed at 1400°C and 5 GPa measured in the present study show an increase of  $\text{Fe}^{3+}$  concentration as a function of Fe content in the Fe compositional range between zero and 0.2. Redox conditions during the experiments were buffered using the Mo-MoO<sub>2</sub> buffer, which is slightly more oxidising than the Fe-(Mg,Fe)O buffer (O'Neill, 1986). Within the uncertainty of the data, it is plausible that the  $\text{Fe}^{3+}$  concentration is changing at constant  $f_{\text{O}_2}$  in response to the variation of the Fe bulk concentration caused by diffusion, implying that rate of diffusion of  $\text{Fe}^{3+}$  and  $\text{Fe}^{2+}$  is similar in (Mg,Fe)O.

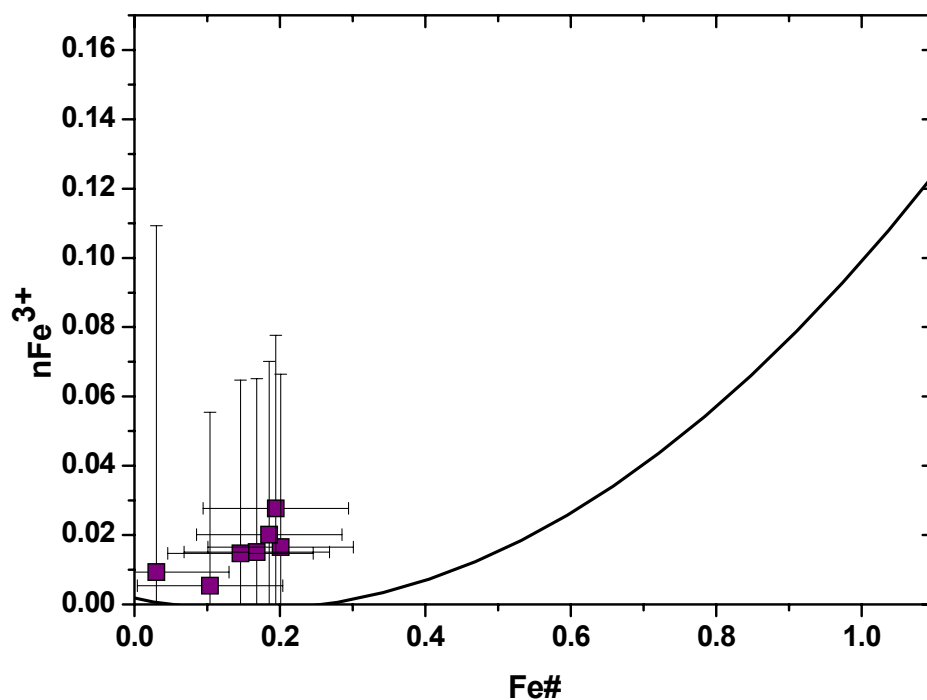


**Fig. 5.2** –  $\text{Fe}^{3+}$  concentration vs. Fe# of (Mg,Fe)O along the diffusion profile K685\_1 (diffusion experiment performed at 1400°C and 5 GPa at the Mo-MoO<sub>2</sub> buffer) (purple squares). Results are compared to literature data for (Mg,Fe)O equilibrated with iron metal in the temperature range between 1433K and 1573K (Srećec et al., 1987) (solid line).

### 5.3 Oxygen fugacity in lower mantle (Mg,Fe)O ferropericlase

The present work has demonstrated for the first time that it is possible to measure *in situ*  $\text{Fe}^{3+}/\sum\text{Fe}$  from lower mantle diamond inclusions directly using the electron microprobe. Inclusions were selected from three localities worldwide (Juina area, Brazil; Machado River, Brazil; Eurelia kimberlite and Springfield Basin, Australia). The flank method has expanded the database of quantitative determinations of  $\text{Fe}^{3+}/\sum\text{Fe}$  of inclusions worldwide to include inclusions 20-30 microns in size. The high spatial resolution offered by the electron microbeam made it possible to measure a sample as small as 15  $\mu\text{m}$  in diameter (P11 sample, Machado River, Brazil). Therefore, the flank method may enable the detection of even small variation (e.g. on the micro scale) of the redox state with an accuracy comparable to that of Mössbauer spectroscopy.

For all the inclusions measured worldwide,  $\text{Fe}^{3+}/\sum\text{Fe}$  was measured using equation (8) and (9) (see § 4.2.3) and shows a variation from 1 to 13%. An estimation of the redox conditions under which natural (Mg,Fe)O were formed can be performed using the approach suggested earlier (McCammon et al., 2004b). In Figure 5.3a trivalent cation content (p.f.u.) measured for the inclusions investigated in the present work are plotted versus the Na content (p.f.u.). The deviation of data from the 1:1 trend between monovalent and trivalent cations provides a measure of the number of vacancies required to balance the charge in the structure (Fig.5.3a), and the variation of these vacancy concentrations with total iron content provides a qualitative measure of oxygen fugacity (Fig.5.3b).

From Figure 5.3b it is evident that inclusions measured in the present work have experienced different redox conditions, ranging from reducing conditions near the equilibrium (Mg,Fe)O-Fe metal to more oxidizing conditions represented by the Re-ReO<sub>2</sub> buffer. Inclusions from Brazil (empty and full squares) show uniformly relatively oxidizing conditions, whereas inclusions from Eurelia kimberlite and Springfield Basin (Australia) (purple triangles) show a large variation of redox conditions, even for inclusions recovered from the same host diamonds. In fact, all the (Mg,Fe)O ferropericlase inclusions from Australia cover nearly the entire oxygen fugacity range. The large range of oxygen fugacities is consistent with results already determined for larger inclusions (200-300  $\mu\text{m}$ ) from lower mantle diamonds recovered from São Luiz, Brazil (McCammon et al., 1997) and Kankan, Guinea (McCammon et al., 2004b): Kankan and São Luiz inclusions recorded quite reduced conditions, whereas inclusions recovered from Juina showed more oxidizing conditions.

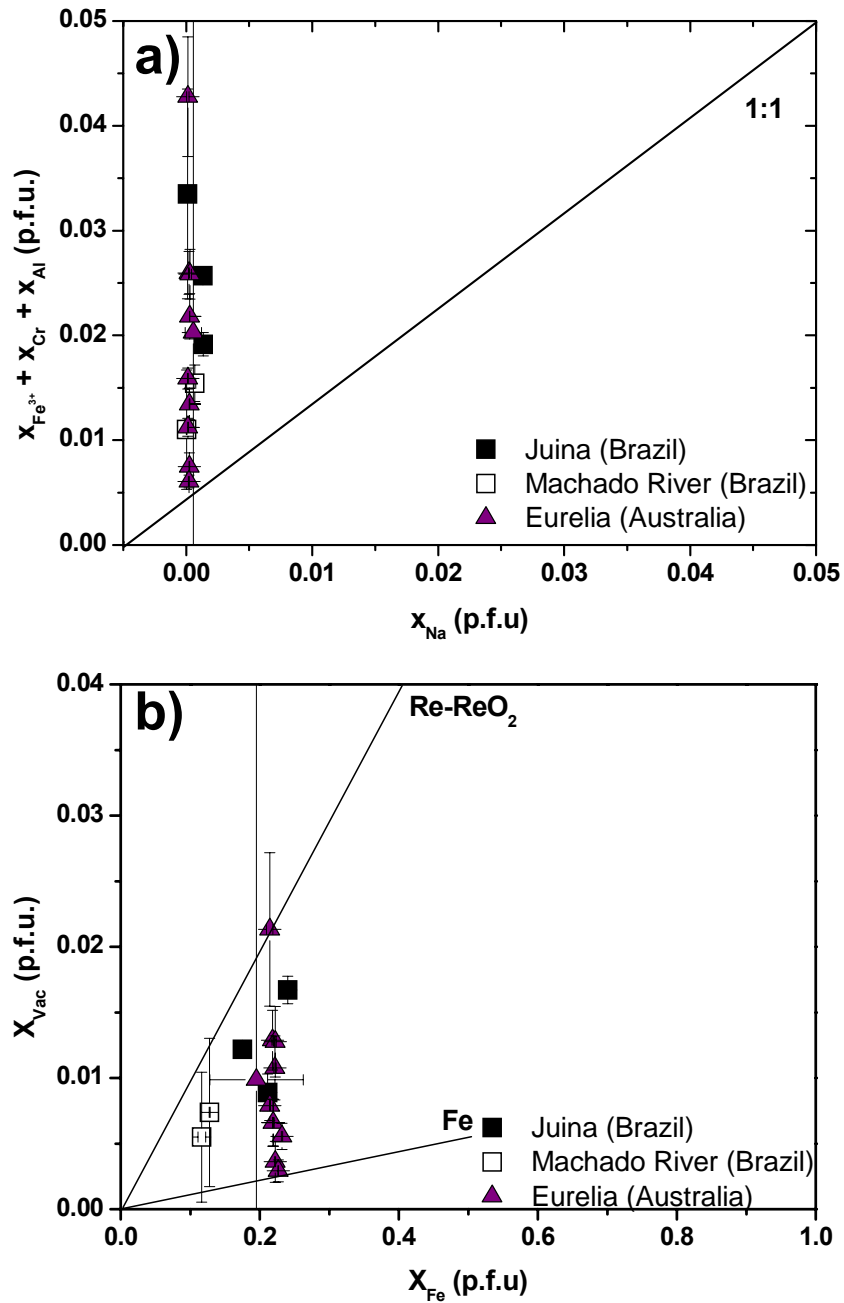


**Fig. 5.3** – a) Trivalent cation abundance versus Na abundance for (Mg,Fe)O inclusions in lower mantle diamonds, expressed in cations per formula unit. The 1:1 line represents stoichiometric charge balance. b) Cation vacancy concentration determined from Fig. 5.3a ( $= \frac{1}{2} (X_{\text{Fe}^{3+}} + X_{\text{Al}} + X_{\text{Cr}} - X_{\text{Na}})$ ) as a function of total iron content. The solid lines indicate the variations reported in the literature for Fe-(Mg,Fe)O and Re-ReO<sub>2</sub> equilibria (McCammon et al., 2004a).

## 5. Discussion and Future Perspective

Inclusions recovered from Eureka kimberlite and the Springfield Basin (Australia) recorded the largest redox variation, with  $\text{Fe}^{3+}/\Sigma\text{Fe}$  varying from 1 to 12%. Surprisingly, the whole range of redox ratios measured so far can be observed with different intervals in inclusions recovered from the same host diamonds (two from diamond F6-04, four from F5-07, five from 5-11, see § 4.2.3, Table 4.9), presumably incorporated during different diamond growth stages (perhaps at different depths, or as a consequence of mantle convection, or after having experienced different magmatic events). This may also suggest a drastic change in the oxygen fugacity conditions which occurred in the environment where the diamond formed and affected their growths. Such strong variations in oxygen fugacity may have a strong impact on chemical and physical properties and mantle processes.

### 5.3.1 Implications for diamond formation

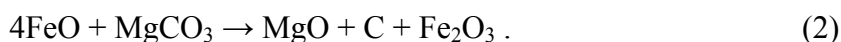
The crucial question of how ultradeep diamonds form is still intensively debated. The widely accepted theory regarding diamond genesis is in favor of subducted oceanic crust depositing at the transition zone – lower mantle boundary (660 km; Ringwood, 1991; Stachel et al., 2000, Walter et al., 2008). As already discussed in the introduction, the negative Eu anomalies observed in silicate inclusions combined with the crustal carbon isotope signatures of the host diamonds support this hypothesis (Stachel et al., 2000, Tappert et al., 2005). In contraposition to ultra deep diamond formation, most recent theories for eclogitic diamond formation are based on the presence of mantle-seated carbonatites in the lithosphere, as well as in the case for the more obvious peridotitic diamonds (Thomassot et al., 2007). Therefore, the idea is becoming more accepted that lithospheric diamonds could also crystallize from a metasomatic C-H-O-N-S or carbonatitic fluid/liquid (Thomassot et al., 2009, and reference therein). On basis of these observations it can be considered that deep-seated fluids introduced by Thomassot et al. (2009) might also be extended to greater depths (the transition zone – lower mantle boundary), and the mantle-related model could be also applicable for the lower mantle diamond formation.

The main mechanism, however, suggested for diamond crystallization may involve the following reaction (Liu 1999):



## 5. Discussion and Future Perspective

But possibly a coupled redox reaction takes place in the deep Earth to generate diamonds such as the the following:



Reaction (2), proposed by McCammon (2006), could also be one of the mechanisms to charge balance the high  $\text{Fe}^{3+}$  concentration in  $(\text{Mg,Fe})(\text{Si,Al})\text{SiO}_3$ . In fact, Mg,Si-perovskite was found to contain a significant amount of  $\text{Fe}^{3+}$  in the presence of Al, even under reducing conditions, both experimentally (Lauterbach et al., 2000; Frost et al., 2004a) and based on observations of natural samples as diamond inclusions (McCammon et al., 1997; McCammon et al., 2004b). Moreover, the reduction of carbonates involved in diamond formation according to reaction (2) would explain why  $(\text{Mg,Fe})\text{O}$  ferropericlasite is so far the most abundant phase recovered in lower mantle diamonds (more than half occurrences worldwide).

If the mantle-seated carbonatitic model can be also applied to explain the formation of ultra-deep diamonds, it is possible that the redox conditions at depths below 660 km associated to diamond formation may be strongly related to the initial composition of materials subducting in the lower mantle (subduction-related evidence) but locally influenced by the presence of the composition of mantle-seated carbonatites (mantle-related evidence). Diamonds may therefore precipitate from either reduced or more oxidized fluids. According to the material in subduction, or mantle-seated carbonatites, or a combination of both, different redox behavior may then determine the redox conditions involved at the time of diamond crystallization. On the basis of results obtained in the present study,  $\text{Fe}^{3+}/\sum\text{Fe}$  measured for diamond inclusions worldwide combined with data already obtained for other inclusions previously measured from Kankan (Guinea) and São Luiz (Brazil) show a geographical correlation of the variation of oxygen fugacity (Fig. 5.4).

## 5. Discussion and Future Perspective

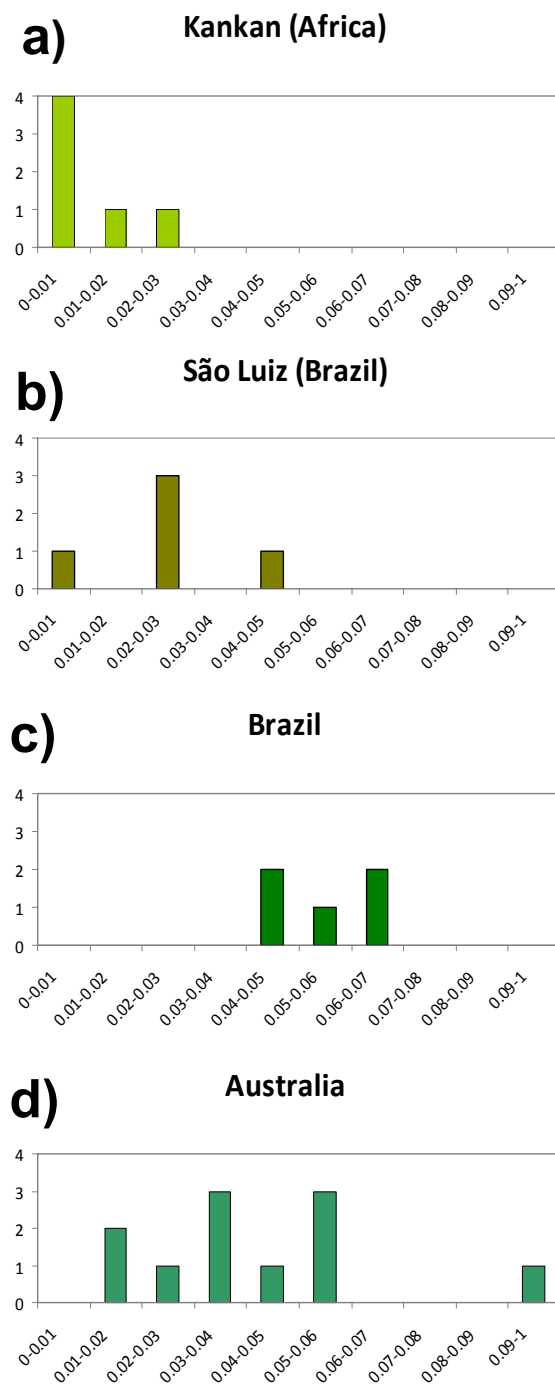


**Fig. 5.4** – Oxygen fugacity variation in (Mg,Fe)O ferropericlase inclusions worldwide. Oxygen fugacities for each inclusion are estimated from Fig. 5.3a as the slope of the line including the origin. Data for Kankan (Guinea) (a) and São Luiz (Brazil) (b) inclusions are based on McCammon et al. (2004b).

## 5. Discussion and Future Perspective

Redox conditions registered in lower mantle diamond inclusions studied in the present work compared with data from the literature vary from reducing in the African province (Kankan Guinea), moving towards more oxidizing in the Brazilian regions (Juina area and Machado River), where they partially overlap a more reduced region (São Luiz). Australian inclusions recovered from Eurelia kimberlite and Springfield Basin (Australia) show a large redox variation among all twelve inclusions measured.

Flank method measurements on inclusions extracted from their host diamonds can therefore indicate approximate  $fO_2$  conditions. However once the inclusions are removed out of the host diamond, information on the direction of any redox gradient that may have evolved, and possible correlation with diamond growth or anomalies in the variation of the redox conditions through time, are lost. In fact the diamond itself records in the growth zones information regarding all of the different environments which it has gone through in traveling before reaching the surface.

With regard to the Australian diamonds, the C isotopic abundance consistent with marine carbonates may indicate that deeply subducted carbonates were involved in the formation of the presumed ultradeep diamonds from Eurelia (Tappert, et al. 2009). The ultimate source of these diamonds has been linked to the subducted oceanic lithosphere of the proto-Pacific plate during the Permian period (Fig. 5.5). As can be seen from Figure 5.5, the Juina and São Luiz regions (Brazil) and Kankan (Guinea) (the latter not reported in the map) are relatively young (around 95 Ma, Cretaceous), compared to the Australian kimberlite occurrences which are dated 170 Ma. At the same time the Brazilian localities are at the opposite margins of the subduction of the proto-Pacific plate with respect to the Australian localities. It may be therefore speculated that the differences encountered between these localities in terms of mineral assemblages and  $Fe^{3+}/\Sigma Fe$  ratio (with the apparent sensitive redox gradient observable in Australian diamonds), may lie in a combination of different processes which determined their formation and subsequent emplacement at different geologic times.

## 5. Discussion and Future Perspective

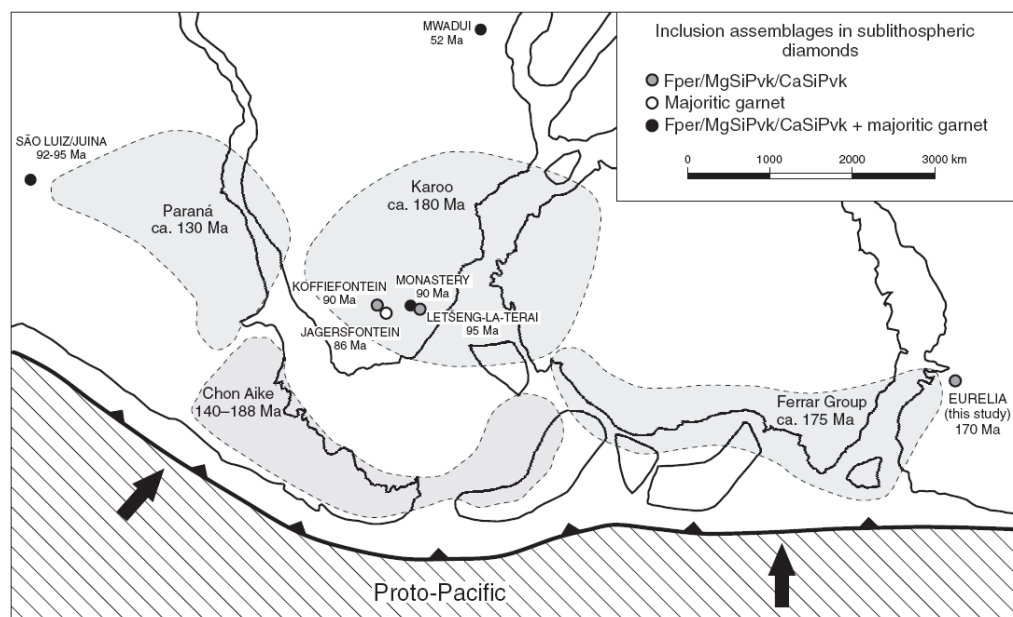


**Fig. 5.5** – Reconstruction of southern Gondwana before breakup showing locations of Mesozoic and early Cenozoic kimberlites with ultradeep diamonds. The main inclusion parageneses for ultradeep diamond populations at each locality are given. Emplacement ages for southern African kimberlites are based on Allsopp and Barrett (1975), Smith (1983), Allsopp et al. (1989), Rickard et al. (1989), and Stiefenhofer and Farrow (2004). Ages of kimberlitic sources for alluvial diamonds in the São Luiz–Juina area, Brazil, are based on Heaman et al. (1998). Areal extents of Mesozoic large igneous provinces (shaded gray) and ranges for their eruption ages are based on Hergt et al. (1991) and Pankhurst et al. (1998). Fper indicates ferropericlase; Pvk indicates perovskite. *From Tappert et al., (2009)*

Nevertheless, recent experimental data show that the  $\text{Fe}^{3+}$  solubility in ferropericlase in equilibrium with Mg,Si-perovskite and  $\text{SiO}_2$  stishovite decreases as a function of pressure (Tange et al., 2009). These results, combined with observations on natural samples (particularly the contribution provided by Australian inclusions), confirm Mg,Si-perovskite as the  $\text{Fe}^{3+}$ -like species in the lower mantle (McCammon 1997), and may provide constraints on a variation of redox conditions as a function of depth. Such redox condition variations in the region of the lower mantle where diamond formed may strongly affect the physical and chemical properties of the surrounding mantle and therefore have an impact on lower mantle dynamics.

#### 5.4 Future perspectives for flank method applications and lower mantle studies

It is evident that to constrain models of diamond genesis more accurately, it is necessary to perform a multi disciplinary study including isotopic and spectroscopic as well as optical studies. A study of nitrogen contents and carbon isotope abundance in diamonds can be decisive in providing insights into diamond genesis and diamond evolution through time. Cathodoluminescence offers an important tool to investigate diamond growth evolution (Bulanova, 1998; Schulze et al., 2004). In fact, by detecting the presence of different growth stages, it can provide information on the occurrence of different mechanisms and magmatic events that might have been involved in the diamond growth history, and possibly affect the oxygen fugacity conditions. In the same way, cathodoluminescence studies can aid in the identification of syngenetic inclusions. Such information is crucial in order to provide clues to the link between the genesis of diamond, its evolution through time, and its mineral inclusions. Assuming that carbonatitic liquids are present at lower mantle depths (Walter et al. 2008), a certain variability of the lower mantle could be locally determined by the occurrence of different types of carbonatitic liquids (from more reduced to quite oxidized). The redox gradient observed for the Australian inclusions may therefore be a consequence of the interaction between those liquids and the mineral assemblages occurring at different stages during the diamond growth.

The discovery of diamonds containing several inclusions which registered different oxygen fugacity conditions open the possibility of cathodoluminescence studies, combined with the flank method for the determination of  $Fe^{3+}/\Sigma Fe$ , that would enable the reconstruction of possible redox gradients experienced by the (Mg,Fe)O ferropericlase inclusions during diamond formation. This may provide further insight into the reliability of (Mg,Fe)O as an indicator of oxygen fugacity. Additionally, the study of isotopic variations recorded in different diamond growth zones may provide evidence of magmatic events that the diamond encountered in travelling through the mantle.

## 6. Concluding statements and further work

The experimental results obtained in the present study lead to the following conclusions:

1. Following the same approach by Höfer and Brey (2007) for garnet, the flank method was successfully calibrated using the Jeol XA-8200 electron microprobe at Bayerisches Geoinstitut for a set of (Mg,Fe)O samples synthesized at 15 GPa and 1800-2000°C over a Fe compositional range from  $\sim <3$  to 46.8% in weight and  $\text{Fe}^{3+}/\Sigma\text{Fe}$  from 1 to 15%. The flank method detection limit with regard to the Fe bulk composition corresponds to 3 wt%.

2. The values of  $\Sigma\text{Fe}$  (wt%) and  $L\beta/L\alpha$  (counts per second) ratios were obtained simultaneously by combining quantitative and qualitative analysis to quantify major elements and the  $\text{Fe}^{3+}/\Sigma\text{Fe}$  ratios.  $\text{Fe}^{3+}/\Sigma\text{Fe}$  determined by the flank method was generally in agreement within experimental error with Mössbauer data. The flank method offers several advantages: reduced measuring times of only a few hours (versus a minimum of two days for Mössbauer spectroscopy) and much higher spatial resolution of 1-10  $\mu\text{m}$  (versus no smaller than 100  $\mu\text{m}$ ). Therefore, the flank method appears to be suitable to determine  $\text{Fe}^{3+}/\Sigma\text{Fe}$  in natural ferropericlase from diamond inclusions, which are commonly less than 50  $\mu\text{m}$  in size.

3. For the first time *in situ*  $\text{Fe}^{3+}/\Sigma\text{Fe}$  was determined for (Mg,Fe)O ferropericlase inclusions from lower mantle diamonds worldwide (Juina area and Machado River, Brazil, Eurelia and Springfield Basin, Australia) of less than 50  $\mu\text{m}$  in size without destroying the samples. The smallest inclusion measured in the present work was 15  $\mu\text{m}$ .

4. The measured  $\text{Fe}^{3+}/\Sigma\text{Fe}$  ratio of the inclusions varied from 1 to 13%. Consideration of the trivalent cations and the cation vacancies required to balance the excess positive charge leads to the conclusion of varying oxygen fugacity conditions involved in the formation of the inclusions. These observations combined with the geographical correlation observed among all inclusions measured in the present work and from previous studies in literature leads to the suggestion of other mechanisms than subducted slabs being involved in diamond formation.

## 6. Concluding statements and further work

5. Flank method measurements are sensitive to chemical composition, because the presence of extra phases in (Mg,Fe)O can affect the  $L\beta/L\alpha$  ratio. However, it was not possible to observe a clear correlation as a function of the amount of magnesioferrite exsolved from (Mg,Fe)O ferropericlasite. Therefore, the energies associated with the  $FeL\alpha$  and  $FeL\beta$  lines might be affected differently depending on the Fe site distribution (e.g., clustering) and structural and electronic configuration (e.g., spin state). Further work could focus on a combined TEM and flank method study to investigate the variation of the  $L\beta/L\alpha$  ratio as a function of Fe clustering with increasing  $\Sigma Fe$  and increasing amount of impurities exsolved from (Mg,Fe)O.

6. The  $L\beta/L\alpha$  ratio is highly sensitive to iron concentration, suggesting the possibility for the flank method to be applied to diffusion studies. The application of the flank method to  $\Sigma Fe$  gradients demonstrated for the first time the possibility to follow the variation of the  $Fe^{3+}/\Sigma Fe$  ratio on a micron scale. Moreover, diffusion studies provided a measure of the lower detection limit of  $\Sigma Fe$  for flank method measurements on (Mg,Fe)O ferropericlasite (3 wt% of  $\Sigma Fe$ ).

The next steps in constraining  $Fe^{3+}/\Sigma Fe$  ratios for the lower mantle include extending the calibration of the flank method to mineral phases other than (Mg,Fe)O ferropericlasite. Listed below are possible research projects for future studies:

1. The calibration of the flank method on Mg,Si-perovskite would open the possibility of measuring *in situ*  $Fe^{3+}$  solubility between coexisting (Mg,Fe)O in lower mantle assemblages. Since it was reported that the  $Fe^{3+}$  solubility in ferropericlasite is pressure dependent, it is plausible to consider the couple (Mg,Fe)O-Mg,Si-perovskite as a potential geobarometer for lower mantle depths.

2. During the last few years the flank method has seen constant improvements and has been shown to be an important tool for studies of to deep and ultradeep diamonds (Höfer and Brey 2007; Creighton et al. 2008; present study). The calibration may be potentially extended to other mantle phases intensively studied such as pyroxenes, which have applications in geothermometry (Ellis and Green, 1979).

## *6. Concluding statements and further work*

3. In order to investigate the mechanisms which could control the redox conditions during lower mantle diamond formation, a set of high pressure high temperature experiments using a multi anvil apparatus could be carried out. Experimental studies with the aim of reproducing diamond formation and the phase equilibria at lower mantle conditions also in the presence of carbonatitic liquids could provide new insight into the effect of liquids on the evolution of diamond formation and their possible influence on the variation of oxygen fugacity.

## 7. References

- Agee, C.B. (1998) Phase transformations and seismic structure in the upper mantle and transition zone. *Reviews in Mineralogy and Geochemistry*, 37, 1, 165-203.
- Albee, A.L. and Chodos, A.A. (1970) Semiquantitative electron microprobe determination of  $\text{Fe}^{2+}/\text{Fe}^{3+}$  and  $\text{Mn}^{2+}/\text{Mn}^{3+}$  in oxides and silicates and its application to petrologic problems. *American Mineralogist*, 55, 491-501.
- Allsopp, H.L., and Barrett, D.R., (1975) Rb-Sr age determinations on South African kimberlite pipes. *Physics and Chemistry of the Earth*, v. 9, p. 605–617.
- Allsopp, H.L., Bristow, J.W., Smith, C.B., Brown, R., Gleadow, A.J.W., Kramers, J.D., and Garvie, O.G. (1989) A summary of radiometric dating methods applicable to kimberlites and related rocks, in Ross, J., ed., *Kimberlites and related rocks*. Volume 1: Geological Society of Australia Special Publication 14, p. 343–357.
- Anderson, W.W. and Ahrens, T.J. (1994) An equation of state for liquid iron and implications for the Earth's core. *J. Geophys. Res.*, 99, 4273-4284.
- Andrault, D. (2001) Evaluation of (Mg,Fe) partitioning between silicate perovskite and magnesiowüstite up to 120 GPa and 2300 K. *J. Geophys. Res.*, 106 (B2), 2079–2087.
- Badro, J., Fiquet, G., Guyot, F., Rueff, J.-P., Struzhkin, V.V., Vankò, G., Monaco, G. (2003) Iron Partitioning in Earth's Mantle: Toward a Deep Lower Mantle Discontinuity. *Science*, 300, 789-791.
- Berlin, J., Spilde, M., Brearley, A.J., Draper, D.S., and Dyar, M.D. (2004) In-situ determination of  $\text{Fe}^{3+}/\Sigma\text{Fe}$  of spinels by electron microprobe: an evaluation of the flank method. LPI Contribution. Vol. 1203, pp. 12.
- Berry, A.J., O'Neill, H.S.C., Jayasuriya, K.D., Campbell, S.J., and Foran, G.J. (2003) XANES calibrations for the oxidation state of iron in a silicate glass. *American Mineralogist*, 88, 967-977.
- Bibby, D.M. (1982) Impurities in natural diamonds. In: Throver, P.A. (Ed.), *Chemistry and Physics of Carbon* 18, 1-91. Marcel Dekker, New York.
- Braginsky, S.I. (1964) Magnetohydrodynamics of the Earth's core? *Geomagnetism and Aeronomy*, 4, 698-712.

## 7. References

- Brey, G.P., Bulatov, V., Girnisc, A., Harris, J.W., Stachel, T. (2004) Ferropericlasite - a lower mantle phase in the upper mantle. *Lithos*, 77, 655-663.
- Brown, G.E., JR., and Parks, G.A. (1989) Synchrotron based X-ray absorption studies of cation environments in Earth materials. *Reviews of Geophysics*, 27, 519-533.
- Buffett B. A., Garnero, E. J. & Jeanloz, R. (2000) Sediments at the top of Earth's core. *Science* 290, 1338–1342.
- Bulanova, G.P. (1995) The formation of diamond. *Journal of Geochemical Exploration*, 53, 1-23.
- Bulanova, G.P., Smith, C.B., Kohn, S.C., Walter, M.J., Gobbo, L., Kearns, S. (2008) Machado River, Brazil – a newly recognised ultradeep diamond occurrence. 9<sup>th</sup> International Kimberlite Conference.
- Calas, G., Bassett, W.A., Petiau, J., Steinberg, M., Tchoubar, D., and Zarka, A. (1984) Some mineralogical applications of synchrotron radiation. *Physics and Chemistry of Minerals*, B11, 17-36.
- Canil, D. and O'Neill, H. (1996) Distribution of Ferric Iron in some Upper-Mantle Assemblages. *Journal of Petrology*, 37, 609-635.
- Chen, J.R., Gordon, B.M., Hanson, A.L., Jones, K.W., Kraner, H.W., Chao, E.C.T., and Minkin, J.A. (1984) Synchrotron X-ray fluorescence and extended X-ray absorption fine structure analysis. *Scanning*, 4, 1483-1500.
- Chen G., Liebermann R.C., Weidner D.J. (1998) Elasticity of Single-Crystal MgO to 8 Gigapascals and 1600 Kelvin. *Science* 280, 1913-1916.
- Creighton, S., Stachel, T., Matveev, S., Höfer, H., McCammon, C., Luth, R. (2009) Oxidation of Kaapvaal lithospheric mantle driven by metasomatism. *Contrib. Mineral. Petr.*, 157, 491-504.
- Davies, R.M., Griffin, W.L., Pearson, N.J., Andrew, A.S., Doyle, B.J. and O'Reilly, S.Y. (1999) Diamonds from the deep: pipe DO-27, Slave Craton, Canada. In the J.B. Dawson Volume, *Proceedings of the VIIth International Kimberlite Conference*, (ed. J.J. Gurney, J.L. Gurney, M.D. Pascoe and S.H. Richardson), Red Roof Design, Cape Town, 148-155.
- Davies, G.F. and Gurnis, M. (1986) Interaction of mantle dregs with convection: Lateral heterogeneity at the core-mantle boundary. *Geophys. Res. Lett.*, 13, 1517-1520.
- Deines, P. (1980) The carbon isotopic composition of diamonds: relationship to diamond shape, color, occurrence and vapor composition, *Geochim. Cosmochim. Acta* 44 943– 961.

## 7. References

- Delaney, J.S., Dyar, M.D., Sutton, S.R., and Bajt, S. (1998) Redox ratios with relevant resolution: Solving an old problem by using the synchrotron microXANES probe. *Geology*, 26, 139-142.
- Dodd, C.G., and Rippe, P.H. (1978) Soft X-ray spectroscopy of ferrous silicates. *Physics and Chemistry of Minerals*, 3, 145-162.
- Duffy, T. S., Hemley, R. J. & Mao, H. K. (1995) Equation of state and shear strength at multimegabar pressures: Magnesium oxide to 227 GPa. *Phys. Rev. Lett.* 74, 1371–1374.
- Dziewonski A.M. and Anderson D.L. (1981) Preliminary Reference Earth Model. *Physics of the Earth and Planetary Interior* 25, 297-356.
- Dubrovinsky, L. and Lin, J.-F. (2009) Mineral Physics Quest to the Earth's Core. *EOS transactions, American Geophysical Union*, 90, 21-22.
- Enders, M., Speer, D., Maresch, W.V., and McCammon, C. (2000) Ferric/ferrous iron ratios in sodic amphiboles: Mössbauer analysis, stoichiometry-based model calculations and the high-resolution microanalytical flank method. *Contribution to Mineralogy and Petrology*, 140, 135-147.
- Fialin, M., Wagner, C., Métrich, N., Hulmer, E., Galoisy, L. And Bézoz, A. (2001)  $\text{Fe}^{3+}/\Sigma\text{Fe}$  vs.  $\text{FeL}\alpha$  peak energy for minerals and glasses: Recent advances with the electron microprobe. *American Mineralogist*, 86, 456-465.
- Fei (1995) Thermal expansion. *Mineral Physics and Crystallography: A Handbook of Physical Constants*. AGU.
- Fei, Y. (1999) Effects of temperature and composition on the bulk modulus of  $(\text{Mg,Fe})\text{O}$ , *American Mineralogist*, 84, 272-276.
- Fei, Y. and Mao, H.K. (1994) In situ determination of the NiAs phase of FeO at high pressure and temperature. *Science*, 266: 1668-1680.
- Fei, Y., Mao, H.K., Shu, J., Hu., J. (1992) P–V–T equation of state of magnesiowüstite  $(\text{Mg}_{0.6}\text{Fe}_{0.4})\text{O}$ . *Phys Chem Miner* 18, 416–422.
- Fischer, D.W. (1965) Changes in the soft X-ray L emission spectra with oxidation of the first series transition metals. *Journal of Applied Physics*, 36, 2048-2053.
- Frost, D.J., Poe, B.T., Tronnes, R.G., Liebske, C., Duba, A., Rubie, D.C. (2004a) A new large volume multianvil system. *Phys. Earth Planet. Inter.* 143-144. 507-514.

## 7. References

- Frost, D.J., Liebske, C., Langenhorst, F., McCammon, C.A., Trønnes, R.G. and Rubie, D.C. (2004b) Experimental evidence for the existence of iron-rich metal in the Earth's lower mantle. *Nature*, 428, 409-412.
- Frost, D.J. (2008) The Upper Mantle and Transition Zone. *Elements Magazine*, 4, 171-176.
- Garvie, L.A.J. and Craven, A.J. (1994) Use of electron-energy loss near-edge fine structure in the study of minerals. *American Mineralogist*, 79, 411-425.
- Gavrilenko, P. (2008) Water solubility in Diopside. Ph.D Thesis, University of Bayreuth.
- Giddings, R.A. and Gordon, R. S. (1973) Review of Oxygen Activities and Phase Boundaries in Wüstite as Determined by Electromotive-Force and Gravimetric Methods. *Journal of the American Ceramic Society*, 56, 111-116.
- Goarant, F., Guyot, F., Peyronneau, J. and Poirier, J.P. (1992) High-pressure high-temperature reactions between silicates and liquid iron alloys, in the diamond anvil cell, studied by analytical electron microscopy. *J. Geophys. Res.*, 97, 4477-4487.
- Golla, U. and Putnis, A. (2001) Valence state mapping and quantitative electron spectroscopic imaging of exsolution in titanohematite by energy-filtered TEM. *Physics and Chemistry of Minerals*, 28, 119-129.
- Grant, C.A., (1995) Sources of experimental and analytical error in measurements of the Mössbauer effect in amphibole [Ph.D. thesis]: Eugene, University of Oregon, 255 p.
- Grasserbauer, M (1975a) Die Bedeutung der Valenzbandspektren in der Elektronenstrahl-Mikroanalyse. II. *Mikrochim. Acta* 1: 563-576.
- Grasserbauer, M (1975b) Die Bedeutung der Valenzbandspektren in der Elektronenstrahl-Mikroanalyse. III. *Mikrochim. Acta* 1: 597-610.
- Gütlich, P., Link, R., and Trautwein, A. (1978) Mössbauer spectroscopy and transition metal chemistry. Berlin: Springer-Verlag.
- Hahn, W.C. Jr. and Muan, A. (1962) Activity measurements in oxides solid solutions: the system FeO-MgO in the temperature interval 1100 °C to 1300°C. *Trans. AIME*, 224 [3], 416-420.
- Harris, J.W., Hutchison, M. T., Hursthouse, M., Light, M., Harte, B. (1997) A new tetragonal silicate mineral occurring as inclusions in lower-mantle diamonds. *Nature*, 387, 486-488.
- Harte, B., and Harris, J.W. (1994) Lower mantle mineral associations preserved in diamonds. *Mineralogical Magazine*, 58A, Goldschmidt Conference Edinburgh.

## 7. References

- Harte, B., Harris, J.W., Hutchison, M.T., Watt, G.R. and Wilding, M.C. (1999) Lower mantle mineral associations in diamonds from Sao Luiz, Brazil. In *Mantle Petrology: Field Observations and High Pressure Experimentation: A tribute to Francis R. (Joe) Boyd* (ed. Y. Fei, C.M. Bertka and B.O. Mysen), The Geochemical Society, Houston, 125-153.
- Hayman, P.C., Kopylova, M.G., Kaminsky, F.V. (2005) Lower mantle diamonds from Rio Soriso (Juina area, Mato Grosso, Brazil). *Contribution to Mineralogy and Petrology*, 149, 430-445.
- Hazen, R.M. (1981) Systematic variation of bulk modulus of wüstite with stoichiometry. *Carnegie Inst Wash. Yearb* 80: 277-280.
- Hazen, R.M., and Jeanloz, R. (1984) Wüstite ( $\text{Fe}_{1-x}\text{O}$ ): A review of its defect structure and physical properties, *Rev. Geophys.*, 22, 37-46.
- Heaman, L.M., Teixeira, N.A., Gobbo, L., and Gaspar, J.C. (1998) U-Pb mantle zircon ages for kimberlites from the Juina and Paranatinga provinces, Brazil. 7th International Kimberlite Conference, Cape Town, South Africa, Extended Abstracts, p. 322–324.
- Hergt, J.M., Peate, D.W., and Hawkesworth, C.J. (1991) The petrogenesis of Mesozoic Gondwana low-Ti flood basalts: *Earth and Planetary Science Letters*, v. 105, p. 134–148.
- Höfer, H.E. (2002) Quantification of  $\text{Fe}^{2+}/\text{Fe}^{3+}$  by Electron Microprobe Analysis – New Developments. *Hyperfine Interactions*, 144/145, 239-248.
- Höfer, H.E., Brey, G.P., and Oberhänsli, R. (1995) The determination of the oxidation state of iron in synthetic garnets by X-ray spectroscopy with the electron microprobe. *Physics and Chemistry of Minerals*, 23, 241.
- Höfer, H.E., Brey, G.P., Schulz-Dobrick, B., and Oberhänsli, R. (1994) The determination of the oxidation state of iron by the electron microprobe. *European Journal of Mineralogy*, 6, 407-418.
- Höfer, H.E., and Brey, G.P. (2001) The use of soft X-ray emission to determine the iron oxidation state in synthetic garnet samples by the electron microprobe. 11th Annual V.M. Goldschmidt Conference, p. 3227.
- Höfer, H.E. and Brey, G.P., (2007). The iron oxidation state of garnet by electron microprobe: its determination with the flank method combined with major-elements analysis. *American Mineralogist*, 92, 873-885.

## 7. References

- Höfer, H.E., Weinbruch, S., McCammon, C.A., and Brey, G.P. (2000) Comparison of two electron probe microanalysis techniques to determine ferric iron in synthetic wüstite samples. *European Journal of Mineralogy*, 12, 63-71.
- Hutchison, M.T. (1997) Constitution of the deep transition zone and lower mantle shown by diamonds and their inclusions. Ph.D Thesis, University of Edinburgh.
- Jacobsen, S.D., Angel, R.J., Reichmann, H.-J., Mackwell, S.J., McCammon, C.A., Smyth, J.R., and Spetzler, H.A. (1999) Hydrostatic compression of single-crystal magnesiowüstite. *EOS Transactions* 80:937
- Jacobsen, S.D., Reichmann, H.-J., Spetzler, H.A., Mackwell, S.J., Smyth, J.R., Angel, R. and McCammon, C.A. (2002) Structure and elasticity of single-crystal (Mg,Fe)O and a new method of generating shear waves for gigahertz ultrasonic interferometry. *Journal of Geophysical Research Letters*, 107, B2, 4, 1-14.
- Jackson, L., and Niesler, H. (1982) The elasticity of periclase to 3 GPa and some geophysical implications. In S. Akimoto and M.H. Manghnani, Eds., *High-pressure research in geophysics*, p. 93-133. Center for Academic Publications, Tokyo.
- Jeanloz, R. (1990) The nature of the Earth's core. *Ann. Rev. Earth Planet. Sci.*, 18, 357-386.
- Jeanloz, R., and Ahrens, T.J. (1980) Equation of state of FeO and CaO. *Geophys.J.R.Astron.Soc.*, 62: 505-528.
- Jephcoat, A. and Olson, P. (1987) Is the inner core of the Earth pure iron? *Nature*, 325, 332-335
- Kantor, I.Y., Dubrovinsky, L.S. and McCammon, C.A. (2006) Spin crossover in (Mg,Fe)O: a Mössbauer effect study with an alternative interpretation of x-ray emission spectroscopy data. *Physical Review B*, 73, 10010-1,4.
- Kantor, I.Y., Dubrovinsky, L.S. and McCammon, C.A. (2007) Reply to "Comments on "Spin crossover in (Mg,Fe)O: a Mössbauer effect study with an alternative interpretation of x-ray emission spectroscopy data"". *Physical Review B*, 75, 1771031-1771033.
- Karki, B.B., Wentzcovitch, R.M., de Gironcoli, S., Baroni, S.(1999) First-Principles Determination of Elastic Anisotropy and Wave Velocities of MgO at Lower Mantle Conditions. *Science*, 286, 1705-1707.
- Karki, B.B., Stixrude, L., Clark, S.J., Warren, M.C., Ackland, G.J., and Crain, J. (1997) Structure and elasticity of MgO at high pressure, *American Mineralogist*, 82, 51-60.

## 7. References

- Kawai N., Endo S. (1970) The generation of ultrahigh hydrostatic pressures by split sphere apparatus. *Rev. Sci. Instrum.* 41. 1178-1181.
- Kennet, B.L.N., Engdahl, E.R., and Buland, A. (1995) Constraints on seismic velocities in the Earth from travel times. *Geophys. J. Int.* 122: 108-124.
- Kesson, S.E. and Fitz Gerald, J.D. (1991) Partitioning of MgO, FeO, NiO, MnO and Cr<sub>2</sub>O<sub>3</sub> between magnesian silicate perovskite and magnesiowüstite: implications for the origin of inclusions in diamond and composition of the lower mantle. *Earth and Planetary Science Letters*, 111, 229-240.
- Kesson, S. E., Fitz Gerald, J. D., O'Neill, H. St. C. & Shelley, J. M. G. (2002) Partitioning of iron between magnesian silicate perovskite and magnesiowüstite at about 1 Mbar. *Phys. Earth Planet. Int.* 121, 85–102.
- Knittle, E. and Jeanloz, R. (1989) Simulating the core-mantle boundary: An experimental study of high-pressure reactions between silicate and liquid iron. *Geophys. Res. Lett.*, 16, 609-612.
- Knittle, E., Jeanloz, R., and Smith, G.L. (1986) Thermal expansion of silicate perovskite and stratification of the Earth's mantle. *Nature*, 319, 214-216.
- Knittle, E. and Jeanloz, R. (1986) High pressure metallization of FeO and implications for the Earth's core. *Geophys. Res. Lett* 13: 1541-1544.
- Ito, E., and Takahashi, E., (1989) Postspinel transformations in the system Mg<sub>2</sub>SiO<sub>4</sub>-Fe<sub>2</sub>SiO<sub>4</sub> and some geophysical implications. *Journal of Geophysical Research*, 94, 10637–10646.
- Larson A.C, Von Dreele R.B. (1994) GSAS General Structure Analysis System. Los Alamos National Laboratory, New Mexico, USA.
- Lauterbach, S., McCammon, C.A., van Aken, P., Langenhorst, F. And Seifert, F. (2000) Mössbauer and ELNES spectroscopy of (Mg,Fe)(Si,Al)O<sub>3</sub> perovskite: A highly oxidised component of lower mantle. *Contribution to Mineralogy and Petrology*, 138, 17-26.
- Lay, T. (1995) Seismology of the lower mantle and core-mantle boundary. *Rev. Geophys. Supplement*, (July), 325-328.
- Lay, T. (1989) Structure of the core-mantle transition zone: A chemical and thermal boundary layer. *EOS Trans. AGU*, 70, 49-59.
- Legkova, G.W., Voitkevich, W.G., Sharkin, O.P. (1982) The electron probe determination of the amounts of Fe<sup>2+</sup> and Fe<sup>3+</sup> in amphiboles (in Russian). *Mineral Zhurnal*, 4, 90-93.

## 7. References

- Lin, J.F., Struzhkin, V.V., Jacobsen, S.D., Hu, M.Y., Chow, P., Kung, J., Liu, H., Mao, H.-K., and Hemley, R.J. (2005) *Nature (London)* 436, 377.
- Lin, J.F., Heinz, D.L., Mao, H.-K., Hemley, R.J., Devine, J.L., Li, J., Shen, G. (2003) Stability of magnesiowüstite in Earth's lower mantle. *Proceedings of National Academy of Sciences of the United States of America*, 100, 4405-4408.
- Liu, L. (1999) Genesis of Diamonds in Lower Mantle. *Contrib. Mineral. Petr.*, 134, 170-173.
- Long, G.J. (1983) The Ideal Mössbauer Effect Absorber Thickness. *Mössbauer Effect Reference and Data Journal*, 6(2), 42-29.
- Loper, D.E. (1984) The dynamical structure of D'' and deep plumes in a non-Newtonian mantle. *Phys. Earth Planet. Interiors*, 34, 57-67.
- Loper, D.E. (1978) The gravitationally powered dynamo. *Geophys. J. R. astr. Soc.*, 54, 389-404.
- Mainprice, D. (2007) Seismic anisotropy of the deep Earth from a mineral and rock physics perspective. In: G. Schubert, Editor, *Treatise in Geophysics*, vol. 2, Elsevier, Oxford, pp. 437-492.
- Mao, W.L., Mao, H.-K., Sturhahn, W., Zhao, J., Prakapenka, V.B., Meng, Y., Shu, J., Fei, Y. and Hemley, R.J. (2006) Iron-rich postperovskite and the origin of ultralow-velocity zones. *Science*, 312, 564-565.
- Mao, H.-K., Shen, G., and Hemley, R.J. (1997) Multivariable dependence of Fe-Mg partitioning in the lower mantle, *Science*, 278, 2098-2100.
- Mao, W., Shu, J., Hu, J., Hemley, R. J. & Mao, H. K. (2002) Displacive transition in magnesiowüstite. *J. Phys. Condens. Matter* 14, 1-6.
- Meyer, H.O.A. (1987) Inclusions in diamond. In Nixon PH (ed) *Mantle xenoliths*, John Wiley & Sons, Chichester, pp 501-522.
- Meyer, H.O.A., McCallum, M.E. (1986) Mineral inclusions in diamonds from the Sloan kimberlites, Colorado. *J Geol*, 94, 600-612.
- McCammon C. (2006) Microscopic properties to macroscopic behavior: The influence of iron electronic state. *Journal of Mineralogical and Petrological Sciences*, 101, 130-144.
- McCammon, C.A. (2004) Mössbauer Spectroscopy: Applications. In A. Beran and E. Libowitzky Eds. *Spectroscopic Methods in Mineralogy*. *Emu notes in Mineralogy*, 6, 369-398.
- McCammon, C. (2001) Deep Diamond Mysteries. *Science*, 293, 813-814.

## 7. References

- McCammon, C.A. (2000) Insights into Phase Transformations from Mössbauer Spectroscopy. In P. H. Ribbe Eds. Transformation Processes in Minerals. Reviews in Mineralogy and Geochemistry, 39, 241-264.
- McCammon, C.A. (1997) Perovskite as a possible sink for ferric iron in the lower mantle. *Nature*, 387, 694-696.
- McCammon, C.A. (1994) A Mössbauer milliprobe: Practical considerations. *Hyperfine Interactions*, 92, 1235-1239.
- McCammon, C.A., Hutchison, M., and Harris, J. (1997) Ferric iron content of mineral inclusions in diamonds from São Luiz: a view into the lower mantle. *Science*, 278, 434-436.
- McCammon, C.A., Lauterbach, S., Seifert, F., Langenhorst, F., van Aken, P.A. (2004a) Iron oxidation state in lower mantle assemblages I. Empirical relations derived from high-pressure experiments. *Earth and Planetary Science Letters*, 222, 435-449.
- McCammon, C.A., Peyronneau, J., Poirier, J.-P. (1998) Low ferric iron content in (Mg,Fe)O at high pressures and high temperatures. *Geophysical Research Letters*, 25, 1589-1592.
- McCammon, C.A., Stachel, T., Harris, J.W. (2004b). Iron oxidation state in lower mantle mineral assemblages II. Inclusions in diamonds from Kankan, Guinea. *Earth and Planetary Science Letters*, 222, 423-434.
- McGuire, A.V., Francis, C.A., and Dyar, M.D. (1992) Mineral standards for microprobe analysis of oxygen. *American Mineralogist*, 77, 1087-1091.
- Murakami, M., Hirose, K., Kawamura, K., Sata, N., Ohishi, Y. (2004) Post-Perovskite phase transition in MgSiO<sub>3</sub>. *Science*, 304, 855-858.
- Odake, S., Fukura, S., Arakawa, M., Ohta, A., Harte B. and Kagi, H. (2008) Divalent chromium in ferropervicite inclusions in lower mantle diamonds revealed by micro-XANES measurements. *Journal of Mineralogical and Petrological Sciences*, 103, 350-353.
- Olson, O., Schubert, G. and Anderson, C. (1987) Plume formation in the D'' layer and the roughness of the core-mantle boundary. *Nature*, 327, 409-413.
- O'Neill, H.S.C. (1986) Mo-MoO<sub>2</sub> (MOM) oxygen buffer and the free energy of formation of MoO<sub>2</sub>. *American Mineralogist*, 71, 1007-1010.
- O'Nions, R.K. and Smith, D.G.W. (1971) Investigations of the LII,III X-ray emission spectra of Fe by electron microprobe. Part 2. The FeLII,III spectra of Fe and Fe-Ti oxides. *American Mineralogist*, 56, 1452-1463.

## 7. References

- Pankhurst, R.J., Leat, P.T., Sruoga, P., Rapela, C.W., Marquez, M., Storey, B.C., and Riley, T.R. (1998) The Chon Aike province of Patagonia and related rocks in West Antarctica: A silicic large igneous province. *Journal of Volcanology and Geothermal Research*, v. 81, p. 113–136.
- Pavicević, M.K., Amthauer, G., El Goresy, A. (1989) X-ray L-emission spectra of iron on silicate garnets. *J. Serb. Chem. Soc.*, 54, 359-371.
- Pavicević, M.K., Ramdohr, P., El Goresy, A. (1972) Electron microprobe investigations of the oxidation states of Fe and Ti in Ilmenite in Apollo 11, Apollo 12, and Apollo 14 crystalline rocks. *Geochimica and Cosmochimica Acta Supplem.* 3(1), 295-303.
- Pavicević, M.K., Timotijevi, D., Amthauer, G. (1992) Electron configuration of the valence and the conduction band of magnetite ( $\text{Fe}_3\text{O}_4$ ) and hematite ( $\alpha\text{-Fe}_2\text{O}_3$ ). In: *Inst. Phys. Conf. Ser. No. (Int. Congr. X-ray optics and microanalysis, Manchester)*, 130, 101-104.
- Prewitt, C.T., and Downs, R.T. (1998) High pressure crystal chemistry, in *Ultra-high-Pressure Mineralogy: Physics and Chemistry of the Earth's Deep Interior (1998)* edited by R.J. Hemley, *Rev. Mineral.*, 37, 283-317, Mineral Society of America, Washington D.C.
- Raeburn, S.P., Ilton, E.S., and Veblen, D.R. (1997a) Quantitative determination of the oxidation state of iron in biotite using X-ray photoelectron spectroscopy: Calibration. *Geochimica and Cosmochimica Acta*, 61, 4519-4530.
- Raeburn, S.P., Ilton, E.S., and Veblen, D.R. (1997b) Quantitative determination of the oxidation state of iron in biotite using X-ray photoelectron spectroscopy: II. In situ analysis. *Geochimica and Cosmochimica Acta*, 61, 4531-4537.
- Rama Murthy, V. and Hall, H.T. (1970) The chemical composition of the Earth's core: Possibility of sulfur in the core. *Phys. Earth Planet. Interiors*, 2, 276-282.
- Ramsey, W.H. (1949) On the nature of the Earth's core. *Mon. not. R. astr. Soc. Geophys. Suppl.*, 5, 409-426.
- Rancourt, D.G., McDonald, A.M., Lalonde, A.E., and Ping, J.Y. (1993) Mössbauer absorber thicknesses for accurate site populations in Fe-bearing minerals. *American Mineralogist*, 78, 1-7.
- Reed, S.J.B. (2005) *Electron Microprobe Analysis and Scanning Electron Microscopy in Geology*. Cambridge University Press.

## 7. References

- Reichmann, H.-J., Angel, R.J., Spetzler, H., and Bassett, W.A. (1998) Ultrasonic interferometry and X-ray measurements on MgO in a new diamond anvil cell. *American Mineralogist*, 83, 1357-1360.
- Reichmann H-J, Jacobsen SD, Mackwell SJ, McCammon CA (2000) Sound wave velocities and elastic constants for magnesiowüstite using gigahertz interferometry. *Geophys Res Lett* 27: in press
- Richet P, Mao HK, Bell PM (1989) Bulk moduli of magnesiowüstites from static compression measurements. *J. Geophys. Res.*, 94, 3037–3045.
- Rickard, R.S., Harris, J.W., Gurney, J.J., and Cardoso, P. (1989) Mineral inclusions in diamonds from Koffiefontein mine, in Ross, J., ed., *Kimberlites and related rocks*. Volume 2: Geological Society of Australia Special Publication 14, p. 1054–1062.
- Ringwood, A.E. (1991) Phase transformations and their bearing on the constitution on the mantle. *Geochimica and Cosmochimica Acta*, 55, 2083-2110.
- Rubie, D.C. (1999) Characterizing the sample environment in multianvil High-Pressure experiments. *Phase Transitions*, 68, 431-451.
- Schaefer, W.L., and Brindley, G.W. (1963) Oxidation of magnesiowüstite single crystals, I, Optical and kinetic data, *J. Phys. Chem. Solids*, 24, 919-925.
- Schulze, D.J., Harte, B., Valley, J.W., Dominic, M. and Channer, DeR. (2004) Evidence of subduction and crust-mantle mixing from a single diamond. *Lithos*, 77, 349-358.
- Scott-Smith, B.H., Danchin, R.V., Harris, J.W., Stracke, K.J. (1984) Kimberlites near Orroroo, South Australia. In Kornprobst J (ed) *Kimberlites I: kimberlites and related rocks*, Elsevier, Amsterdam, pp 121-142.
- Shim, S.-H., Duffy, T.S. and Shen, G. (2001) The post-spinel transformation in Mg<sub>2</sub>SiO<sub>4</sub> and its relation to the 660-km seismic discontinuity, *Nature*, 411, 571-574.
- Shu, J., Mao, H. K., Hu, J., Fei, Y. & Hemley, R. J. (1998a) *N. Jb. Mineral. Abh.* 172, 309–323.
- Shu, J., Mao, H. K., Hu, J., Fei, Y. & Hemley, R. J. (1998b) *Eos Trans. Am. Geophys. Union* 79 (17), Spring Meeting Suppl., abstr. M21A-01.
- Sinogeikin, S.V., and Bass, J.D. (2000) Single-crystal elasticity of pyrope and MgO to 20 GPa by Brillouin scattering in the diamond cell, *Phys. Earth Planet. Inter.*, 120, 43-62.
- Smith, C.B. (1983) Pb, Sr and Nd isotopic evidence for sources of southern African Cretaceous kimberlites: *Nature*, v. 304, p. 51–54, doi: 10.1038/304051a0.

## 7. References

- Sobolev NV, Efimova ES, Pospelova LN (1981) Native iron in Yakutian diamonds and its paragenesis (in Russian). *Geol Geophys Akad Nauk SSSR Sib* 12: 25±29.
- Sobolev, V.N., McCammon, C.A., Taylor, L.A., Snyder, G.A., and Sobolev, N.V. (1999) Precise Mössbauer milliprobe determination of ferric iron in rock-forming minerals and limitations of electron microprobe analysis. *American Mineralogist*, 84, 78-85.
- Song, X. and Ahrens, T.J. (1994) Pressure-temperature range of reactions between the liquid iron in the outer core and the mantle silicates. *Geophys.Res.Lett.*, 21, 153-156.
- Speidel, D.H. (1967) Phase equilibria in the system MgO– FeO–Fe<sub>2</sub>O<sub>3</sub>: the 1300 °C isothermal section and extrapolations to other temperatures, *J. Am. Ceram. Soc.* 50, 243–248.
- Spetzler, H. (1970) Equation of state of polycrystalline and single crystal MgO to 8 kilobars and 800 K. *Journal of Geophysical Research*, 75, 2073-2087.
- Speziale, S., Milner, A.A., Lee, V.E., Clark, S.M., Pasternak, M.P. and Jeanloz, R. (2005). Iron spin transition in Earth's mantle. *Proceedings of the National Academy of Sciences*, 102(50): 17918-17922.
- Speziale, S. Lee, V., Clark, S.M., Lin, J-F., Pasternak, M.P. and Jeanloz, R. (2007) Effects of Fe spin transition on the elasticity of (Mg,Fe)O magnesiowüstite and implications for the seismological properties of the Earth's lower mantle. *Journal of Geophysical Research*, 112.
- Srečec, I., Ender, A., Woermann, E., Gans, W., Jacobsson, E., Eriksson, G. and Rosén E. (1987) Activity-Composition Relations of the Magnesiowüstite Solid Solution Series in Equilibrium with Metallic Iron in the Temperature Range 1050-1400 K. *Phys. Chem. Minerals*, 14, 492-498.
- Stacey, F.D. and Davis, P. (2008) *Physics of the Earth*, Cambridge University Press.
- Stachel, T., Brey, B.P., Harris, J.W. (2005) Inclusions in Sublithospheric Diamonds: Glimpses of Deep Earth. *Elements Magazine*, 1, 73-78.
- Stachel, T. (2001) Diamonds from the asthenosphere and the transition zone, *Eur. J. Mineral.*, 13, 883– 892.
- Stachel, T., Brey, G.P., Harris J.W. (2000) Kankan diamonds (Guinea) I: from the lithosphere down to the transition zone. *Contribution to Mineralogy and Petrology*, 140, 1-15.
- Stachel, T., Harris, J.W. and Brey, G.P. (1997) Rare and unusual inclusions in diamonds from Mwadui, Tanzania. *Contrib. Mineral. Petrol.*, 132, 34-47.

## 7. References

- Stagno, V. and Frost, D. (2008) Carbonatites, kimberlites and diamonds in the Earth's mantle. In preparation.
- Stiefenhofer, J., and Farrow, D.J. (2004) Geology of the Mwadui kimberlite, Shinyanga district, Tanzania: *Lithos*, v. 76, p. 139–160, doi: 10.1016/j.lithos.2004.04.017.
- Suzuki, T., Akimoto, S. and Fukai, Y. (1984) The system iron-enstatite-water at high pressures and temperatures – formation of iron hydride and some geophysical implications. *Phys. Earth Planet. Interiors*, 36, 135-144.
- Suzuki, I. (1975) Thermal expansion of periclase and olivine, and their anharmonic properties. *J. Phys. Earth*, 23, 145-159.
- Tange, Y., Takahashi, E., Nishihara, Y., Funakoshi, K. and Sata, N. (2009) Phase relations in the system MgO-FeO-SiO<sub>2</sub> to 50 GPa and 2000°C. An application of experimental techniques using multianvil apparatus with sintered diamond anvils. *Journal of Geophysical Research*, 114, B02214, 1-12.
- Tappert, R., Stachel, T., Harris, J.W., Muehlenbachs, K., Ludwig, T., and Brey, G.P. (2005) Subducting oceanic crust: The source of deep diamonds. *Geology*, v. 33, p. 565–568.
- Tappert, R., Foden, J., Stachel, T., Muehlenbachs, K., Tappert, M., Wills, K. (2009) Deep mantle diamonds from South Australia: A record of Pacific subduction at the Gondwanan margin. *Geology*, v. 37, no. 1; p. 43-46.
- Tappert, R., Foden, J., Muehlenbachs, K., Stachel, T., Goryniuk, M., Wills, K. (2008) The diamonds of South Australia. 9<sup>th</sup> International Kimberlite Conference Extended Abstract No.9IKC-A-00209
- Tassinari, C.C.G. and Macambira, M.J.B. (1999) Geochronological provinces of the Amazonian craton. *Episodes* 22, 174-182.
- Thomassot, E., Cartigny, P., Harris, J.W., Lorand, J.P., Rollion-Bard, C., Chaussidon, M. (2009) Metasomatic diamond growth: A multi-isotope study (<sup>13</sup>C, <sup>15</sup>N, <sup>33</sup>S, <sup>34</sup>S) of sulphide inclusions and their host diamonds from Jwaneng (Botswana). *Earth and Planetary Science Letter*, 282, 79-90.
- Thomassot, E., Cartigny, P., Harris, J.W., K.S. (Fanus) Viljoen (2007) Methane related diamond crystallization in the Earth's Mantle: Stable isotope evidences from a single diamond bearing xenolith. *Earth and Planetary Science Letters*, 257, 362-371.
- Tobi, B.H. (2001) EXPGUI, a graphical user interface for GSAS. *J. Appl. Cryst.*, 34, 210-213.

## 7. References

- Tromp, J. (2001) Inner-core anisotropy and rotation. *Ann. Rev. Earth Planet. Sci.*, 29, 47-69.
- Ulmer, G.C. and Barnes, H.L. (1987) *Hydrothermal Experimental Techniques*. A Wiley-Interscience publication. ISBN 0-471-82145-4.
- Urakawa, S., Kato, M. and Kumazawa, M. (1987) Experimental study on the phase relations in the system Fe-Ni-O-S up to 15 GPa. In *High Pressure Research in Mineral Physics*, M.H. Manghnani and Y. Syono eds., American Geophysical Union, Washington, D.C., 95-111.
- van Aken, P.A. and Liebscher, B. (2002) Quantification of ferrous/ferric ratios in minerals: new evaluation schemes of the L<sub>23</sub> electron energy-loss near edge spectra. *Physics and Chemistry of Minerals*, 29, 188-200.
- van Aken, P.A., Liebscher, B., and Styrsa, V.J. (1998) Quantitative determination of iron oxidation state in minerals using FeL<sub>23</sub>-edge electron energy-loss near-edge structure spectroscopy. *Physics and Chemistry of Minerals*, 25, 323-327.
- van Aken, P.A., Styrsa, V.J., Liebscher, B., Woodland, A.B., and Redhammer, G.J. (1999) Microanalysis of Fe<sup>3+</sup>/ΣFe in oxide and silicate minerals by investigation of electron energy-loss near-edge structures (ELNES) at the Fe M<sub>2,3</sub> edge. *Physics and Chemistry of Minerals*, 26, 584-590.
- Vissiliou, M.S. and Ahrens, T.J. (1982) The equation of state of Mg<sub>0.6</sub>Fe<sub>0.4</sub>O to 200 GPa. *Geophys. Res. Lett.* 9, 127-130.
- Vissiliou, M.S. and Ahrens, T.J. (1981) Hugoniot equation of state of periclase to 200 GPa. *Geophys. Res. Lett.*, 8, 729-732.
- Wagner, C., Deloule, E., Fialin, M. and King, P.L. (2008) Dehydrogenation of kaersutitic amphibole under electron beam excitation recorded by changes in Fe<sup>3+</sup>/ΣFe: An EMP and SIMS study
- Walter, M.J., Bulanova, G.P., Armstrong, L.S., Keshav, S., Blundy, J.D., Gudfinnsson, G., Lord, O.T., Lennie, A.R., Clark, S.M., Smith, C.B. and Gobbo, L. (2008) Primary carbonatite melt from deeply subducted oceanic crust. *Nature*, 454, 622-626.
- Williams, Q., Jeanloz, R. and McMillan, P. (1987) Vibrational spectrum of MgSiO<sub>3</sub> perovskite: Zero-pressure Raman and mid-infrared spectra to 27 GPa. *J. Geophys. Res.*, 92, 8116-8128.
- Wood, B.J. (1993) Carbon in the core. *Earth and Planetary Science Letter*, 117, 593-607.
- Yagi, T., Suzuki, K., Akimoto, S. (1985) Static compression of wüstite (Fe<sub>0.98</sub>O) to 120 GPa. *J. Geophys Res* 90: 8784-8788.

## 7. References

- Zha C.S., Mao H.K., Hemley R.J. (2000) Elasticity of MgO and a primary pressure scale to 55 GPa. *Proceedings of National Academy of Sciences USA* 97, 13494-13499.
- Zhang, J. (2000) Effect of Defects on the Elastic Properties of Wüstite. *Physical Review Letters* 84, 507-510.
- Zharkov, V.N., Karpov, P.B. and Leontjeff, V.V. (1985) On the thermal regime of the boundary layer at the bottom of the mantle. *Phys. Earth Planet. Interiors*, 41, 138-142.
- Zou, G., Mao, H.K., Bell, P.M., Virgo, D. (1980) High-pressure experiments on the iron oxide wüstite ( $\text{Fe}_{1-x}\text{O}$ ) *Carnegie Inst Washington Year book* 79: 374-376.

## **Erklärung**

Hiermit erkläre ich, dass ich die vorliegende Arbeit selbständig verfasst und keine andere als die von mir angegebenen Quellen und Hilfsmittel benutzt habe.

Ferner erkläre ich, dass ich nicht anderweitig versucht habe, mit oder ohne Erfolg, eine Dissertation einzureichen und auch keine gleichartige Doktorprüfung an einer anderen Hochschule endgültig nicht bestanden habe.

Bayreuth, im Juli 2009

Micaela Longo